Synthesis, Microstructure and Mechanical Properties of Titanium with Controlled Levels of Porosity

A thesis

submitted in fulfilment

of the requirements for the degree

of

Doctor of Philosophy in Materials and Process Engineering

at

The University of Waikato

by

Qian Xu

THE UNIVERSITY OF
WAIKATO
Te Whare Wānanga o Waikato

2014

Abstract

Porous titanium (Ti) products have many applications due to their excellent corrosion resistance, high strength-to-weight ratio, high specific surface area, etc. However, the major limitation is the expensive cost of porous Ti products because of the high raw materials costs and the difficulty of processing. The novelty of this research work is concerned with a study of a ceramic casting technique, slip casting, to create porous Ti products and the effect of porosity on the mechanical properties and gas permeability of Ti compacts.

An optimised Ti slurry was developed from 43 vol.% of Ti powder, 0.3 dw.% of dispersant, 0.8 dw.% of plasticiser and 0.8 dw.% of binder, mixed with a balance of distilled water, which produced a viscosity of 290 cP. It was then poured into a plaster mould to form compacts with a green density of 45%. Thermal debinding was carried out at 320°C with an argon flow for 2 hours, followed by vacuum sintering different samples at 1000°C and 1200°C for 0.5 hours, respectively. The porous sintered compacts had satisfactory tensile strength with some plastic deformation. The increase in oxygen and carbon content during processing was minor. The results from this investigation suggested that slip casting is a potentially low-cost, simple manufacturing route for porous Ti products.

Porous Ti compacts with porosity in the range of 12.3 vol.% to 35.3 vol.% were fabricated by slip casting. The mechanical properties, fracture morphology, gas permeability, pore size analysis and pore shape factors for the porous Ti compacts were determined for different porosity levels. A decreasing porosity level resulted in less open porosity and gas permeability, reduced pore size, and an increased tensile stress and elongation. The mechanical properties of porous Ti compacts produced by slip casting were comparable with more conventional press and sintered materials at the same porosity levels. Theoretical models for tensile stress and ductility as a function of porosity were examined and incorporated into the results and differences between the theoretical models and experimental results are discussed. The pore shape factor analysis showed that tensile loading would stretch the pores in the compacts to produce more irregular pores, which were acting as linkage sites to allow the propagation of cracks. Additionally, a novel interconnected pore characterisation method using ammonium meta-tungstate solution is presented. By using backscatter scanning electron microscopy, the interconnected pores can be directly observed.

The packing behaviour and sintering behaviour of Ti compacts fabricated with different particles size distribution were characterised and studied, in terms of porosity, pore size analysis, tensile properties and gas permeability. Two different particles size (avg. 14 µm & avg. 56 µm) of pure Ti hydride-dehydride powder were used in five volume proportions (20:80, 40:60, 60:40, 80:20 & 100:0). A theoretical model predicted that the green density reaches a maximum when the volume fraction of fine particles is 0.35. It was found that although experimental results showed similar behaviour there was no well-defined maximum green density. The sintered compacts showed that an increase in the volume fraction of fine powder particles reduced the porosity, permeability level and pore size, and increased the tensile properties. The relationship between permeability and porosity level was non-linear and this was caused by the differences in pore diameters in the compacts. The capillary tube model was used to discuss the relationship between the permeability, pore diameter and porosity. Using this information, a graded porosity compact was designed and fabricated by slip casting. A future study on this graded porosity compacts is recommended to undertake in more depth.

Publications

Journal Publications

1. Xu, Q., Gabbitas, B., Matthews, S., (2014). "*Titanium compacts with controllable porosity by slip casting of binary powder mixtures.*" Powder Technology 266: 396-406.
2. Xu, Q., Gabbitas, B., Matthews, S., (2014). "*The effect of binder and plasticizer on porous titanium compacts prepared by slip casting.*" Procedia Materials Science 4: 78-81.
3. Xu, Q., Gabbitas, B., Matthews, S., (2013). "*Influence of porosity on mechanical behaviour and gas permeability of Ti compacts prepared by slip casting*." Materials Science and Engineering: A 587: 123-131.
4. Xu, Q., Gabbitas, B., Matthews, S., Zhang, D., (2013). "*The development of porous Ti products using slip casting.*" Journal of Materials Processing Technology 213(8): 1440-1446.
5. Xu, Q., Gabbitas, B., Matthews, S., Zhang, D., (2012). "*Optimisation of performance of dispersants in aqueous Ti slips*." Key Engineering Materials 520: 330-334.

Conference Proceedings

1. Xu, Q., Gabbitas, B., Matthews, S., Zhang, D. "*.Influence of particles size fraction on slip casting of Ti.*" Proceedings of Ti-WaiCAM symposium, Hamilton, New Zealand, February, 2013.
2. Xu, Q., Gabbitas, B., Matthews, S., Zhang, D. "*An alternative to make porous Ti products – Slip casting & Tape Casting.*" Proceedings of Ti-WaiCAM symposium, Hamilton, New Zealand, February, 2011.

Acknowledgements

First of all, I would like to express my special thanks of gratitude to my chief supervisor, Professor Brian Gabbitas for giving me the golden opportunity to do this wonderful project on the topic "Synthesis, Microstructure and Mechanical Properties of Ti with Controlled Levels of Porosity". I am thankful for his guidance, advice, support (both financial and educational) and understanding. I would also like to thank my previous research co-supervisor, Professor Deliang Zhang, and current research co-supervisor, Dr. Rob Torrens for the helpful advice.

Special thanks to Dr. Steven Matthews, from the Massey University for his valuable discussion and suggestions on my experimental work and published journal papers. My sincere thanks to Dr. Chris Yu Chen, from Pyrotek Ltd., for his treasured discussion and suggestions on the slip casting work. Many thanks to Dr. Jian Yu, from GaoQ Functional Materials Ltd, China, for providing permeability and pore size analysis test. Great thanks to Associate Professor Alan Langdon for his timely help and suggestions on the application of porous Ti as an electrode in water purification process. Also special thanks to Professor Janis Swan who guided me into the engineering study seven years ago.

I would like to express my appreciation to all research officers, Stiliana Raynova, Dr. Mingtu Jia and Dr. Fei Yang, all technical staff, Helen Turner, Dr. Lisa Li, Indar Singh, Chris Wang, Yuanji Zhang, Brett Nichol, Alan Smith, Martin Gore and Michael Hoogeveen, administrative staff, Mary Dalbeth and Janine Williams, all PhD students in Ti research group, Izhar Abdul Aziz, Ajit Pal Singh, Dengshan Zhou, Jia Lou, Huiyang Lu, Kenneth Sichone, Paul Ewart, Navaneeth Velluva, Thavanayagam Gnanavithan and Dr. Amro Gazawi.

I would like to thank the Ministry of Business, Innovation and Employment (MBIE) for funding this project.

Last, but certainly not least, I am truly grateful to my parents, my uncle, Dr. Ganqing Xu, my auntie-in-law, Mrs Suqiong Liu, Lingze Deng, Luyuan Chen and my Little Rabbit for their love, motivation and constant support in my life.

Contents

List of Figures

List of Tables

1. Chapter 1 -- Introduction

1.1 Background

Titanium (Ti) ranks as the ninth most plentiful element and the fourth most abundant structural metal in the Earth’s crust [1]. However, Ti is never found in a pure state. In 1910, Matthew Albert Hunter from Rensselaer Polytechnic Institute in Troy, N.Y., was first to isolate Ti metal by heating titanium tetrachloride ($TiCl_4$) with sodium in a steel bomb. In 1932, Wilhelm Justin Kroll from Luxembourg produced significant quantities of Ti by combining $TiCl_4$ with calcium and later on he demonstrated that Ti could be extracted commercially by reducing $TiCl_4$ by using magnesium [1]. To date, Ti is still produced in a batch process rather than a continuous process. As a result, the difficulty in processing makes Ti and Ti products expensive.

Porous Ti has a wide range of applications, including biomedical implants, sandwich cores in structural applications, chemical filters and acoustic absorbers, owing to its good strength-to-weight ratio, excellent corrosion resistance and high surface area. However, because pure Ti has a strong chemical affinity to oxygen and too high interstitial oxygen content results in embrittlement, so far, the fabrication process for porous Ti products has mainly focused on a powder metallurgy route. This has led to the development of novel powder metallurgy techniques for low cost manufacturing to give different kinds of pore microstructures and properties of porous Ti. These include freeze casting [2-6], creep expansion [7], space-holder technique [8-12], gel casting [13-15], etc.

1.2 Research aims

The first aim of this project is to develop a novel low cost processing route for making porous Ti. A slip casting process was selected because of its novelty and simplicity in ceramics processing. Ohkawa et al. studied Ti slip casting for dental applications using sodium alginate as a binder [16]. Due to the contamination from the decomposition of sodium alginate, a TiC phase was found in the sintered Ti compact. Thus, a brittle sintered Ti part was produced. In another Ti slip casting study, a slurry formed from a mixture of Ti and TiH_2 powder was used to make a Ti foam with a porosity ranging from 56.1 vol.% to 65.2 vol.% [17]. In this case, safety is a major concern due to the high reactivity of TiH_2. Thus, this novel process comprises its own special formulation, which is different from the two processes mentioned above and also resolves the contamination issue.

The second aim of this project is to control the porosity level in the slip cast Ti compact by using different sintering conditions (sintering temperature, sintering time, heating rate and cooling rate) and powder compositions with different powder particle sizes. It is also important to understand the influence of porosity on mechanical properties, gas permeability and pore size distribution of the slip cast Ti. Oh et al. [18] investigated the compressive strength and open porosity level of porous Ti with porosity ranging from 5.0 to 37.1 vol.%, produced by a press and sintering route. It would be of interest to compare the properties of slip cast Ti compacts with that made by other powder metallurgy routes.

1.3 Thesis outline

This thesis is organised into seven chapters as outlined below.

Chapter 1	The introduction gives the motivation for carrying out this research, the research aims and objectives and an outline of the thesis. The introduction includes the developmental history of Ti, the applications of porous Ti and a brief summary of novel powder metallurgical routes for making porous Ti.
Chapter 2	The literature review provides an overview of the research into the processing techniques for making porous Ti, novel powder casting techniques, the roles of slurry formulation in slip casting and the relationships between porosity, tensile properties and permeability.
Chapter 3	The methods chapter describes the experimental process of slip casting, experimental design using a binary powder particle size system and materials analysis including porosity measurements, permeability analysis, pore size analysis, interconnected pore characterization, tensile testing, fractography, oxygen and carbon analysis and pore shape analysis.

Chapter 4	This chapter focuses on the study of slurry formulation (dispersant, binder, plasticiser and solids content level) in a slip casting. A complete study is presented, from an investigation of the basic slurry formulation to the final sintered compact. The tensile properties, oxygen and carbon levels in sintered Ti compacts depend on the effectiveness of the optimised slurry formulation. Results confirming this are presented.
Chapter 5	By following the optimised slurry formulation, a series of sintering experiments using different conditions, namely sintering temperature, sintering time, heating rate and cooling rate, were carried out to control the porosity in the sintered Ti compacts based on Taguchi experimental design. The influence of porosity on the tensile properties, permeability and pore size of slip cast Ti compacts are shown. The tensile fracture models for porous Ti compacts are also illustrated.
Chapter 6	This chapter describes the effect of different binary powder compositions on the porosity, pore size distribution, permeability and tensile properties of slip cast Ti. A Ti compact with a porosity gradient was also designed by the slip casting technique.
Chapter 7	The conclusions chapter summarises all the findings in this research project. It also recommends potential further work based on the current work.

2. Chapter 2 -- Literature Review

2.1 Introduction

Porous Ti–based products have the potential for many applications in the structural and biomedical fields. This is due to their outstanding mechanical properties, low density and biocompatibility [19]. A detailed description of the application of porous Ti-based products is presented in section 2.2. Ti is a universal solvent at temperatures above 400°C. In particular, too high interstitial oxygen results in embrittlement of Ti. Due to the large surface area of porous Ti, a powder metallurgy route which allows the forming process to be carried out at lower temperatures, to reduce the possibility of contaminants, is therefore a promising way to fabricate porous Ti products [19, 20]. Figure 2-1 illustrates the evolution in the number of annually published research papers which study porous metals and porous Ti, respectively. In the last decade, the numbers of publications on porous metals and porous Ti has increased gradually and the number of publications on porous metals (or metal foams) has reached a maximum level in 2012. However, the number of publications in 2013 shows unexpectedly drop, which might be due to the delay in publication.

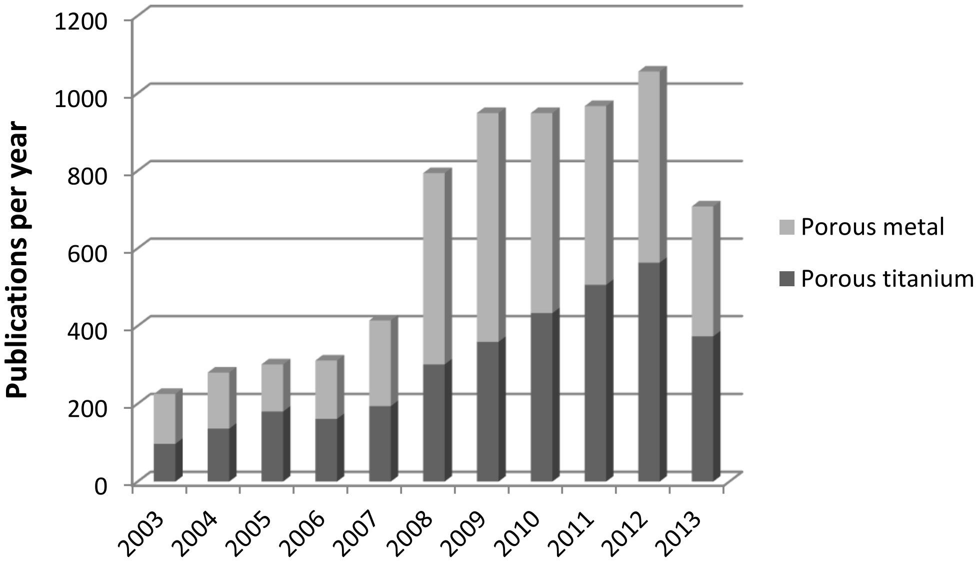

Figure 2-1 Evolution of the annual number of papers published on research related to porous Ti and porous metal for comparison. The numbers were

obtained by searching publications with the concept porous metal or metallic foams in the key words field in Scopus (i.e. KEY((metal foam) OR (cellular metal) OR (porous metal)), KEY((titanium foam) OR (cellular titanium) OR (porous titanium))), AND (LIMIT-TO(SUBJAREA, "MATE") OR LIMIT-TO(SUBJAREA, "ENGI")).

A number of powder metallurgy routes for producing porous Ti have been developed. These can be categorised into five major processes, namely powder particle sintering, hollow powder sintering, a space-holder method, sintering of powder on a fugitive scaffold and pressurised pore expansion [19]. These methods will be reviewed in section 2.3. However, making porous Ti products into the desirable shapes for specific applications is also important. Common metal forming techniques used to produce porous Ti materials are: metal injection moulding (MIM) [21], and powder compaction and sintering [9, 12, 22]. Interestingly, some researchers have investigated ceramics casting processes, such as gel casting [13], tape casting [23], freeze casting [2, 3], and slip casting [24, 25], as possibilities for the fabrication of porous Ti materials. These techniques have the advantages of being able to make complex shapes, low processing cost and good materials homogeneity. Section 2.4 will review in-depth these ceramics' shaping techniques used for porous Ti production.

To address the issue of high processing costs for porous Ti using conventional powder metallurgy routes, a slip casting process is considered to be an alternative route. Slip casting is a conventional near-net-shape ceramics technique that is commonly used to manufacture dinnerware and sanitary-ware. It is a filtration process in which a solvent based powder slurry, is poured into a plaster mould, which creates capillary forces by its porosity and absorbs the solvent from slurry. Over a period, the powder compact will be formed and dried in the mould. The viscosity of the slurry is a critical parameter in slip casting. This process involves a binder, plasticiser and dispersant for controlling the viscosity of the slurry. A slurry with too high or too low a viscosity results in a poor quality sediment [26]. Details of slurry formulation with regard to the function of each component is summarised in section 2.5. The overall processing procedures for slip casting are presented in section 2.6.

A binary powder mixture consists of both coarse and fine powder particles. Using such a binary powder mixture in the process could lower the cost of the raw powder materials and achieve different degrees of pore size and permeability in the compacts. Additionally, those compacts with coarse powder particles give better dimensional stability during sintering. A major limitation of using coarse powder particles is the limited strength of sintered compacts due to the large grains in the microstructure [27, 28]. The variation of green packing density and the final compact sintered density as a function of composition and powder particles size are summarised in section 2.7.

The mechanical properties and permeability of porous materials are considered to be important criteria for use in various applications. In sintering powder metallurgy, porosity is normally controlled by the processing variables, such as sintering temperature and time, heating rate, cooling rate, particle size of the raw powder materials and the packing density of a green compact [28]. The porosity level, pore size distribution, pore morphology and interconnectivity greatly affects the mechanical behaviour of slip cast material [29-31]. In particular, under tensile loading, interconnected pores have a more detrimental effect on the ductility of porous compacts than isolated pores, because more strain is localised around the interconnected pore region, whereas the strain distributes more homogenously throughout a material with isolated pores [30]. The effect of porosity on the properties of porous sintered metals is described in section 2.8, in terms of theoretical work and experimental work.

2.2 Applications of porous Ti products

Porous Ti products can be used for various applications depending on the degree of pore interconnectivity, as shown in Figure 2-2. Porous Ti plate is normally used in gas and liquid filtration, chemical reagent filtering, water purification, beer or wine filtration, steam filtration, etc., owing to its excellent corrosion resistance and wetting properties [32]. Using a powder metallurgy process, metallurgists at Accumet Materials, Co. have managed to produce Ti plates for filtering purposes, with a typical thickness of 0.25 mm – 0.30 mm, and up to 178mm wide × 178mm long. The plate has 50% porosity with a pore size of 10 µm [33].

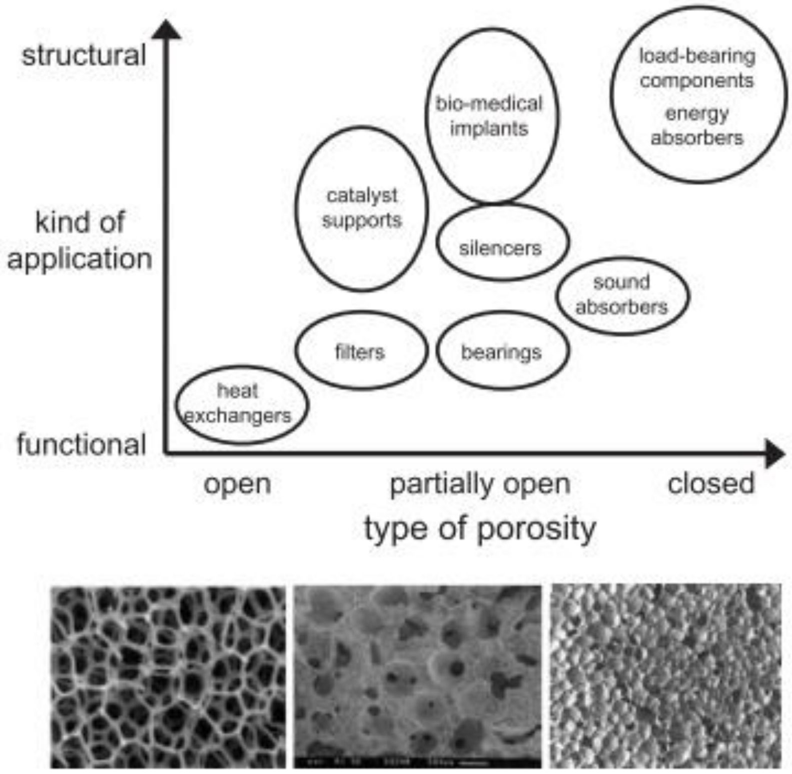

Figure 2-2 Application of porous Ti products with different levels of porosity [34].

In structural applications, Ti foams act as a sandwich core for aerospace or submarine vehicles. Dryden Flight Research Centre has applied porous Ti to the left wing of the F-16XL aircraft (Figure 2-3) to develop a laminar flow, which improves fuel economy, reduces the impact of exhaust emission in the upper atmosphere and reduces the sonic boom [35].

Figure 2-3 The porous Ti LFC glove is clearly seen on the left wing of test aircraft [35].

Compared with conventional graphite anodes, Ti anodes operate with a lower level of power consumption in an electrolysis process for chlorination of water for purification purposes. Ti-based anodes have a high current efficiency with less contamination in both the cell electrolyte and the chlorine. The Ti electrodes used for electro-winning and electro-refining of metals, such as copper, gold, nickel, manganese, and manganese dioxide, from sulphides dissolved in sulphuric acid has an environmental-friendly impact on the smelting process by avoiding a need for roasting of the sulphide ores [1].

Over the last three decades, Ti has been considered to be one of the most favourable biomaterials due to its excellent biocompatibility and its high resistance to corrosion from body fluids. Traditionally, solid Ti materials have been used for orthopaedic applications. However, a stress shielding effect can be induced at the interface between the bone tissue and the implant, which can result in loosening of the implant. Moreover, the solid structure of an implant gives a zero or low likelihood of implant fixation and bone tissue regeneration [8]. Therefore, a highly porous Ti structure is introduced for orthopaedic applications [8, 18, 36-39]. Based on clinical research, it has been shown that porous implants are biologically fixed by the ingrowth of tissue, which provides a better functionality than for solid implants [37, 38].

2.3 A review of fabrication techniques of Ti based porous products

There are a number of well-developed methods that are used to produce porous Ti, such as: powder partial sintering, the space holder method, the creep expansion process, etc. The following section reviews the techniques used to create porous Ti-based products. A schematic diagram to illustrate each process is shown in Figure 2-4.

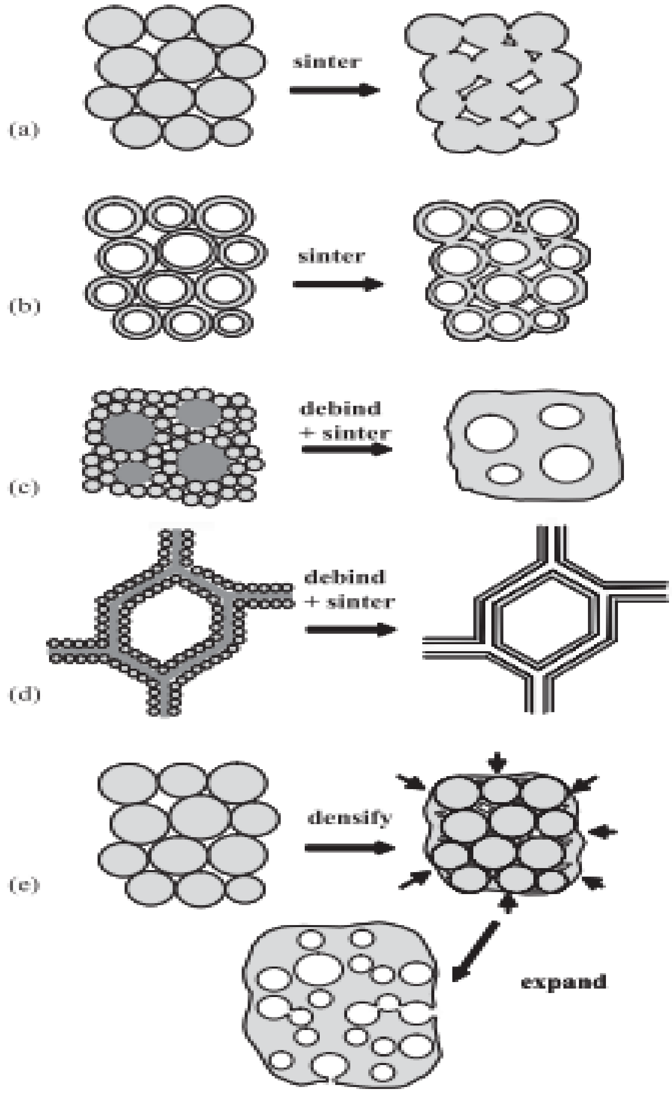

Figure 2-4 Schematic of the main solid-state processes used to fabricate Ti foams; (a) powder particle sintering; (b) hollow powder sintering; (c) Fugitive space-space holder method; (d) sintering of powders deposited on fugitive scaffold; (e) powder densification in presence of gas, and subsequent expansion of trapped gas bubbles [19].

2.3.1 Particle sintering

The simplest way to make Ti foam is to partially sinter Ti powders under isostatic pressing or loose packing (Figure 2-4(a)). Generally, this process gives a relative low porosity (less than 50%). The green compact density, sintering temperature and holding time can significantly affect the porosity level. However, with this process it is difficult to control the pore size and shape, which to a large extent depend on the shape and size of the particles. For spherical powders, pores are cusped at the sintering necks between powder particles (Figure 2-5). In addition, this method produces incomplete interconnected pores [40].

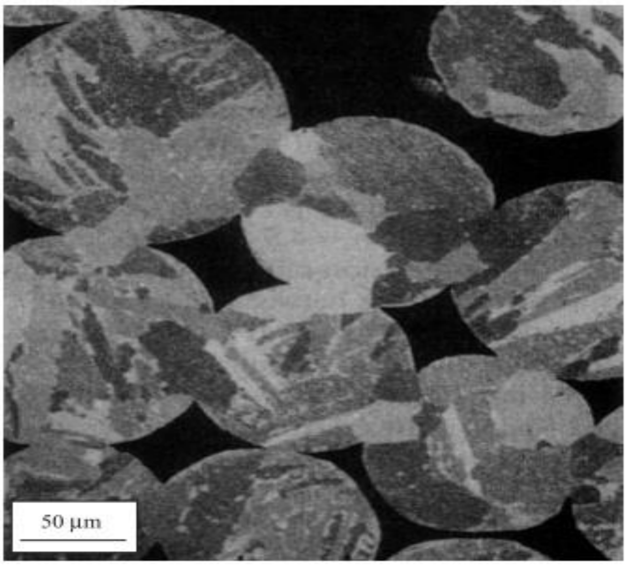

Figure 2-5 Cross-section of a foam produced by partial sintering of CP-Ti powders, showing sharp cusps [41].

Cirincione et al. investigated the effect of sintering time on the porosity of loose Ti-6Al-4V powders at 1000^{o}C. Their investigation showed that holding between 0.5 and 24 h gave porosities between 41% and 55%. The maximum compressive strength of 55 MPa was obtained at 49% porosity [42]. Oh et al. fabricated porous Ti compacts by sintering the spherical Ti powders with and without applied pressure. They produced a porosity range from 5.0 to 37.1 vol% by controlling sintering conditions and Ti powder sizes [18]. It was found that powder size and sintering pressure are the dominant factors governing the densification behaviour of porous Ti compacts. The small size of the powder particles and the high sintering pressure produce a low porosity level in the compact. For instance, in Figure 2-6(a), it is interesting to note that in a compact sintered at 1573K (1300^{o}C) there is no necking but only surface contact between powder particles (374μm), in spite of a higher sintering temperature. On the other hand, neck formation between Ti powder particles (65μm) is observed in a porous compact sintered at 1373K (1100^{o}C) (Figure 2-6(b)). Thus, smaller particles with high specific surface areas have higher energy, so that they can be sintered faster even at lower sintering temperatures.

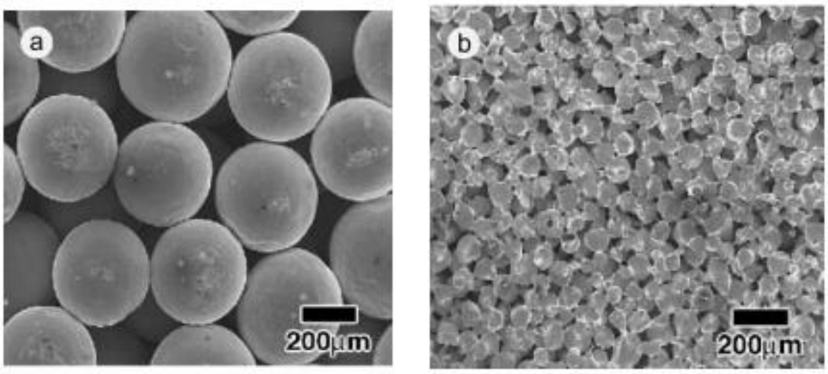

Figure 2-6 SEM micrograph of porous Ti compacts sintered at (a) 1573 K using 374 μm powder; (b) 1373 K with 65 μm powder [18].

Thieme et al. [43] produced porosities ranging from 35% to 60% for sintered Ti powders. They added 1.5 wt.% silicon to the Ti powders to produce a transient liquid phase, which accelerated the sintering process of coarse powders. Functionally graded Ti foams could also be produced by sintering a stack of three powder layers with different particle sizes and silicon content (Figure 2-7). The porosity varied from 22% at the finer powder layer (48μm) to 45 % at the coarser powder layer (200μm).

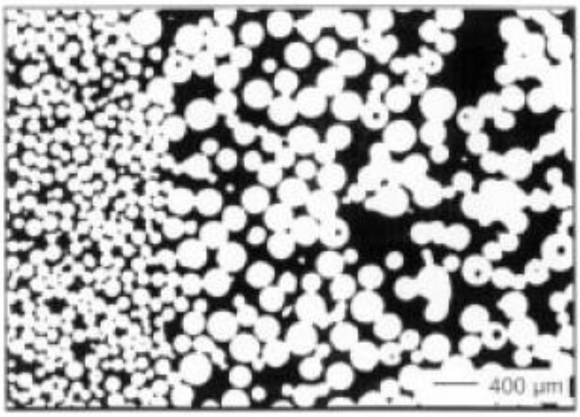

Figure 2-7 Microstructure of a graded Ti specimen [43].

2.3.2 Hollow powder

This process is illustrated in Figure 2-4(b). The basic principle is to use secondary pores produced from hollow powders to fabricate foam by sintering. This process controls the shape and volume fraction of the secondary pores, regardless of the characteristics of the Ti powder. However, a major drawback of this process is that there is the potential for contamination brought about by the binders, and also primary porosity would be formed due to incomplete sintering. In addition, this process is not suitable for uniaxial pressing to facilitate the sintering, because during pressing the secondary pores would collapse [19].

Hurysz et al. [44] injected a slurry of Ti hydride and a polymer binder in a solvent through a co-axial nozzle to produce hollow Ti spheres with dimensions of 1 to 6 mm diameter and 0.1 mm wall thickness. Once the spheres had been sintered, a porosity of around 86% resulted.

2.3.3 Space-holder method

There are two kinds of space holder materials: one is known as a solid space holder, and the other a fugitive space holder. A solid space holder normally consists of solid powders which can be easily removed, either by a burning process at low temperatures or by dissolving in a solvent, without causing excess contamination of the Ti powders. This is also a common way to make an open cell foam (Figure 2-4(c)) [45]. Ti powders are mixed with the solid space holder and then pressed under pressure. This allows sufficient green strength to be imparted to the metal powder to prevent collapse when the space holders are being removed. Sintering is the final step.

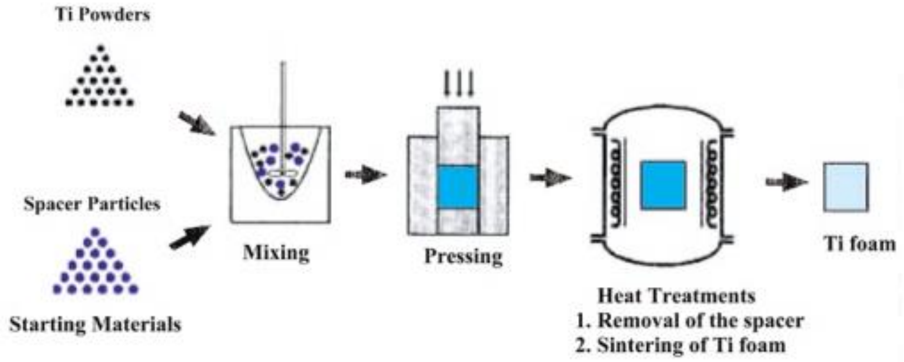

Figure 2-8 Schematic illustrations of the space-holder process for porous Ti [12].

In 1983, Wheeler et al. [46] used magnesium wires as space holders, which evaporated at 1000°C. Due to their typical shape, elongated pores were made in the Ti or Ti-6Al-4V foam. Wen et al. [12] reported a fabrication process for open-cellular Ti foams by mixing Ti powders with the ammonium hydrogen carbonate (NH_4HCO_3) particles, followed by cold compaction, removal of the space-holders and sintering (Figure 2-8). Chen, et al. [21] used sodium chloride (NaCl) as a space holder to fabricate porous Ti implants by powder injection moulding. This study shows that the NaCl content has a significant effect on the porosity level of a Ti implant (Figure 2-9). Increasing the NaCl content (30% to 60%) increases the porosity from 42.4% to 71.6%, decreases the compressive strength from 316.6 to 17.5 MPa and reduces the elastic modulus from 3.03 to 0.28 GPa. Other space-holders are also being investigated, such as carbamide (urea) [47], ammonium hydrogen carbonate [12, 22, 48], polymer granules [49], etc.

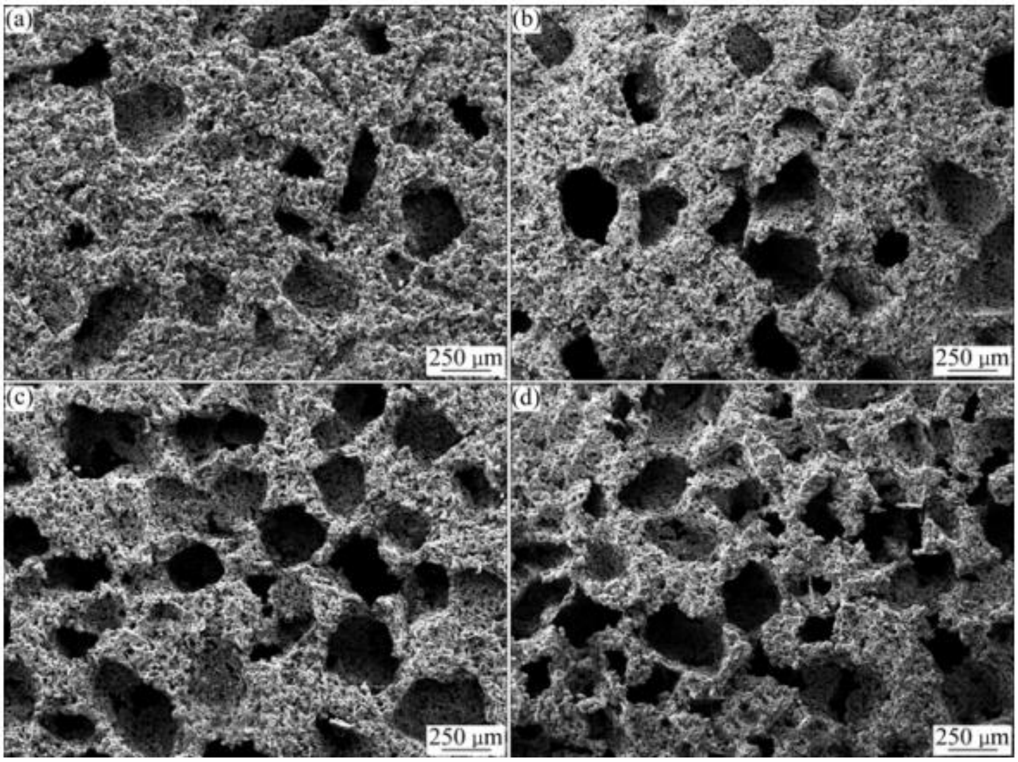

Figure 2-9 Ti implants made using NaCl as a space holder (a) 42.4% porosity; (b) 52.1% porosity; (c) 62.0% porosity; (d) 71.6% porosity [21].

2.3.4 Sintering of powders deposited on fugitive scaffold

Foams produced using a fugitive space holder uses a mixture of Ti powders and binder deposited on a fugitive scaffold (Figure 2-4(d)). After debinding and subsequent sintering, a reticulated foam is formed. An open-cell Ti-6Al-4V foam (Figure 2-10) was produced by Li et al. [40] using a polyurethane elastomeric scaffold. A high porosity level of 88% was achieved, with a compressive strength of 10 MPa. A second deposition of a powder slurry on the previously-sintered foam, followed by sintering, showed that the density and the compressive strength of Ti-6Al-4V were both improved. The porosity level decreased to 80% and the compressive strength increased to 36 MPa [50]. This is due to the healing of flaws in the Ti struts.

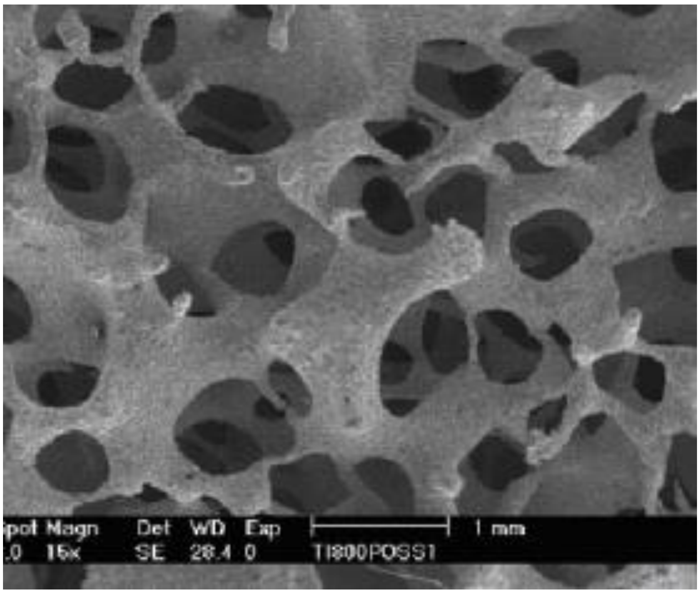

Figure 2-10 Porous Ti-6Al-4V produced using a fugitive scaffold [40].

2.3.5 Creep expansion process

The creep expansion process is illustrated in Figure 2-4(e). Kern et al. [51, 52] were the first to invent the creep expansion process to produce Ti-6Al-4V foam materials. In this process, Ti-6Al-4V powders are packed into a steel can. The can is evacuated and backfilled with argon gas to a predetermined pressure level. Then, the powders are densified by hot isostatic pressing (HIP). As a result, argon gas is entrapped within the Ti compact. After cooling and removal of the can, the Ti compact is heat treated under vacuum, which allows the expansion of the high-pressure argon gas bubbles to produce a porous body. Based on this technique, a small modification was made by Biasotto et al. [53], who used hydrogen rather than argon. In this case 5 or 10 wt.% of TiH_2 powders were used for the production of hydrogen. A major drawback of this process is that hydrogen could be dissolved in and diffused through the Ti matrix which results in embrittlement. The limitation of this process is that it can only generate modest porosities (up to 50 vol.%), because walls between adjacent pores fracture under a relatively small strain. It allows for the merging of pores with each other and with the billet surface, which leads to the escape of the foaming gas [19].

2.3.6 Superplastic expansion process

An improved technique based on a creep expansion process (section 2.3.5) is known as superplastic expansion, which induces superplasticity in the Ti matrix during foaming. This process has faster deformation rates and a higher tensile ductility [19, 54]. Dunand and Teisen [55] first used transformation superplasticity for solid-state foaming of CP-Ti and Ti-6Al-4V. Later, Murray and Dunand focussed on the evolution of pore microstructure for specimens superplastically foamed under thermal cycling conditions (830 and 980 °C) [7, 54, 56, 57]. In Figure 2-11, the pores are mostly rounded and generally equiaxed when foaming for 8 hours, with pore sizes ranging from 2-3 μm to 100 μm. During the next 18 hours of thermal cycling, the pore size increased and internal pore coalescence occurred. The porosity level was kept close to constant which indicated that the gas pressure was too low to influence any further expansion.

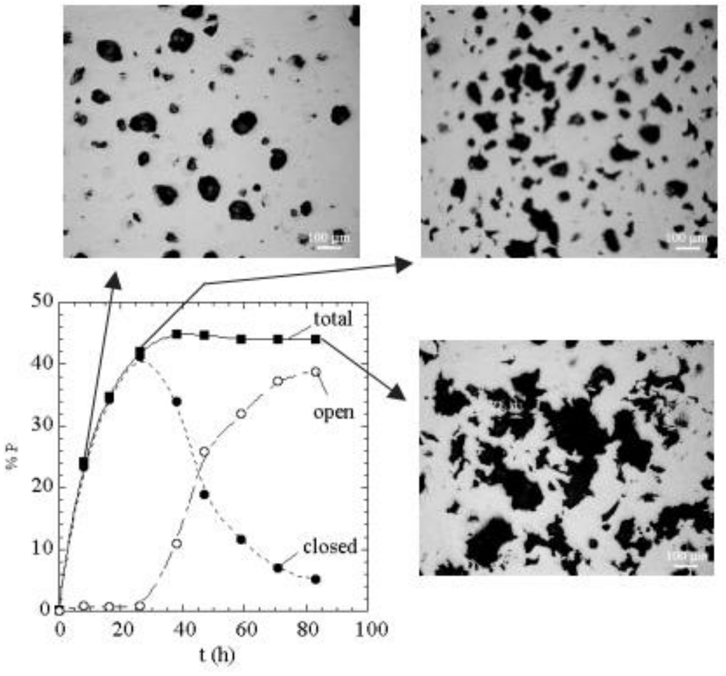

Figure 2-11 The superplastic expansion process; the porosity level varies as a function of time [54].

2.4 A review of powder casting techniques

A number of porous Ti fabrication processes have been reviewed above. Recently, some researchers have investigated ceramics’ casting processes on the fabrication of porous Ti materials, such as gel casting, tape casting, freeze casting and slip casting. These techniques have an advantage of making products in near-net-shapes. However, the development of stable metal powder slurries provides significant challenges. This is because metal powders are larger in size than those used for ceramic processing and have a higher density, producing more difficult to keep suspended. A detailed review will be presented in the following sections.

2.4.1 Gel casting

Gel casting is a ceramic forming process that first invented in the 1990s by Janney et al. [58]. The formation of a cross-linked polymer aqueous solution gel as the setting mechanism is the key point in gel casting [59]. There are some gel casting research have been done on metals, such as nickel-based superalloy [59], steel [60], etc. Erk et al. [15] demonstrated the feasibility of a gel casting process to fabricate porous Ti in complex shapes. A unique porous Ti screw for implant applications was fabricated with a 20 vol.% porous core and a higher porosity near the surface (Figure 2-12). Gel casting has the advantage of low processing cost, and produces a strong green compact. However, it involves a long processing time. In the case of air bubbles trapped in the compact, it will result in deterioration of mechanical properties.

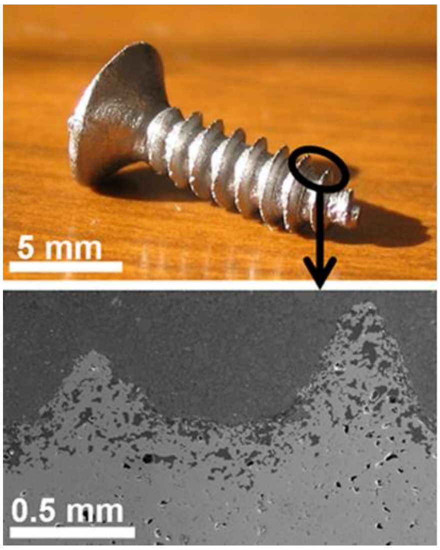

Figure 2-12 Photograph and SEM cross-sectional micrograph of a gel-cast and sintered Ti screw [15].

2.4.2 Tape casting

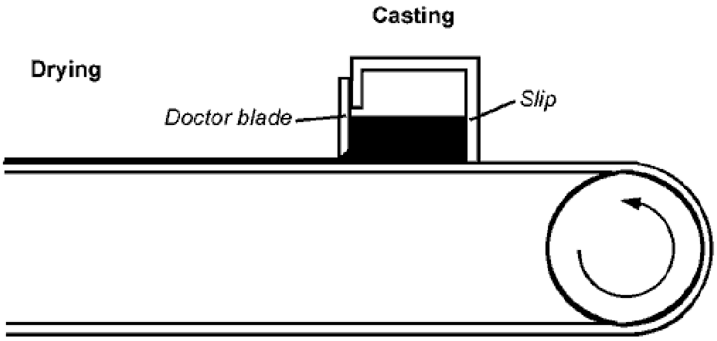

Figure 2-13 Tape casting process [61].

In tape casting, the slurry is deposited on a strip carried by rollers (Figure 2-13). The slip flows continuously from a reservoir through an adjustable slot onto the strip. Hot air is blown over the strip in the opposite direction to dry it. Typically, tape casting could manufacture parts with thicknesses ranging from 0.25 mm to 1.0 mm [61]. Rak and Walter [23] obtained a porous Ti sheet with a thickness of 370 μm by tape casting a mixture of Ti and Ti hydride slurry, followed by ambient temperature drying then sintering. Less than 0.2 wt.% Ti hydride powder was used as a reducing agent to improve the sinterability of the Ti powder. This technique opens up an alternative way to manufacture porous or fully dense Ti sheets.

2.4.3 Freeze casting

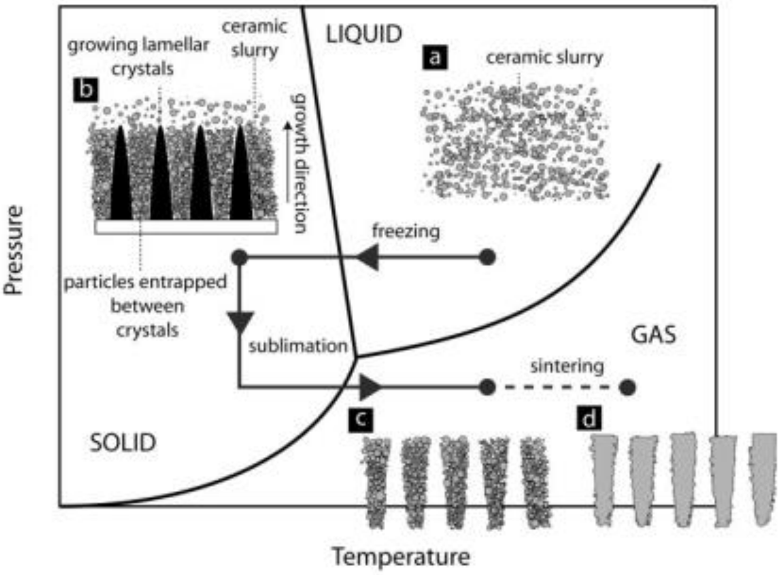

Figure 2-14 The four processing steps of freeze casting: (a) slurry preparation; (b) solidification; (c) sublimation; (d) sintering [62].

Freeze casting consists of freezing a powder slurry, followed by sublimation of the freezing vehicle from the solid to the gas state, and subsequent sintering to give final densification and strength, as shown in Figure 2-14. During the sintering stage, microporosity created from the powder packing can be removed, but the macroporosity created by the solvent crystals is retained [62].

Recently, researchers have demonstrated that freeze casting is one of the most useful methods for producing porous Ti [2-6]. They used either water [4-6] or camphene [2, 3] as the freezing vehicle, which is frozen to below their solidification temperature. As a result, the growth of the freezing vehicle produces an interconnected structure, which leaves interconnected pores in the compact after freeze- drying. In particular, the cooling rate and the cooling time can govern the size and morphology of the freezing vehicle; which in turn means that the size and morphology of pores can be controlled. A typical example is shown in Figure 2-15. The porous Ti scaffolds were produced by freezing casting using camphene as the freezing vehicle [2]. The size of pores increased significantly from 144 ± 21 µm to 271 ± 15 µm with an increase in the freezing time from 1 day to 7 days.

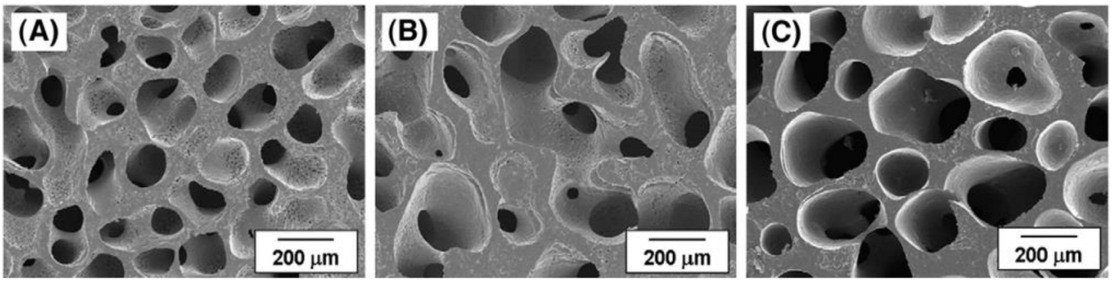

Figure 2-15 SEM micrographs of the porous Ti scaffolds produced by freezing casting with various freezing times of (A) 1 day, (B) 4 days, and (C) 7 days [2].

2.4.4 Slip casting

Slip casting is a well-established technique used for the large-scale fabrication of ceramic substrates. Firstly, the slurry is cast into a plaster mould, the water is removed by capillary force, and a consolidated layer consisting of packed particles builds up [61]. When a desirable thickness has been reached the excess slip is removed (drain casting), or the casting proceeds until the casting fronts approach each other and a solid body has been obtained (solid casting). Finally, the cast is sintered to achieve the final densification.

Neirinck et al. [17] worked on the slip casting of a slurry mixture of Ti and Ti hydride powder to form a green compact, through absorption of a solvent by a plaster mould, followed by sintering. They produced Ti products with a high porosity level ranging from 55 vol.% to 65 vol.% for implant applications. However, safety is a major concern with this process due to the high reactivity of Ti hydride powder. The compressive strength varied from 121 MPa to 141 MPa. Ohkawa et al. [16] fabricated Ti products with a relatively low porosity level, ranging from 4 vol.% to 20 vol.%, by slip casting of a pure Ti powder slurry. The tensile strength obtained varied from 200 MPa to 300 MPa with a negligible amount of elongation. In addition, TiC was detected by X-ray diffraction (XRD) due to contamination from the binder. Nevertheless, to date there are no reported investigations on the slip casting of Ti powders with a view to achieving a controlled level of porosity, acceptable mechanical strength and an interconnected pore structure. As a result, a more in-depth literature review on the slip casting process is given in the next sections.

2.5 A review of slurry formulation in slip casting

Table 2-1 Summary of aqueous slurry additives system for slip casting.

Powder	Solvent	Dispersant	Plasticiser	Binder	Ref.
Ti	Water	Sodium alginate			[16]
Ti & Ti hydride	Water	Cyclohexane		Poly vinyl-butyral (PVB) dissolved in ethanol	[17]
Copper	Water	Sodium alginate			[63]
Stainless Steel	Water	Ammonia alginate			[64]
$La_{0.8}Sr_{0.2}CrO_3$	Toluene & 2-propanol	KD1^{TM}	Di-n-butyl phthalate & Polyethylene Glycol	PVB	[65]
Hydroxy-apatite	Water	Polyacrylic acid (PAA)		Polyvinyl alcohol(PVA)	[66]
Hydroxy-apatite	Water	Calgon Darvan C			[67]
Alumina	Water	PAA			[68]
Alumina	Water	Ammonium polyacrylate			[69]
Alumina	Water	Darvan C Dolapix CE64 Duramax D3005			[70]
α-Sialon	Methylethyl-keton and ethanol	KD1^{TM}			[71]

Slurry formulation is the most important stage in making a good slip casting. In general, there are five components in the powder casting, namely: powder, solvent, binder, plasticiser and dispersant. Each component has a different effect on the rheology of a slurry and on the density and mechanical properties of a casting, etc. Table 2-1 summarises information from the literature on the aqueous slurry additive systems used for slip casting of metal and ceramics powder. The following sections describe and explain in detail the effects resulting from each component, along with the research studies based on these.

2.5.1 Powder

To obtain a suitable slip, a well-characterised powder is essential. In general, a small particle-sized powder would have a high specific surface area. This would allow an effective packing of particles. One disadvantage of using a small particle-sized powder, is that higher cast shrinkages are produced and higher concentrations of additives are required [72].

A number of studies have been conducted based on the use of ceramics' powders, in terms of particles size distribution, solids contents level, etc. By mixing a different proportion of powders of different particle size, a higher packing density could be achieved [73-76]. Tari [74] blended a coarse and fine alumina powders together and a maximum value of about 74% of the theoretical density was obtained. A more detailed description will be reviewed in section 2.7.

The optimum solids content level is determined by the viscosity of a slurry. However, slip casting requires a certain degree of fluidity in a slurry in order to be able to cast it into a mould. Li [40] has studied the powder particle shape and the effect of solids content level on the rheology of a Ti-6Al-4V slip. The study showed that spherical particles, with the smallest size, yield the lowest amount of sediment and have the least viscosity. It was found that there is a sharp increase in the viscosity of a slurry once the solid content increases to 75 wt.% of Ti-6Al-4V powders (Figure 2-16).

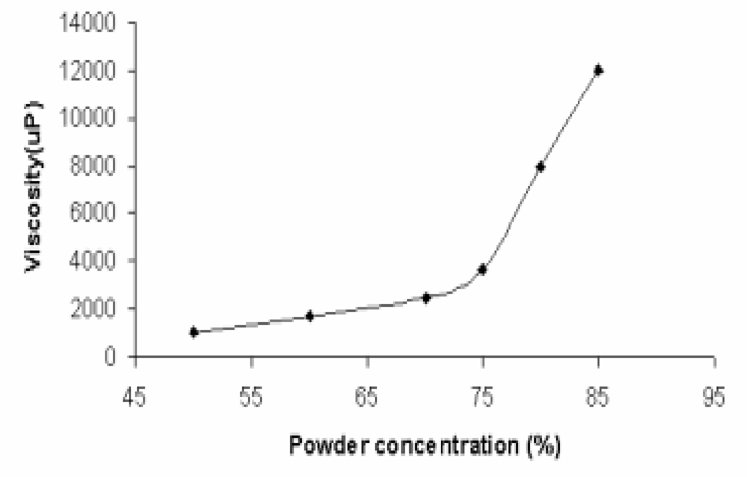

Figure 2-16 Viscosity change with solids content level of Ti-6Al-4V powder [40].

The Krieger-Dougherty (K-D) equation describes theoretically the rheological behaviour of a slurry as the volume fraction of solids loading changes [77]:

$$\eta_r = \frac{\eta}{\eta_o} = (1 - \frac{\phi}{\phi_m})^{-[\eta]\phi_m} \tag{2-1}$$

where η_r is the relative viscosity, η_o is the viscosity of the medium, $[\eta]$ is the intrinsic viscosity, ϕ_m is the maximum packing fraction and ϕ is the volume fraction of particles in the suspension. The K-D equation assumes that the particles in a slurry are spherical. The expected packing fraction is 0.62 for close packed spheres of equal size.

2.5.2 Solvent

A solvent is an important component for making a slip in the slip casting process. It offers a media for powder interactions and the interaction between the powder and organic additives. The most commonly used slurry is either water-based [66, 69, 78-81] or ethanol-based [82]. The pH of the solvent has an effect on the stability of slip and normally, this also needs to take into account the type of dispersant. This will be discussed in depth in the next section.

Although an organic solvent is commonly used as a dispersion media in colloidal processing due to its excellent compatibility with organic additives, water is emerging as an alternative because it is environmentally friendly, low cost and safe. Metal powder – water systems have been employed in colloidal processing by some researchers. Sánchez-Herencia et al. [14] demonstrated colloidal processing using aqueous nickel powder suspensions to produce porous or dense compacts, which consist of a 77 wt.% solids loading, 0.5 wt.% carrageenan acting as a gelling agent on cooling with a balance of deionised water. Takeda and Minagawa [64] developed a stainless steel slurry to produce dense compacts using a slip casting process, with a slip consisting of 82.7 wt.% powder, 0.3 wt.% ammonium alginate as a binder and the balance water.

2.5.3 Dispersant

A dispersant is used to coat the powder particles to make a stable suspension (also known as deflocculated) in the slurry due to steric and/or electrostatic repulsion. In general, the van der Waals force is the dominant attractive force between particles, which could cause flocculation. A combination of both steric and electrostatic mechanisms, known as electrosteric, has been proposed to obtain better stabilisation. In Figure 2-17, it is illustrated the behaviour of flocculated suspension and deflocculated suspensions. The flocculated suspension shows a random packing structure whereas the deflocculated suspension showed an ordered packing structure. The most frequently used dispersants for slip casting are polyelectrolytes, such as Dispex A40, Dispex N40, Darvan C, Dolapix CE64, etc. Most of them are sodium salts or ammonium salts of poly(acrylic acids).

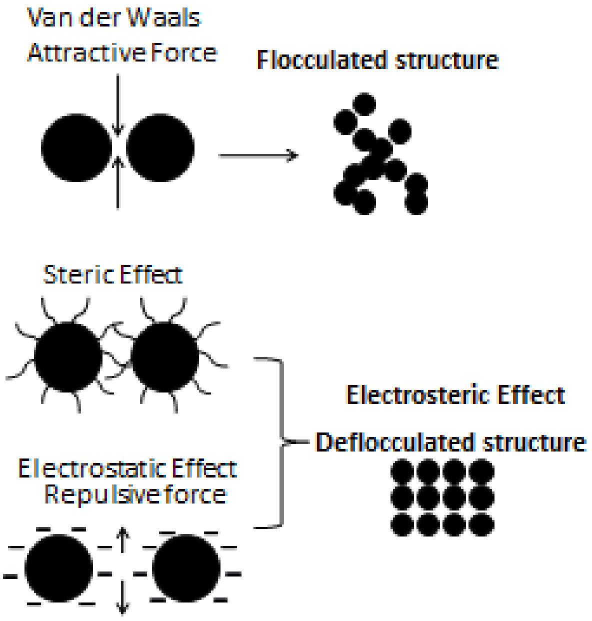

Figure 2-17 An illustrate of the flocculated structure and deflocculated structure.

As mentioned before, the pH value of the solvent is of particular importance due to the formation of electrostatic double layers, which would give high surface potentials and produce repulsive Coulomb forces on the particles. Surface charging in an aqueous environment is due to protonation or hydroxylation of surface hydroxide groups, resulting in a positive or a negative surface charge respectively [83].

Measurements of the zeta potential or isoelectric point (iep), and the streaming potential of an aqueous suspension could give indications of the effectiveness of a dispersant, in terms of pH value and/or dispersant amount [84-87]. In slip casting, the dispersants are normally negative polyelectrolytes. The zeta potential and streaming potential become more negative at the beginning, due to an increase in the amount of polyelectrolyte adsorbed onto the surface, and then they reach a constant plateau. However, sometimes, an increase in the ionic strength leads to a compression of the electrical double layer around each particle causing particles to settle more easily, providing a clear supernatant [88].

Other measurements to optimise the dispersant are to test the viscosity of a slurry, and compare the sedimentation rate and sedimentation height. By observing the sedimentation behaviour of the slurry, it can also tell if it is flocculated or deflocculated, as illustrated in Figure 2-18. Initially, the flocculated suspension will produce a clear supernant whereas the deflocculated suspension will remain cloudy. Over a long period of time, the particles settle down due to the force of gravity, and at a later stage, the flocculated suspension forms porous sediment whereas the deflocculated suspension gives dense packing sediment which is rather difficult to re-disperse. In Figure 2-19, the minimum point of the graph shows the optimum amount of dispersant.

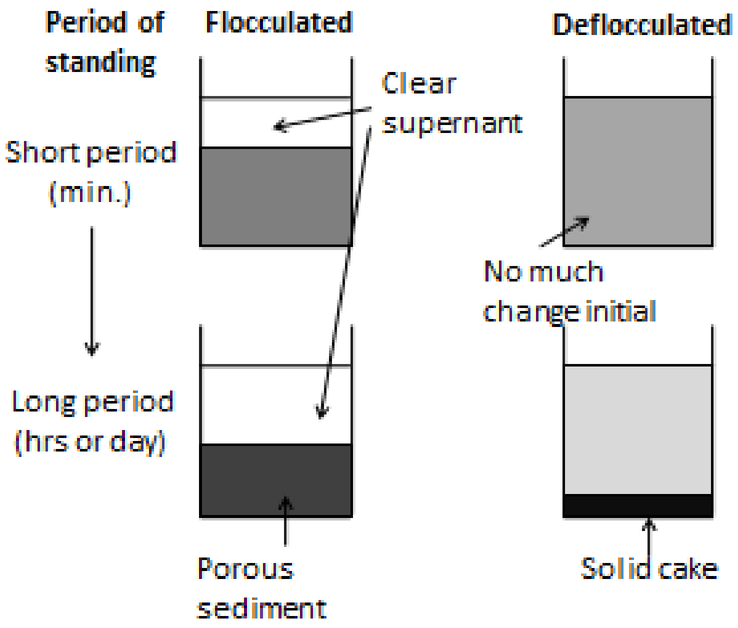

Figure 2-18 An illustrate of sedimentation behaviour of both flocculated and deflocculated slurries.

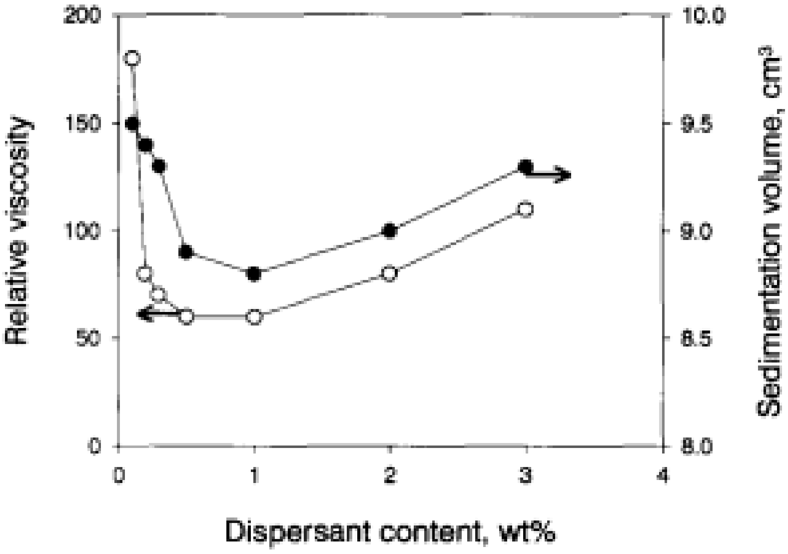

Figure 2-19 Relative viscosity and sedimentation volume of alumina/water suspensions as a function of dispersant amount [89].

2.5.4 Binder

The binder provides strength to a green casting through organic bridges between the particles after the drying process. Organic binders are either dissolved or dispersed in water as an emulsion. Most soluble binders are long chain polymer molecules [83].

In general, two groups of substances have usually been used as binders for aqueous casting of ceramics: vinyl or acrylic–type polymers and cellulose ethers. The vinyls group are represented by a linear backbone consisting of carbon-carbon bonds, with a side group attached to every other atom. The acrylics are characterised by two side groups attached to the carbon atom.

To optimise the binder concentration, experiments must be done carefully. If the binder content is too low the green casting body would develop cracks and if it is too high there might be many voids in the body. In general, a compromise must be found between strength and density, because increasing the binder content would increase the slip strength and decrease the green density (Figure 2-20).

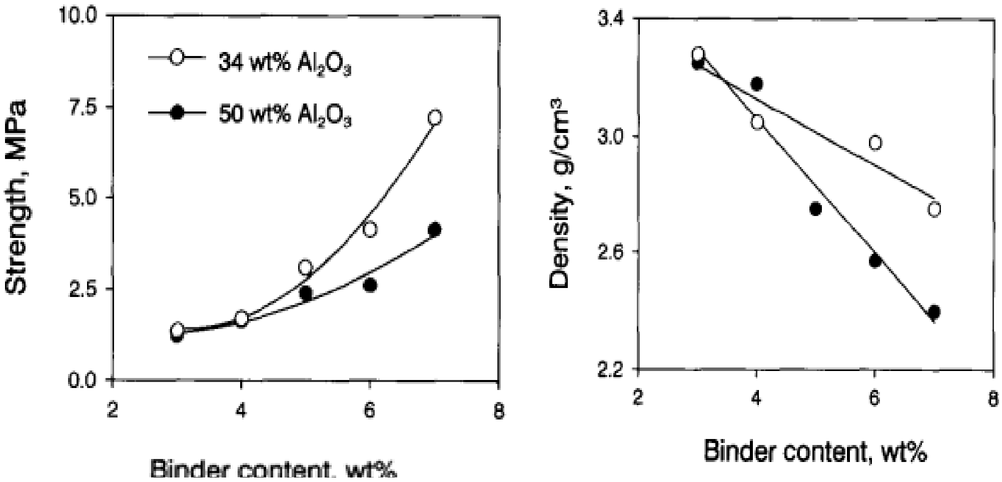

Figure 2-20 Strength and green density of alumina green slips with different powder charges as a function of HEC wt.% [90].

The rheology of a slurry is strongly affected by the binder. Typical values of a suitable slip are in the range of ≈ 0.1 to ≈ 20 Pa s for a shear rate of 50 s^{-1} at room temperature [79, 83, 89, 91, 92]. A pseudoplastic slip is also called a “shear – thinning” slip, which displays a decreasing viscosity with an increasing shear rate [83]. This shear thinning behaviour is usually associated with the slurry structure. At low shear rates, liquid is immobilised in the voids within a floc and the floc network. As the shear rate is increased, the flocs and floc network break down and the entrapped liquid is released and a more ordered structure in the flow direction is formed [74]. A suspension of solid particle tends to settle out in the water if the particle size is larger than 1 µm. In this case, a casting slip would not remain homogeneous if settling occurred. One approach is to increase the binder content in order to increase the viscosity. In the meantime, the slip must be fluid enough to flow into the mould. Therefore, a pseudoplastic solution is utilised. At high shear force, as in casting a tape or other body, the viscosity of the slip may be lower. Once poured, the slip does not run away [92].

2.5.5 Plasticiser

Plasticisers are organic additives that soften the binder in the dry or semidry state. In general, they have a lower molecular weight than the binder and are soluble in the same solvent. The plasticiser breaks the close alignment and bonding of the binder molecules. As a result, this increases the flexibility and workability of a slip.

The most important effect of the plasticiser is to reduce the gel formation temperature, T_g (Figure 2-21). The gelled liquid would have a much slower drying rate because the liquid does not flow to the surface during drying. Water must leave the body by diffusion within the gel structure. Thus, the ratio between the binder and plasticiser needs to be controlled.

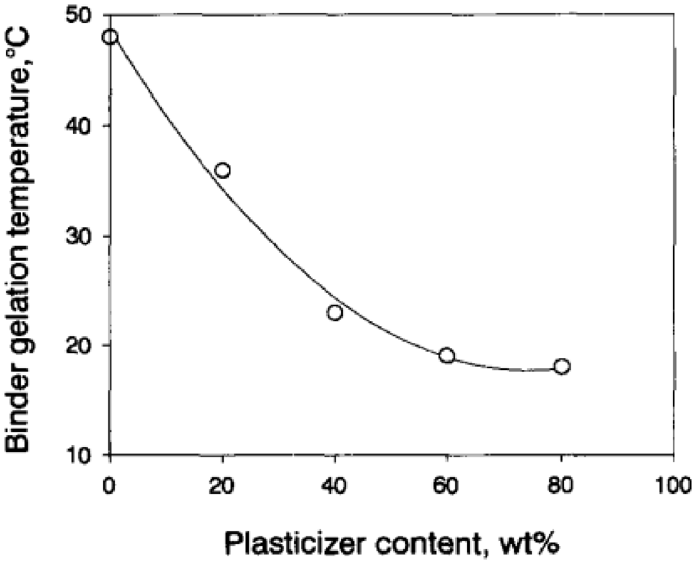

Figure 2-21 Effect of the plasticiser content on the binder, T_g; the plasticiser is PEG and the binder is PVA [83].

2.6 A review of processing of slip castings

The following sections will review one by one the processes involved in slip casting and will present the effects of various parameters that have been investigated by researchers.

2.6.1 Milling

Most of the milling procedures involve two or more stages [78, 92, 93]. The first stage associated with milling is to prepare a slurry of low viscosity, consisting of water, dispersant and powder. This step is to break up agglomerates and to distribute dispersants uniformly on the surfaces of the powder particles. In the second stage, a plasticiser and binder are added to make a more viscous slurry [83].

The milling procedures have been investigated by a number of researchers. The time duration of the milling process can vary from as little as 4 hours to as long as 48 hours. Mistler cited a typical milling time of 24 hours based on his team's experience [92]. This is a time-dependent process because the breaking of an agglomerate would possibly use significant amounts of energy. With incomplete milling, the agglomerates on the surface of the slurry can be observed (Figure 2-22).

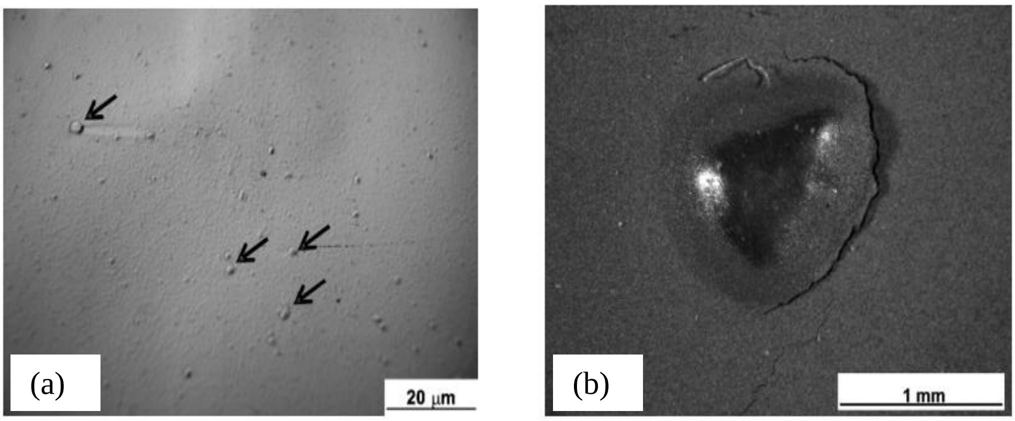

Figure 2-22 (a) Optical micrographs showing agglomerates of binder on the surface of a slurry; (b) "Zipper-bag" effect where an agglomerate is encased in the binder [78].

2.6.2 De-airing

Immediately after milling, the slip has all the required ingredients. The next step is to de-aerate the slip to remove any air that may have been entrained during the milling and mixing process. Air bubbles cause defects in a slip-cast product. Pinholes are the most common defect and also cracks could radiate out from pinholes upon drying, to create a feature known as “crow feet” (Figure 2-23)[78, 92].

The most common technique for de-aerating a slip is to use a partial vacuum with gentle stirring or agitation. Agitation tends to lower the viscosity in a pseudoplastic slip, which indicates that the air removal would be much easier. The vacuum level is normally in the range of 635 to 700 mm of Hg. Too high a vacuum would remove a large volume of solvent along with the air bubbles. The duration of de-aeration varies depending on the volume of a slip. Also the viscosity of a slip affects the de-aeration process. High viscosity slips are much more difficult to de-aerate than low viscosity slips. Another technique for removing air bubbles is to use a slow rotation on a set of rollers with less than 10 rpm [92].

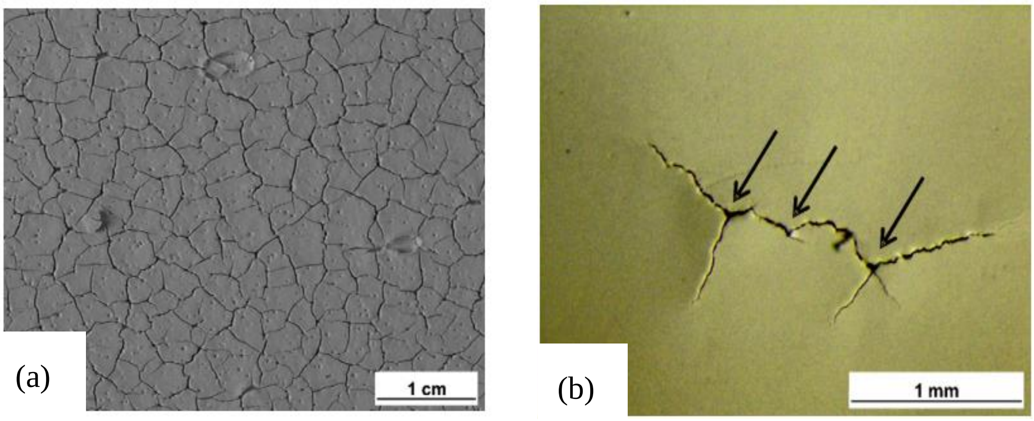

Figure 2-23 (a) pin-holes (b) Two joined “crow’s feet” due to insufficient degassing of the slip prior to casting [78, 92].

2.6.3 Debinding

Debinding is the second stage of the overall process. Unlike ceramics materials, debinding is quite crucial for Ti because it is more likely to be contaminated by oxygen, carbon and hydrogen. Its purpose is to remove the binders from the casting and is similar to the debinding process in powder injection moulding

(PIM). The binder content to be removed from a casting is important because a sudden internal vapour pressure can build up which could result in severe deformation at the sintering stage. In other words, it is desirable to obtain a defect–free product, as any defects would affect the final mechanical strength [94].

A number of binder removal techniques have been investigated. The debinding process deals with Ti, which is very sensitive to oxygen; it would not be the same as a ceramics' binder burnout process that is carried out in air. The common techniques are thermal debinding and solvent debinding [95]. In this case, solvent debinding is not feasible for slip cast compacts because the solvent could dissolve the slip cast compact and return it back to the slurry form again. Thermal debinding generally involves two types of process; one is carried out under a vacuum [96] and the other is carried out under inert gas at atmospheric pressure.

To obtain a defect–free product, two essential criteria must be considered; one is the rate of debinding, and the other is the level of carbon residuals. Too fast a rate of debinding results in cracks or blisters (Figure 2-24); on the other hand, too slow a debinding rate becomes too costly for mass production. Carbon residuals are always a common problem during debinding, as the final mechanical strength would be affected by them. Carburisation arises from binder decomposition, an inert atmosphere and a fast heating rate. Carbon enrichment will occur if carbon has not been completely removed when the process temperature reaches about 450°C [97].

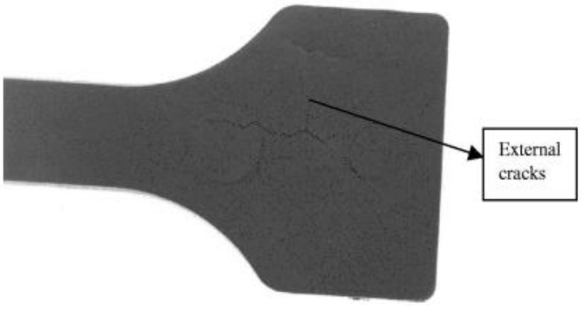

Figure 2-24 External cracks due to high debinding rate [94].

In general, there are three stages during a typical thermal cycle. The first stage involves thermal expansion of the powder and binder and melting of the binder. A hydraulic pressure develops due to the thermal expansion mismatch between the powder and binder, and it continues to be the dominant force on the compact as long as the compact remains saturated with binder. This pressure can lead to slumping of a compact and the amount of slumping is dependent on the thickness of the part [98]. Therefore, a multi-component binder with different thermal properties is preferred because this kind of system is better for accommodating this pressure than a single binder system. The next stage is to evaporate the low molecular weight components at the surface. Capillary forces move liquid binder from the centre of a compact to the surface where evaporation can continue. However, the porosity in a compact allows binder evaporation to occur in the interior and escape through the interconnected network of porosity. The final stage is to thermally decompose the remaining binder at a higher temperature. High levels of open binder-free porosity at this stage allows faster binder removal rates [97].

2.6.4 Sintering

As defined by German [28], sintering is a microwelding process for bonding powder particles together into a solid structure via mass transport that occur largely at the atomic level. A sintering process has four main stages, namely an adhesion stage, an initial stage, an intermediate stage and a final stage. Each sintering stage displays different geometric forms, as presented in Table 2-2. Moreover, as illustrated in Figure 2-25, the pore structure is irregular at the initial stage, depending on the green powder packing structure. As the pore structure becomes rounded, discrete particles are less evident and the solid structure is more coherent.

Table 2-2 Classic stages of sintering [28].

Stage	Process	Surface Area Loss	Densification	Coarsening
Adhesion	Contact formation	Minimal unless compacted at high pressures	None	None
Initial	Neck growth	Significant, up to 50% loss	Small at first	Minimal
Intermediate	Pore rounding and elongation	Near total loss of open porosity	Significant	Increase in grain size and pore size
Final	Pore closure, final densification	Negligible further loss	Slow and relatively minimal	Extensive grain and pore growth

The sintering process is sensitive to many factors, such as particle size, sintering time, sintering temperature and green density, etc. Table 2-3 highlights some key processing changes during sintering, which have been classified into either positive and/or neutral effects, or negative effects on the properties of materials and the cost efficiency of the process.

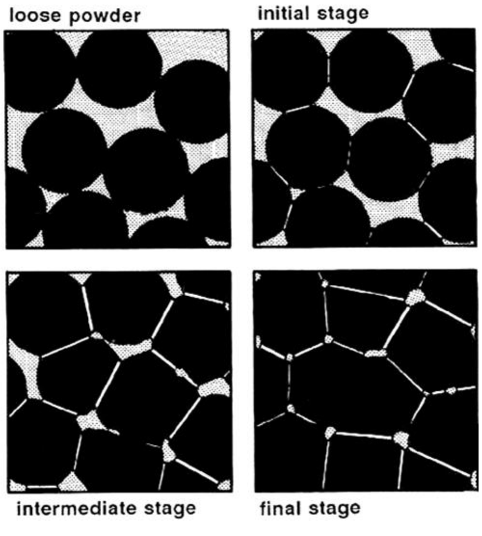

Figure 2-25 A schematic diagram of the four sintering stages starting with a loose powder structure [28].

Table 2-3 Effects of sintering process variables on the sintering process [28].

Change to a Sintering Aid	Positive and/or Neutral Effects	Negative Effects
Decrease in particle size	Faster sintering	Greater expense Higher impurity level Increased hazards
Increase in time	Grain growth and coarsening	Greater expense Reduced productivity
Increase in temperature	Grain growth Higher properties	Greater expense Less precision Greater shrinkage Furnace limitations Pore coarsening
Increase in green density	Less shrinkage Smaller pores Higher final density Uniform dimensions	Density gradients
Increase in alloying/additives	Higher strength	Homogeneity problems Higher sintering temperatures
Use of sintering aids	Faster sintering Lower sintering temperatures Grain growth control	Embrittlement Distortion

In powder metallurgy, the sintered density, porosity and mechanical properties of Ti compacts can be affected by sintering conditions, powder particle size and shape, alloying elements, interstitial elements, etc. Oh et al. [18] fabricated porous Ti with a porosity ranging from 5.0 to 37.1 vol.% by sintering spherical Ti powder particles. Their work showed that the initial powder size and sintering pressure are two dominant factors in controlling the densification process of porous Ti compacts, whereas sintering temperature has only a small effect. A sintering study examined the effect of sintering atmospheres on the density and mechanical properties of sintered Ti compacts, revealing that at similar levels of sintered density, those Ti compacts sintered in argon had much lower tensile properties than those sintered under vacuum [99]. Recent research has shown that additions of alloying elements (Fe and Zr) to Ti powder could enhance the sintering densification of Ti compacts prepared by powder injection moulding, but the mechanical properties were not improved [100]. Moreover, Qian [101] has summarised the tensile properties of cold compacted and sintered Ti as a function of oxygen content. At a similar level of sintered density, an increase in oxygen content increases the strength of sintered Ti compacts, whereas the ductility decreases.

2.7 A review of particle size distribution effects

In this section, the effect of particle size distribution (PSD) on green packing density and the final sintered density of compacts are described below.

2.7.1 Green packing density

Many studies have established the relationship between the particle size distribution in a powder mixture and the packing density [102-108]. The basic mechanism for powder packing in a binary powder mixture is for fine powder particles to fill the interstitial spaces between coarse packed powder particles, without an increase in volume. This reduces the porosity, as illustrated in Figure 2-26. X_L is the volume fraction of coarse particles in the powder composition. The maximum packing density (V_{max}) is achieved when all the voids between the larger particles after packing are filled with small particles.

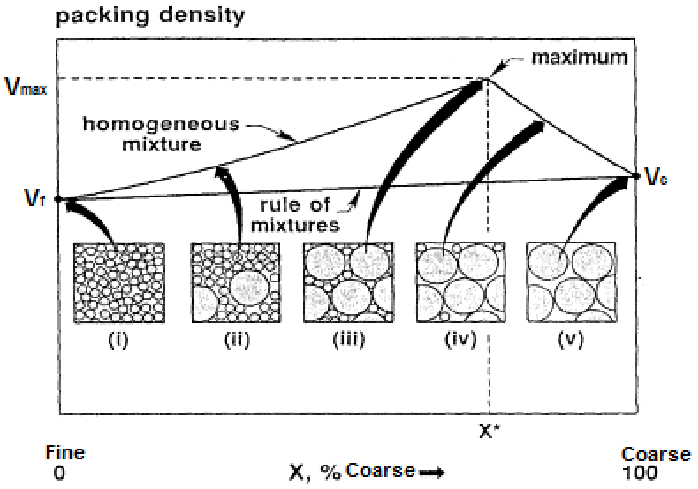

Figure 2-26 Packing density variation with composition for a bimodal mixture [109].

In 1931, Furnas developed a mathematical model to predict the maximum packing density of a two component mixture of coarse and fine particles [105]. The equation is given below:

$$V_{\max} = V_c + (1 - V_c)V_f \tag{2-1}$$

When the fine particle content is 100%, the fractional packing density is V_f and for 100% of coarse particles, the fractional packing density is V_c. The assumption made in this model is that the size ratio between coarse powder particles and fine powder particles is infinitely large. However, Westman showed that Furnas's model is not accurate for predicting the maximum packing density when taking the particle size ratio into account, as shown in Figure 2-27 [102, 103]. The straight lines correspond to Furnas's model, when the size ratio is infinite and the curved lines indicate an alteration to the packing density based on the particle size ratio using Westman's model. Zheng et al. [102] developed an improved empirical relationship to predict the packing density (V_{mix}), which takes into account the particle size ratio, the volume of fine particles and the initial packing density, as shown below:

$$V_{mix} = V_c + (1 - V_c)V_f F_1(X_f)F_2(R) \tag{2-2}$$

where X_f is the volume of fine particles, $F_1(X_f)$ is a function of the volume of fine particles, $F_1(X_f)$ = $[e \square X_f \square \ln X_f]^{\frac{5}{4V_c}}$ and R is the average particle size ratio if the pure coarse or fine particles are not exactly monosized particles, $F_2(R)$ is a function of the size ratio of coarse particles to fine particles, $F_2(R)$ = $\exp(-\frac{4}{R})$. However, this model gives a better fit with monosized particles and when the packing efficiencies for both coarse and fine particles are the same.

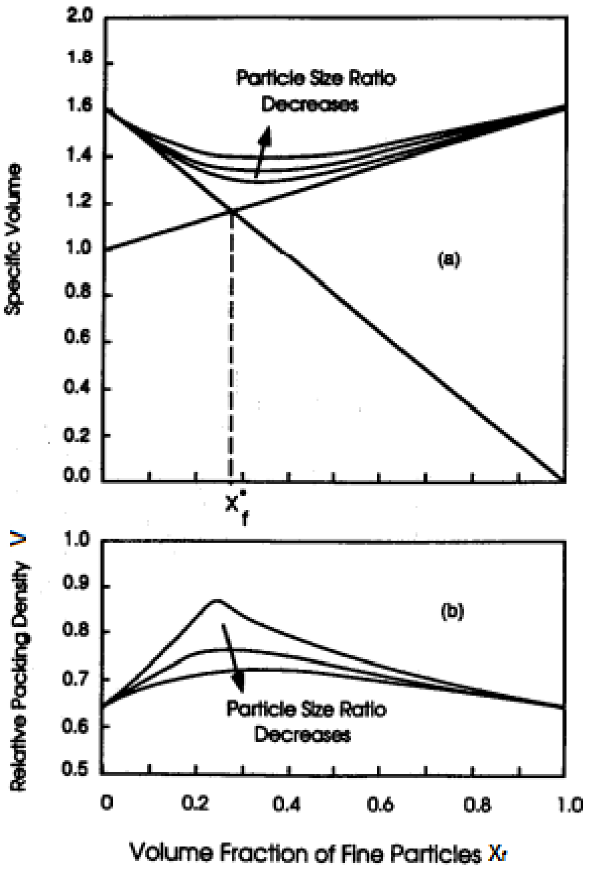

Figure 2-27 The furnas model. (a) The Westman-Hugill plot of the Furnas model; (b) The Furnas model plotted as the packing density versus particle volume fraction [102].

2.7.2 Sintered density

For binary powder mixtures, two factors govern the final sintered density of compacts: the first is the green packing density of compacts and the second is the sintering condition [28]. In general, for a low sintering temperature and short sintering time, the green packing density variation with composition is dominant. In other words, the maximum sintered density of a compact occurs at the optimum mixture of coarse and fine particles which gives the maximum packing density. For a high sintering temperature and long sintering time, a compact made using 100% fine powder particles would be more likely to produce the highest sintered density. Figure 2-28 illustrates the green density and sintered density for a mixture of 9 μm and 1 μm molybdenum powders [110]. The highest sintered density occurs with 100% fine powder particles, even though this has the lowest green packing density. This is because when the small particles constitute the bulk of the structure, large particles generate stresses that inhibit densification [28]. Smith and Messing [111] investigated the bimodal sintering behaviour of a mixture of 5μm and 0.5μm alumina powder, and this produced a similar result.

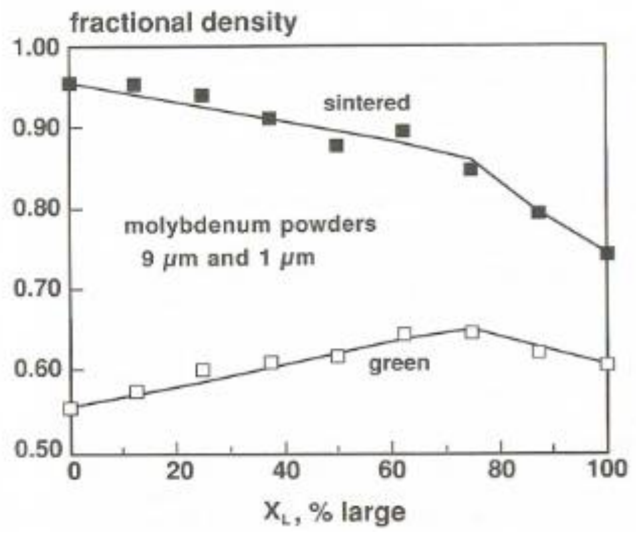

Figure 2-28 Composition effects on the fractional green density and fractional sintered density for a bimodal mixture of 9-µm and 1-µm molybdenum powder [110].

2.8 A review of porosity effects on the properties of sintered metal

2.8.1 Tensile stress (TS) to porosity relationship of sintered metals

Many theoretical models for the tensile behaviour of sintered metals have been derived by considering the micro-mechanisms of failure. Griffiths et al. [112] derived an analytical model of the TS of porous materials based on the ratio of load-bearing area and apparent cross-sectional area, as shown below:

$$\frac{\sigma_t}{\sigma_o} = \frac{A_b}{A_a} = 1 - \lambda P^{2/3} \qquad \textbf{(2-3)}$$

where σ_t is the TS of a porous material, σ_o is the TS of a bulk material, A_a is the apparent cross-sectional area, A_b is the load-bearing area, λ is an empirical constant and P is the level of porosity in vol.%. Griffith et al. suggested that the value of λ can be varied from 0.98 to 2.30, depending on the pore distribution and the interaction effect of the stress concentrations. With regard to the pore distribution, λ is equal to 0.98 for regular tetrahedrons and 1.077 for irregular tetrahedrons. However, when the porous material is subjected to a tensile stress, there are local stress concentrations induced around the pore cavities. To take into account the interaction effect of these stress concentrations, the λ value needs to increase further.

In 1981, Fleck and Smith [113] developed a brick model, as shown below:

$$\frac{\sigma_t}{\sigma_o} = (1 - P^{2/3})^2 \tag{2-4}$$

This model simplified the Griffiths's model by treating the powder particles as solid cubes and pores as cubic spaces and assumed that there is no effect of stress concentration on the pore geometry.

Haynes [114] also proposed a model by assuming no microstructural defects in the sintered metal, as shown below:

$$\frac{\sigma_t}{\sigma_o} = K(1 - P)^M \tag{2-5}$$

where K is a constant that depends on the test geometry and processing details and M is an exponential coefficient which depends on the level of porosity, and which normally varies from 3 to 6. The value of M will be affected by stress concentrations and premature fracture that is produced by crack propagation from pore to pore.

2.8.2 Ductility to porosity relationship for sintered metals

Haynes [115] proposed a simple equation that related the porosity level with the ductility of sintered metals, as presented below:

$$\delta_{rel} = \frac{\delta}{\delta_o} = \frac{V_B}{V_s} = (1 - P)^{\frac{3}{2}} (1 + C \cdot P)^{-\frac{1}{2}} \tag{2-6}$$

where V_B is the notional branch volume of a porous material, V_S is the notional branch volume of a bulk material, δ_o is the ductility of the bulk Ti, δ_{rel} is the relative ductility of the porous material and C is a constant which measures the sensitivity of the ductility to porosity content. This equation is based on the notional branch volume, which is defined as the deformed volume of material when under tension. The effect of the constant C on the relationship between ductility and porosity is shown in Figure 2-29. As the C value increases, the ductility of a material is more sensitive to the pores at a lower porosity content. In

Hayne's model, the *C* value is defined as a parameter which measures the sensitivity of the ductility to the porosity content in the material.

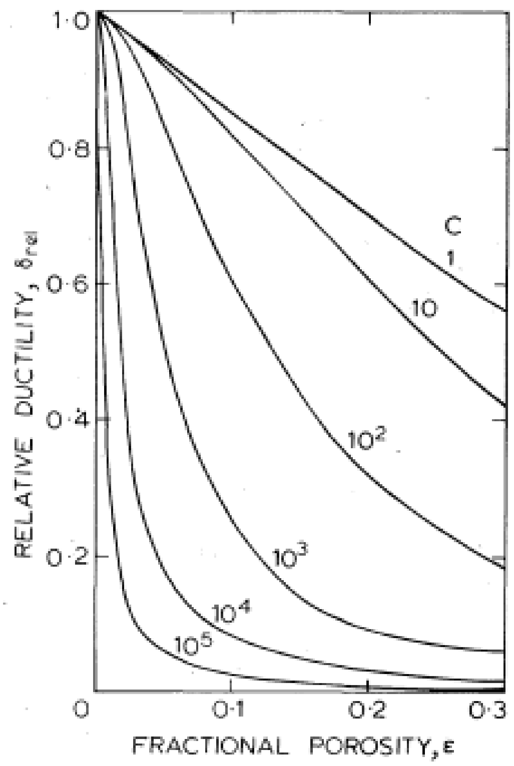

Figure 2-29 Effect of value of constant *C* on the form of the ductility/porosity content curve [115].

2.8.3 Open porosity to total porosity relationship for sintered metals

An increase in the total porosity level in a compact normally increases the level of open porosity. Depending on the techniques used, at a similar level of total porosity in a compact, the percentage of open porosity in a porous compact will vary. Data about the level of total porosity and open porosity collected from the literature is compared in Figure 2-30. As can be seen, the level of open porosity can be altered by the amount of space holder used, the size of the space holder, the powder particle size and the sintering conditions, etc. In Figure 2-30(a), the percentage of open porosity was governed by the different volume fraction of space holder in the compact, ranging from 30 vol.% to 70 vol.% [21]. In Figure 2-30(b), the particle size (from 65 μm to 374 μm), sintering temperatures (from 900°C to 1300°C) and sintering pressures (from 0 to 10 MPa) affected the level of porosity in the compact [18]. Erk, Dunand & Shull [15] employed a thermo-reversible gel casting method using Ti hydride (TiH_2, ≤ 45 μm) with polypropylene spaceholders (35 µm) to fabricate porous Ti products (Figure 2-30(c)). The volume of pores in their work depended on the volume fraction of spaceholders. Dabrowski et al. [8] used a conventional powder metallurgy method involving powder compaction and sintering with a space holder, to produce porous Ti compacts (Figure 2-30(d)). In this case, a range of compaction pressures (from 50 MPa to 100 MPa) were applied to alter the level of porosity.

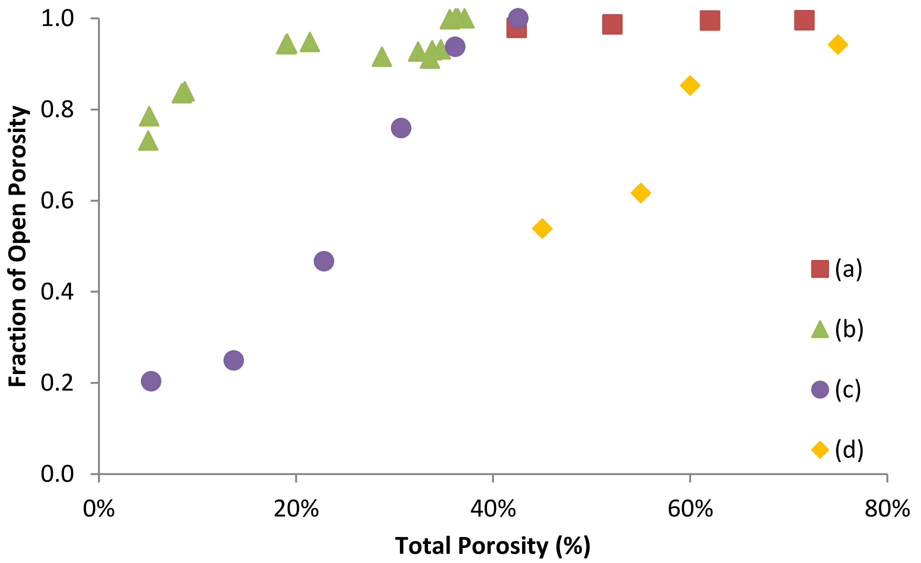

Figure 2-30 Variation of open porosity as a function of total porosity in porous Ti compacts produced by different processing techniques. Data points collected from the literature; (a) Metal injection moulding with space holder technique [21]; (b) powder compaction and sintering with different powder particle sizes and sintering conditions [18]; (c) gel casting using a space holder technique [15]; (d) powder compaction and sintering with a space holder [8].

2.8.4 Permeability to porosity relationship for sintered metals

Permeability is a measure of the volumetric flow rate for fluid flow through a unit area of a porous body under a given pressure gradient. Permeability is also a measure of flow resistance to flow through a porous body. A low value of resistance consumes less energy to push the fluid through the porous compact; however, high resistance to flow can also bring advantages, such as an increased effectiveness of heat transfer between a fluid and solid in heat-exchangers [116, 117]. One of the most commonly used equations to describe the relationship between porosity and permeability is the capillary tube model, developed from Kozeny – Carman equation [118, 119], Hagen-Poiseuille Law and Darcy's Law,

$$k = \frac{P \cdot \bar{d}^{2}}{16 f \tau} \tag{2-7}$$

where k is the permeability coefficient (m^2), $\bar{d}$ is the average diameter of the pore distribution, f is the shape factor of pore and τ is the tortuosity. This equation is assuming the porous media as a bundle of capillary tubes filled with a non-porous cementing material. This equation reveals that both the level of porosity and pore size have a positive effect on the permeability.

2.9 Discussion

In this discussion the reasons for undertaking this research, based on the findings of previous research work on porous Ti, are given. In other words, the previous research work will be discussed and a hypothesis justifying this new research will be stated.

Extensive research has been done on the development of porous Ti products using a variety of techniques, as described and explained above. Powder based processing techniques are dominant in making near-net-shape porous Ti products because they can be processed at low temperatures to prevent oxidation. Traditional methods to make near-net-shape porous Ti products have included a press and sintering route [12] and powder injection moulding (PIM) [21]. The press and sintering route is capable of creating products with a large proportion of open pores in an interconnected structure, using a space-holder technique. The pores are created by burning-out the space holder.. However, it is limited by the high cost of moulding dies, the limited complexity of the compact shape and a variable density gradient. PIM can be used to fabricate complex shapes, but the cost of moulds and the problem of a variable density gradient are important issues. In addition, a relatively large amount of binder is required for PIM, which raises concerns about binder residuals after the debinding stage, especially in the case of Ti. Recently, researchers have used ceramics casting techniques to process metals, including gel casting, freeze casting, tape casting and slip casting, as described in section 2.4. A common feature of these techniques is to start with a desirable viscosity of metal powder slurry. The complex geometries of products can be easily manufactured at low costs owing to the low cost of moulding materials, which are made from plastic materials [15], or plaster [16], etc. To some extent, this lowers the overall processing costs.

Only a limited amount of literature can be found on the slip casting of Ti. In 1970, Thellmann [24] was the first scientist to patent slip casting for use in metal processing. This person claimed that a slip containing 55 wt.% Ti powder particles, with a balance of 2 wt.% cellulose binder and 98 wt.% water was the optimum composition for slip casting. However, there were no detailed results about the carbon residuals and oxygen content that remained in the sintered Ti. In 2004, Ohkawa et al. [25] investigated a slip casting process to produce porous Ti for dental prosthetic appliances. In this paper, they only used one organic additive, sodium alginate, to produce a porous Ti casting. The results showed that rod-like TiC precipitates formed in the α-Ti, and that these derived from the decomposition of the organic additive. The densification process was hindered and a brittle sintered part was produced. Improvements could be made by changing the binder to improve the microstructure of sintered Ti. Some promising work by Neirinck et al. [17] used a Ti and Ti hydride slurry mixture to produce porous Ti compacts by slip casting. Ti hydride raises safety issues due to the release of hydrogen gas during sintering. No further detailed work describing the use of slip casting for processing Ti powder could be found in the literature. And yet the slip casting process is a promising technique for producing porous Ti products which warrants further research.

The development of stable metal powder slurries is the most significant challenge. This is because metal powders are generally larger in size and higher in density than the ceramic powders used in slip casting. A stable and deflocculated suspension gives a homogenous microstructure once it is cast into a compact with sufficient green strength for handling. A dispersant acts as a deflocculating agent. A flocculated suspension produces a compact with an inhomogeneous microstructure with a variation in packing density. Therefore, during sintering, the microstructure shrinks unevenly so that cracks are generated. A binder and plasticiser give strength to the compact once it is in a dry or semi-dry state. The amount of these two organics needs to be controlled as carbon residuals and oxygen pickup are always a problem in the processing of Ti. Moreover, a good organic additive system has to be burnt out during the debinding stage with minimum residual contamination. A small amount of backbone binder is expected to remain in the partially debound compact to support the structure. A number of researchers have reported slurry formulations for slip casting different materials, as shown in Table 2-1. Therefore, a careful choice of organic additives is necessary. A novel slurry formulation for use in Ti slip casting is required. This should be able to satisfactorily produce Ti compacts with low contaminant levels and good mechanical strength.

The porosity level in a sintered powder metallurgy compact is controlled by several factors, such as sintering conditions, green density, particle size of the initial powders, etc, as presented in section 2.6.4 and 2.7. Also it can be seen that the porosity level has a profound impact on the mechanical properties, open porosity, and permeability of sintered compacts (section 2.8). However, there is a lack of experimental data in the literature showing the effect of a range of porosity levels on the properties of sintered Ti prepared by slip casting. Therefore it is of interest to investigate the effect of porosity on these properties for slip cast Ti and to compare theoretical models and the results of experimental work from previous researchers with the experimental results in this new research. This will enhance our understanding of the slip casting process for Ti.

Overall, in this research, the hypothesis to be investigated is that appropriate choices of organic additives, sintering conditions and powder size fractions in the slip casting process can achieve a variety of porosities in sintered Ti products, while maintaining an acceptable level of contaminants and adequate mechanical strength.

3. Chapter 3 -- Experimental Procedure

This chapter describes the experimental work, including the overall procedures of slip casting, testing methodologies and materials' characterisation.

3.1 Raw materials

As starting materials, commercially available Ti powders, with two different average particle sizes (purity: 99.95%; Xi'an Baode Powder Metallurgy Co. Ltd, China) produced by the hydride/dehydride (HDH) process, were used in this study (Figure 3-1).

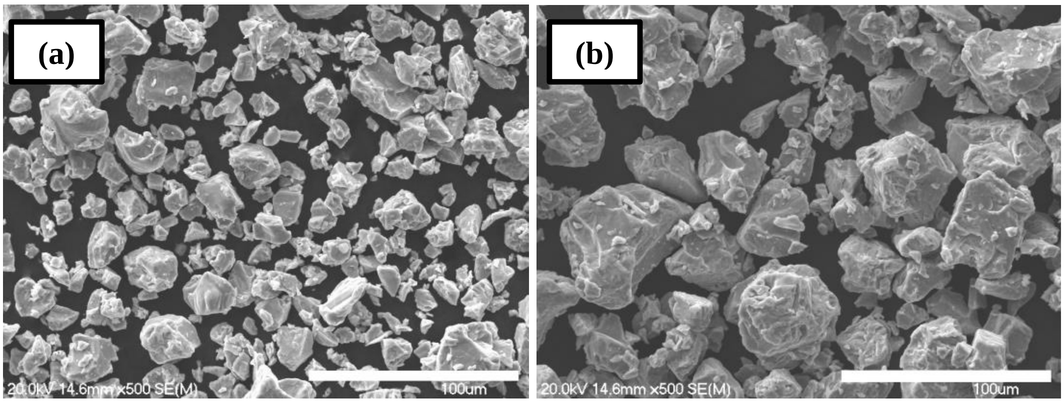

Figure 3-1 SEM image of HDH Ti powder; (a) an average particles size of 14 μm; (b) an average particles size of 56 μm.

Three different classes of organic dispersants were selected. Dispex N-40 and Synthecol SD375 were supplied by Pyrotek Ltd, NZ, whereas Synthecol SD375 is not yet commercially available. Dolapix CE64, made from carboxylic acid, is commercially available and supplied by Zschimmer & Schwartz GmbH Co., Germany. A detailed list, along with the chemical basis, density, and ionicity is presented in Table 3-1. Polyvinyl alcohol (PVA, mw.13,000; Sigma-Aldrich, US) and polyethylene glycol 400 (PEG400; Fluka Chemie GmbH, Germany) were used as the binder and plasticiser, respectively. The choice of these two chemicals was based on their low decomposition temperature so that the reaction with Ti powders at high temperature is minimised.

Table 3-1 List of dispersants along with their properties.

Organic Dispersants	Chemical Basis	Ionicity	Density (20°C)
Dispex N-40	Sodium salt of an acrylic copolymer	A[1]	1.3 g•cm^{-3}
Synthecol SD375	Polycarboxylate ether	A	----
Dolapix CE64	Carboxylic acid	A	1.2 g•cm^{-3}

[1] A – Anionic

3.2 Procedures for making a slip

An overview of the slip casting process is summarised in Figure 3-2, which can be categorised into three major steps, namely slurry formulation, de-binding and sintering. A detailed description will be presented below.

Figure 3-2 A process flow chart for slip casting.

A high density polyethylene (HDPE) plastic jar was used to ball mix all the components, including water. The speed of the roller used for ball mixing was kept at a constant 120 rpm until degassing. The sequence for making a green compact by slip casting is described below.

(1) Distilled water was mixed with the dispersant for 2 hours in a jar.
(2) Ti powder was added to the jar followed by further mixing for 24 hours.
(3) The binder and plasticiser were added and mixed for another 16 hours.

(4) The slurry was degassed for 6 hours using a low rotation speed of less than 10rpm.
(5) The well-mixed slurry was poured into a plaster mould with a plaster to water ratio of 1.53, to form the green compacts. The plaster mould used for casting a rectangular compact had a cavity 40mm long, 20mm high and 10mm wide and the mould for casting tubular compacts had a cavity 40mm in diameter and 70mm high, with an inner cylindrical mandrel (Ø20mm).

(6) The green casts were dried in the mould overnight, and then transferred to an oven at 40°C for one day prior to debinding.

(7) The debinding process was carried out in a horizontal tube furnace with a controlled argon flow rate of 150 ml/min. The debinding temperature will be determined from the results of thermal analysis on the organic additives.

(8) The debound compacts were then placed on a molybdenum plate and sintered under high vacuum (3×10^{-3} Pa). The detailed sintering procedures are presented in section 3.5.

3.3 Slurry formulation

The slurry formulation was investigated with respect to solids content level, dispersant, binder and plasticiser concentrations.

To determine the optimum level of dispersant, the following techniques were used.

(1) Sedimentation technique. Visual observation of the sediment volume and sedimentation rate enabled evaluation of the stability of a slip system. For the sedimentation test, a 60 wt.% Ti aqueous slip was prepared with different concentrations of dispersants (0, 0.3, 0.6, 0.9 and 1.2 dry weight percentage [dw.%]). The slips were transferred to 10 mL measuring cylinders. The sedimentation rate was recorded every 5 minutes for the first 20 minutes by measuring the levels of sediment and noting the sedimentation height after 24 hours.

(2) PCD-potential measurement. The potential characteristics [mV] were measured with a particle charge detector (PCD-03) (Model: Mutek, Germany). The test solution was the same as that used in the sedimentation test. Different concentrations of dispersant were investigated and the streaming potential was used as an indication of the surface charge on particles. A sample was poured into a cylindrical test cell inside which a displacement piston oscillated with a constant frequency. As the piston oscillated, the sample liquid was forced to flow along the wall of the test cell, generating a streaming potential that was measured by two gold electrodes [120]. Due to the fluctuation in the streaming potential, a mean value and the range were taken from the readings.

(3) Viscosity measurement. A viscometer (Brookfield Digital Viscometer, LVTDV-II) was used to measure the viscosity of each slurry, which consisted of 75 wt.% Ti, the balance being water, with 1 dw.% binder (PVA), 1 dw.% plasticiser (PEG400), and different concentrations of dispersants (0, 0.3, 0.6, 0.9 and 1.2 dw.%). The viscosity was measured as a function of rotational speed [rpm] for different amounts of dispersant and changes in pH of solvent.

To obtain the optimum solids content level, the viscosities of slurries prepared at different solids loadings (15, 21, 29, 40, 43, 47 vol.%) with an addition of 0.3 dw.% of dispersant, were measured. To determine the optimum amount of binder and plasticiser, the viscosity of slips, green strength and green density of green compacts were investigated. The green strength of compacts was evaluated from a three point bending test carried out using an Instron tensile testing machine with a cross-head speed of 0.05 mm/min. Before testing, each slip cast rectangular part ($40 \times 20 \times 10mm^3$) was sliced into rectangular bars with a 6mm×6mm square cross section and a 24mm span. The green densities of compacts were averaged using a mass/volume equation from three green rectangular compacts ($40 \times 20 \times 10mm^3$) for each binder concentration (0.6 – 1.2 dw.%). A summary of all the testing parameters is listed in Table 3-2.

Table 3-2 A summary of testing parameters used in a slurry formulation.

Investigated Parameters	Variables	Measurements
Dispersant contents	0, 0.3, 0.6, 1.2 dw.%	• Sedimentation • PCD-potential • Viscosity
Solids content level	15, 21, 29, 40, 43 & 47 vol.% Equivalent to 45, 55, 65, 75, 77 & 80 wt.%	• Viscosity
Binder to plasticiser ratios	1:1 (0.5 dw.% : 0.5 dw.%) & 1:2 (0.5 dw.% : 1.0 dw.%)	• Three point bending test
Binder contents	0.6, 0.8, 1.0 & 1.2 dw.%	• Viscosity • Green density

3.4 Debinding

Thermogravimetrical (TG) analyses (SDT 2960 – Simultaneous DTA – TGA) were performed on the DP64, PVA and PEG400 components to determine their thermal properties in order to optimise the debinding process. Two different atmospheres, air and argon, were also employed in the study. The debinding work was then carried out in a horizontal tube furnace with a heating rate of 1°C/min and a controlled argon flow rate of 150ml/min, as shown in Figure 3-3. The mass loss was recorded for each condition.

Figure 3-3 Debinding furnace used in this work.

3.5 Sintering

The sintering work was undertaken in a high vacuum furnace (3×10^{-3} Pa), as shown in Figure 3-4. The first aim of the sintering work was to control the sintering parameters and achieve a desirable porosity level. The second aim was to determine the effect of porosity on gas permeability, pore size distribution, pore shape, the degree of interconnected pores and the mechanical behaviour of slip cast Ti. The porosity range was controlled using different sintering conditions such as sintering temperature, sintering time, heating rate and cooling rate. Taguchi’s method was applied in this study. The traditional approach to experimental work is to vary one factor at a time, keeping other factors constant. For instance, an investigation with 4 factors, each with 3 levels needs $3^4 = 81$ experiments to be carried out. However, Taguchi’s method only requires 9 experiments plus 1 confirmation test. It is more economical, as fewer experiments are needed than would be required for a one-variable-at-a-time technique and conclusions can be associated with a statistical level of confidence [121]. Taguchi's method has been used in sintering studies by some researchers [63, 121]. The sintering scheme is shown in Table 3-3 and Table 3-4.

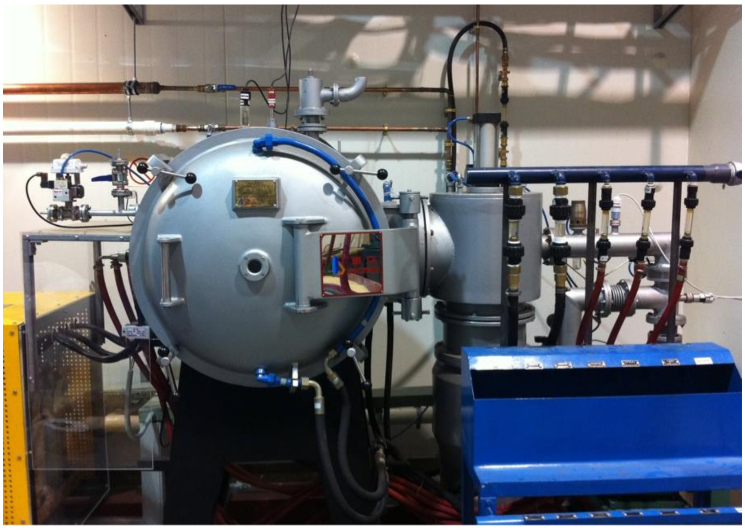

Figure 3-4 High vacuum sintering furnace.

Table 3-3 Factors and levels for the sintering experiments.

	Factors	Level 1	Level 2	Level 3
A	Sintering Time (h)	0.5	1	2
B	Cooling Rate (^{o}C/min)	5	10	Furnace Cooling
C	Heating Rate (^{o}C/min)	5	7	10
D	Temperature (^{o}C)	1000	1100	1200

Table 3-4 Experimental layout and factor distributions of an L_9 orthogonal array.

Run No.	A	B	C	D
T1	1	1	1	1
T2	1	2	2	2
T3	1	3	3	3
T4	2	1	2	3
T5	2	2	3	1
T6	2	3	1	2
T7	3	1	3	2
T8	3	2	1	3
T9	3	3	2	1

Typical heating profiles for the sintering furnace with different cooling rates are plotted in Figure 3-5. The cooling rates (5°C/min & 10°C/min) were controlled until the temperature was below 650°C, after which furnace cooling was used down to room temperature. During furnace cooling, the temperature in the sintering furnace followed an exponential decay. However, when the sintering process uses furnace cooling, the temperature rapidly decreases from the sintering region to below 650°C in about 15 minutes. On the other hand, a slow cooling rate could prolong the sintering process. Therefore, cooling rate could be a potential variable which affects the porosity.

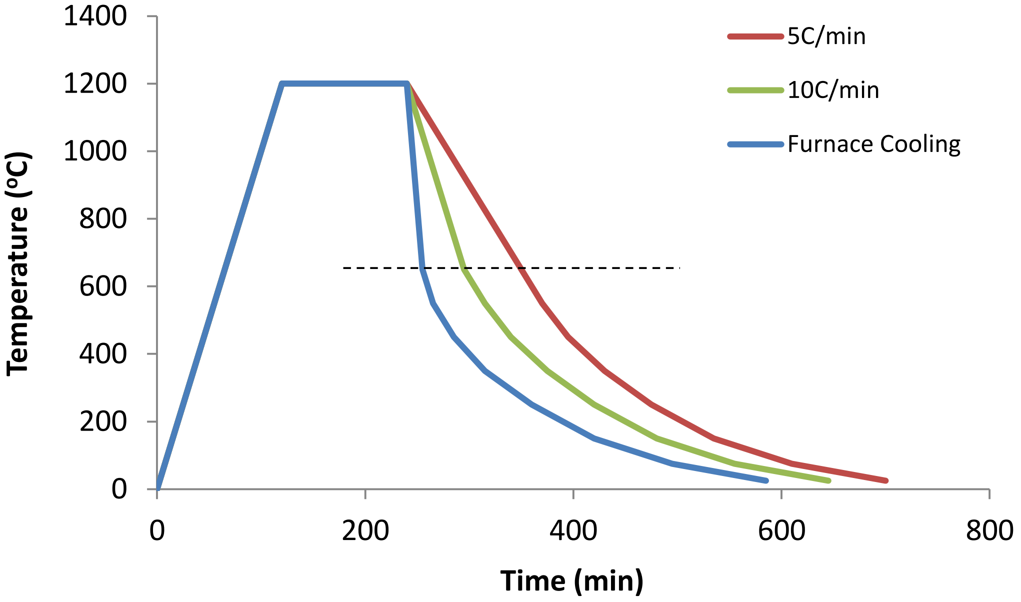

Figure 3-5 Typical heating profiles with different cooling rates, 5°C/min, 10°C/min and furnace cooling.

3.6 Experimental design on binary particle size effect

The effect of particle size distribution (PSD) on the slip casting of Ti was investigated by blending fine Ti powder and coarse Ti powder in five different volume proportions (20:80, 40:60, 60:40, 80:20 & 100:0). The optimised slurry formulation, obtained from experiments as described in section 3.3, were used to make these five compositions of slurry; in other words, the amount of Ti powder, solvent, dispersant, plasticiser and binder added to the slurry were the same. Two dimensions of green rectangular compacts (40 × 20 × 10mm^3 & 100 × 20 × 10mm^3) were made for analysis. By following the procedures as described in section 3.2, three sintering temperatures were investigated, namely 1000°C, 1100°C and 1200°C. The experimental design is summarized in Table 3-5.

Table 3-5 Experimental design for study on the PSD effect of slip casting Ti.

Run No.	Volume percentage of fine powder particles (vol.%)	Sintering temperature (°C)
1.1	20	1000
2.1	40	
3.1	60	
4.1	80	
5.1	100	
1.2	20	1100
2.2	40	
3.2	60	
4.2	80	
5.2	100	
1.3	20	1200
2.3	40	
3.3	60	
4.3	80	
5.3	100	

3.7 Testing Methods & Materials Characterisation

3.7.1 Porosity and open porosity

The total porosity and the open porosity in sintered Ti compacts were measured by the Archimedes' method. The samples were dried at 80°C in an oven until a constant weight was obtained. Then, the sintered compacts were vacuum impregnated overnight with distilled water to measure the saturated weight. The saturated sample was placed on a plastic support in water and the suspended weight was noted. The theoretical density of bulk Ti is 4.5 g/cm^3. The density of water (ρ_{water}) depends on the temperature. The following equations were used to calculate the total porosity and the open porosity level in the sintered Ti compacts.

$$Density = \frac{Dry\ Weight}{(Saturated\ Weight - Suspended\ Weight) \times 4.5} \times \rho_{water} \times 100\% \tag{3-1}$$

$$Porosity = 1 - Density \tag{3-2}$$

$$Open\ Porosity = \frac{Saturated\ Weight - Dry\ Weight}{Saturated\ Weight - Suspended\ Weight} \times \rho_{water} \times 100\% \tag{3-3}$$

$$\rho_{water} = 1.0017 - 0.2315 \times Temperature\ at\ measurement \tag{3-4}$$

3.7.2 Permeability and pore throat size analysis

The permeability and pore throat size analysis was carried out using a pore size distribution analyser (GaoQ Functional Materials Ltd, China). The samples were wire electric discharge machined to a 2 mm thickness and 20mm diameter circular shape and prior to the test, both sides of the samples were ground and fine polished to remove the blockages from the pores after machining. An ultrasonic bath was then used to clean up the samples. The testing methods were based on ASTM F316-03 [122]. The samples were fixed using a sample holder sealed by silicon washers, which was connected to a gas flow tube. Nitrogen gas was flushed through the samples at different flow rates and the corresponding pressure differences were recorded by a pressure sensor. The permeability coefficient was determined using Darcy's law [123]. In the sintered porous material, each pore may have many diameters. Herein, for each pore, the pore size in the material was measured based on the most constricted pore throat diameter in the pore. Information about pore throat diameters is useful for estimating the size of the debris that might pass through a filter [123].

Figure 3-6 Image of the pore size distribution analyser.

3.7.3 Interconnected pore characterisation

A characterisation technique for the identification of interconnected pores was developed using ammonium meta-tungstate (AMT, $(NH_4)[H_2W_{12}O_{40}]\cdot nH_2O$), which is a 99.99% water soluble chemical. AMT was dissolved in distilled water with a mass ratio of 2:1. The samples were then immersed in the AMT solution and kept under vacuum conditions until no bubbles came out. The samples were dried in an oven at 40^{o}C and then put into a muffle furnace, heated to 550^{o}C and held at this temperature for 3 hours. Mooney et al. [124] indicated that AMT is completely transformed to tungsten trioxide (WO_3) at 450^{o}C. Thus, tungsten trioxide would infill the interconnected pores in the porous Ti compacts. Prior to observation, the samples were wire cut machined and the cutting surface ground. WO_3 and Ti have very different atomic number, therefore, the interconnected pores can be observed by backscattered electrons using a Hitachi S4000 scanning electron microscope (SEM).

3.7.4 Particle size distribution analysis

The particle size distributions of the powder were determined using a Malvern MasterSizer machine with Low Angle Laser Light Scattering (LALLS). The powder was dispersed ultrasonically in water.

To analyse the homogeneity of the powder particle size distribution in a mixture of coarse and fine powder particles, samples from three different locations (top, middle & bottom) were taken from a long rectangular compact (100 × 20 × 10mm^3), as illustrated in Figure 3-7.

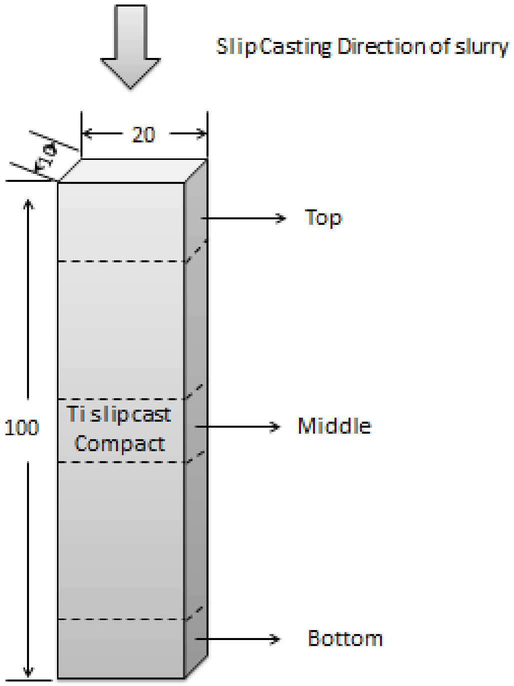

Figure 3-7 An illustration of sample locations taken from a green compact.

3.7.5 Green packing density

The green packing density of a slip cast compact was measured using the mass/volume equation. However, in the experiment, the slip was made using 100 vol.% coarse powder particle sediments in less than 20 seconds and were difficult to re-disperse. The time was too short to allow transference of the slip into the plaster mould. In this case, the packing density of the 100 vol.% coarse powder was then measured by pouring the slip into a 10 mL cylinder and drying in an oven at 60°C until no weight loss was observed. And the mass/volume equation was used to obtain the packing density. The relative packing density was obtained by dividing the measured density by the bulk density of Ti (4.5 g/cm^3).

3.7.6 Three point bending test

The green strength of compacts was evaluated from a three point bending test carried out using an Instron tensile testing machine with a cross-head speed of 0.05 mm/min. Before testing, each slip cast rectangular part (40mm × 20mm × 10mm) was sliced into rectangular bars with a 6mm × 6mm square cross section and a 24mm span.

3.7.7 Tensile testing

Tensile testing of porous Ti compacts was carried out at room temperature using an Instron 4204 tensile testing machine at a strain rate of 1×10^{-4} s^{-1}. Dumbell shaped specimens for tensile testing, with a rectangular gauge cross section of 2×2 mm^2 and a gauge length of 10 mm, were wire electric discharge machined from sintered Ti compacts. The tensile specimens were ground and polished using 600, 1000 and 2000 grit SiC polishing papers.

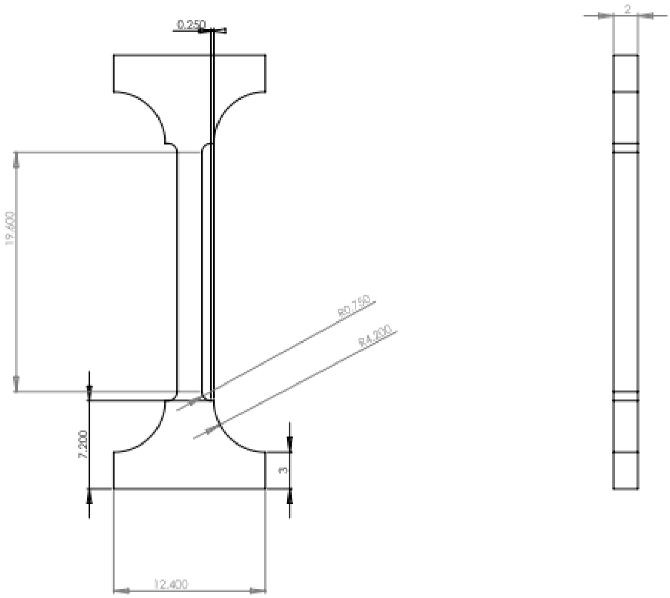

Figure 3-8 Drawing of the tensile test sample.

3.7.8 Optical microscopy

Optical microscope (Olympus BX60) was used to observe the polished cross sectional microstructures in the sintered samples. The samples were also chemical etched by Kroll’s reagent.

3.7.9 Scanning electron microscopy

The fracture surfaces of tensile specimens were examined using a Hitachi S4000 scanning electron microscope (SEM). The longitudinal planes of fractured specimens, which had been prepared by grinding and polishing, were also examined. All samples were coated with a thin film of Pt/Pd using an ion sputterer (E1030, Hitachi).

Backscattered electron imaging was performed on the above system, equipped with a Robinson Detector module.

Energy dispersive x-ray analysis of the samples was performed on the above system equipped with a Kevex Quantum Window x-ray detector, passed through a signal processor (Model 500, IXRF Sustems Inc.) and analysed using the EDS Thermo Noran System SIX.

3.7.10 X-ray Diffraction

X-ray diffraction (XRD) analysis was carried out using a Philips X-pert system with CuKα radiation source. An incidence beam has a scan rate of 2°/min. The scan angle of 2-theta was ranged from 20° to 80°. X'Pert HighScore Plus software was used to analyse the result.

3.7.11 Oxygen and carbon analysis

Oxygen and carbon analysis of the Ti powder and sintered compacts was done at the Institute of Metal Research, Chinese Academy of Sciences, China. For oxygen analysis of a sintered compact, a specimen was required to have a diameter of 3 mm and a length of 40 mm. For carbon analysis on a sintered compact, the specimen was required to consist of at least 5 grams of chips, which were machined using a lathe.

3.7.12 Pore diameter & Pore shape

The pore diameter and the pore shape was measured using image analysis software (Image-Pro Plus) on micrographs obtained using optical microscopy. The pore diameter was measured at two degree intervals and passing through object's centroid, as shown in Figure 3-9.

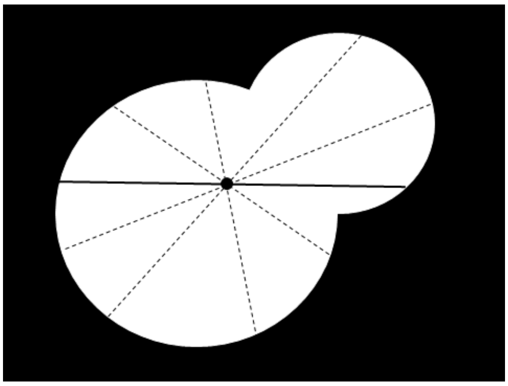

Figure 3-9 An illustrate of measurement on mean pore diameter.

A pore shape factor, F, was used to quantitatively characterise the pore shape using Equation (3-4) [125], where A is the measured area of a pore and P is the measured perimeter of a pore. A pore shape factor of one denotes a round pore. As the value approaches zero, an irregular pore is indicated.

$$F = \frac{4\pi A}{P^2} \tag{3-4}$$

4. Chapter 4 – The development of slip casting process to fabricate porous Ti products

4.1 Introduction

The main objective of this work was to develop a low-cost manufacturing method to fabricate Ti products with a controlled level of porosity using a slip casting approach. An important aim was the optimisation of the Ti slurry formulation to minimise the content of organic additives. A lower organic additive content reduces the probability of carbon contamination in the sintered Ti products. This chapter covers the optimisation of dispersant, solids content level, binder and plasticiser. Thermogravimetric analyses (TGA) was also performed on the organic additives to define the optimum debinding process. Last but not least, a sintering process was undertaken and the impurity content of sintered compacts was examined to verify the feasibility of the optimised slurry formulation. Detailed experimental procedures can be referred to Chapter 3.

4.2 Results and Discussion

4.2.1 Dispersant

4.2.1.1 Streaming potential study

Figure 4-1 shows the variation of streaming potential for different dosages of three dispersants (Syntehcol SD375, Dolpix CE64 & Dispex N-40). All of these dispersants are anionic polyelectrolytes, which give a negative charge to the particles. Both Dolapix CE64 and Dispex N-40 showed a maximum negative potential at 0.3 dw.% and then a decrease (less negative potential) in streaming potential as the dosage increased. It is especially noted that as the concentration of Dispex N-40 increased to 0.9 dw.% and 1.2 dw.%, there was significant fluctuation in the streaming potential, as indicated by the error bars. This was because at higher dosages, due to the high ionic strength, there was compression of the diffuse layer, leading to a reduction in thickness of the double layer on the particles. As a result, the surface charge decreased, which in turn caused the stability of the system to decrease. On the other hand, Synthecol SD375 presents a different pattern of streaming potential due to the steric effect induced on particles' surfaces. Thus, the streaming potential increased negatively as the dispersant concentrations increased which causes more dispersant to be adsorbed onto the particles' surfaces.

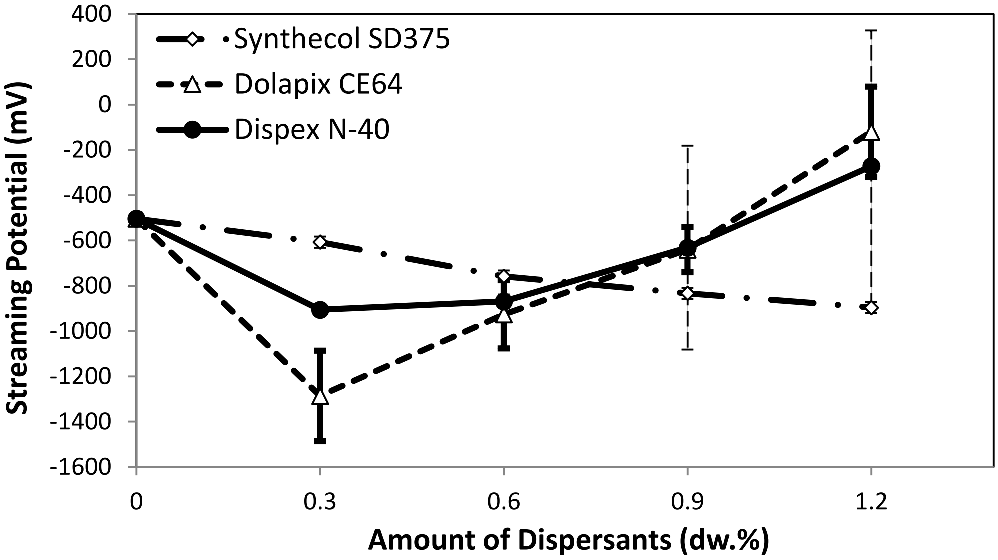

Figure 4-1 Effect of dispersant concentration on the streaming potential of a 60 wt.% Ti slurry.

4.2.1.2 Sedimentation rate and sedimentation height

In a deflocculated slip, there is a slow sedimentation rate and a cloudy region is formed, then after a certain period of time even settling occurs [126]. Figure 4-2 displays the sedimentation behaviour of Ti slips, mixed with different amounts of three dispersants, as a function of time. The sedimentation tests indicate that both Dolapix CE64 and Synthecol SD375 have a good dispersing effect, while Dispex N-40 has the least deflocculating effect on the slip. At 0.6 dw.% and 0.9 dw.% of Synthecol SD375 and 0.3 dw.% of Dolapix CE64, slow sedimentation rates were observed. Thus, Synthecol SD375 and Dolapix CE64 were selected for a measurement of rheological properties.

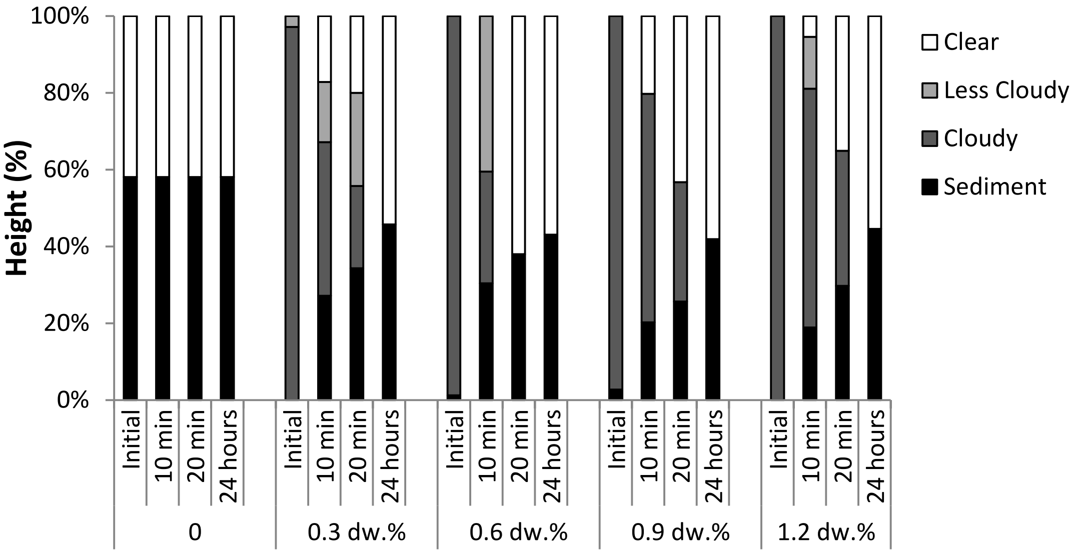

(a) -- Time (min) - Dispex N-40

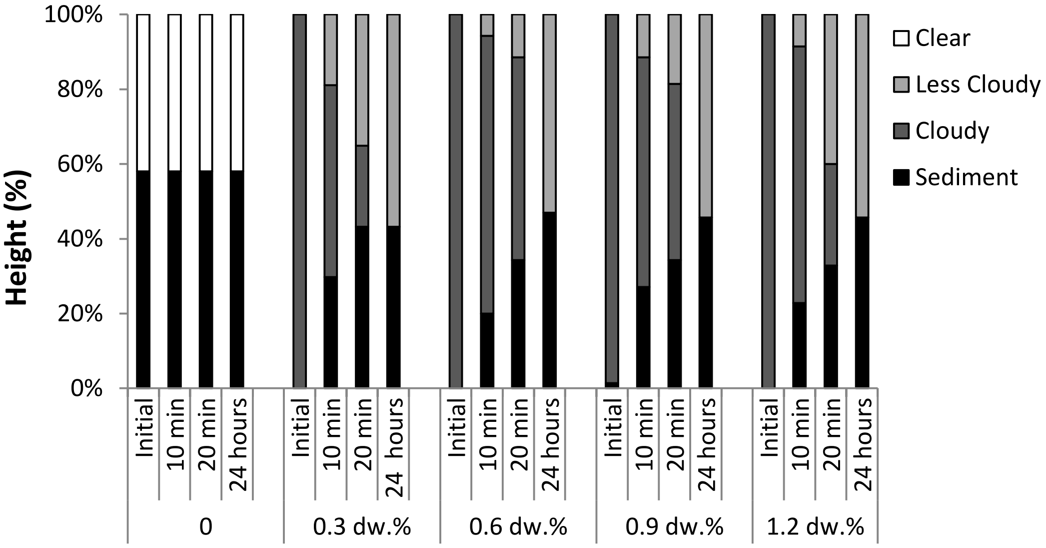

(b) -- Time (min) - Synthecol SD375

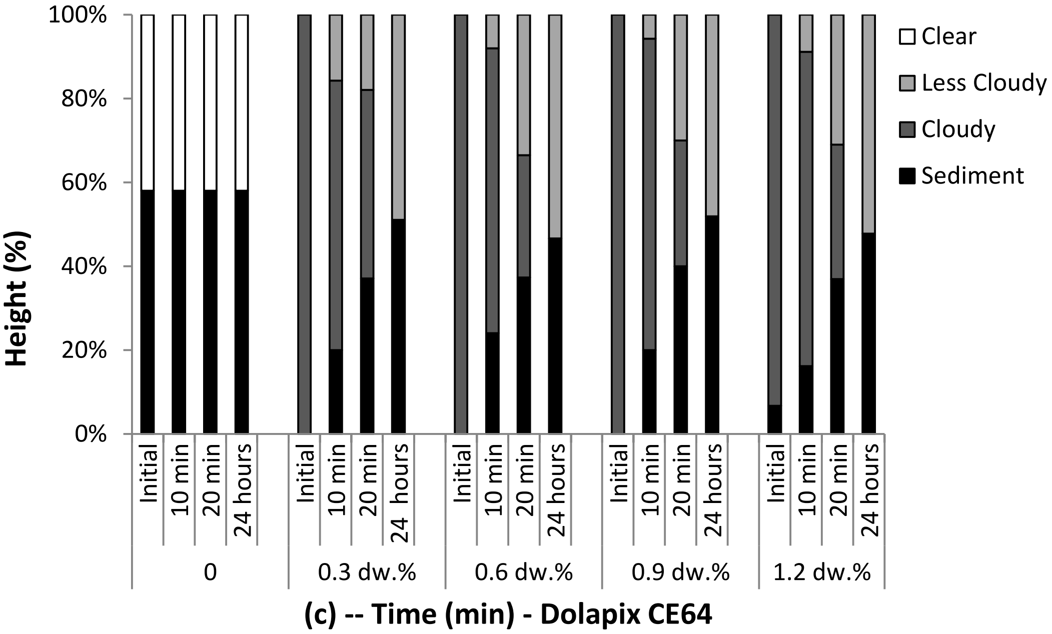

Figure 4-2 Sedimentation study for a 60wt.% Ti slip at different concentrations 0, 0.3, 0.6, 0.9 & 1.2 wt.%; (a) Dispex N-40; (b) Synthecol SD375; (c) Dolapix CE64.

4.2.1.3 Viscosity measurement

Figure 4-3 (a) and Figure 4-3(b) present the viscosity of each slip as a function of the concentration of dispersant for Synthecol SD375 and Dolapix CE64, respectively. For Synthecol SD375 (Figure 4-3(a)), concentrations of 0.3 dw.%, 0.6 dw.% and 0.9 dw.% displayed minimum viscosities at 60 rpm, 30 rpm and 12 rpm, respectively. At 0.9 dw.%, the slip displayed a near-Newtonian flow, while other slips exhibited a pseudoplastic flow. Figure 4-3(b) shows that Dolapix CE64 at the concentration of 0.3 dw.% had the lowest viscosity for all three rotational speeds. From that point on, as the amount of Dolapix CE64 increased, the viscosity of the slip increased. Therefore, as the concentration of the dispersant increased, the resistance to flow and the viscosity of the Ti slip dropped down initially. By increasing the concentration further, the viscosity increased again due to the excessive formation of micelles in the solvent [127]. The optimum level of Dolapix CE64 at 0.3 dw.% is well corroborated with the results from the streaming potential measurement and the sedimentation study.

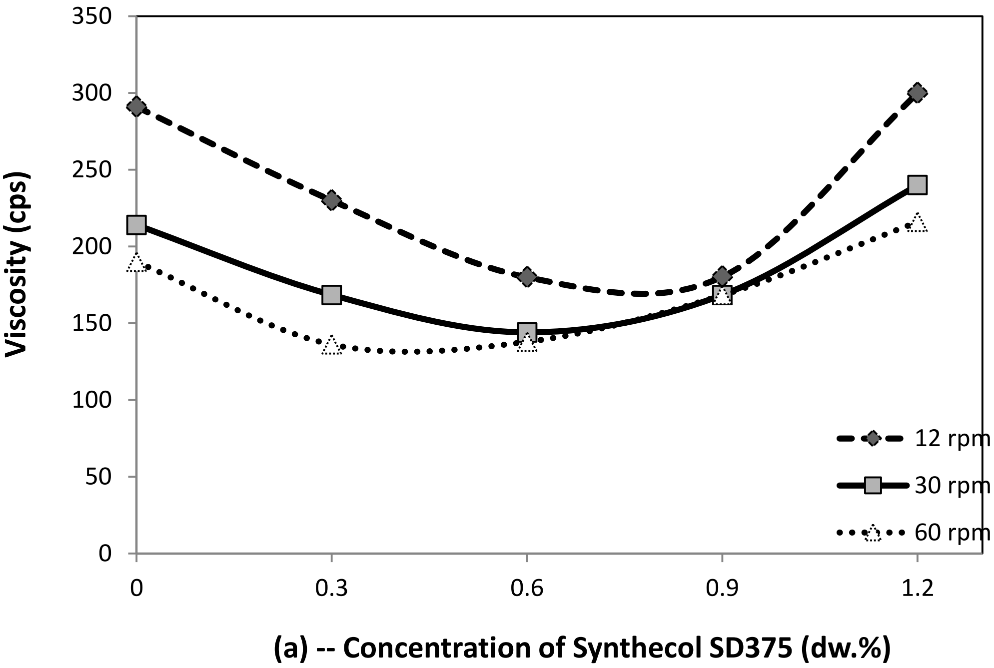

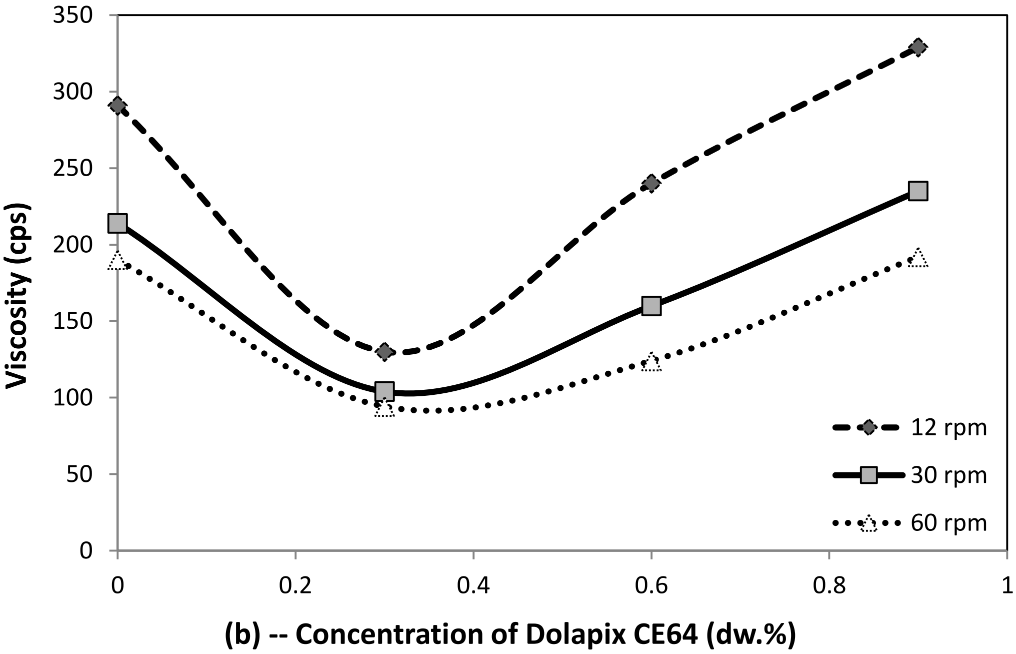

Figure 4-3 Apparent viscosity of a 75 wt.% Ti slip, with 1 dw.% binder (PVA) and 1 dw.% plasticiser (PEG400), as a function of the amount of dispersant at different rotational speed. (a) Synthecol SD375; (b) Dolapix CE64.

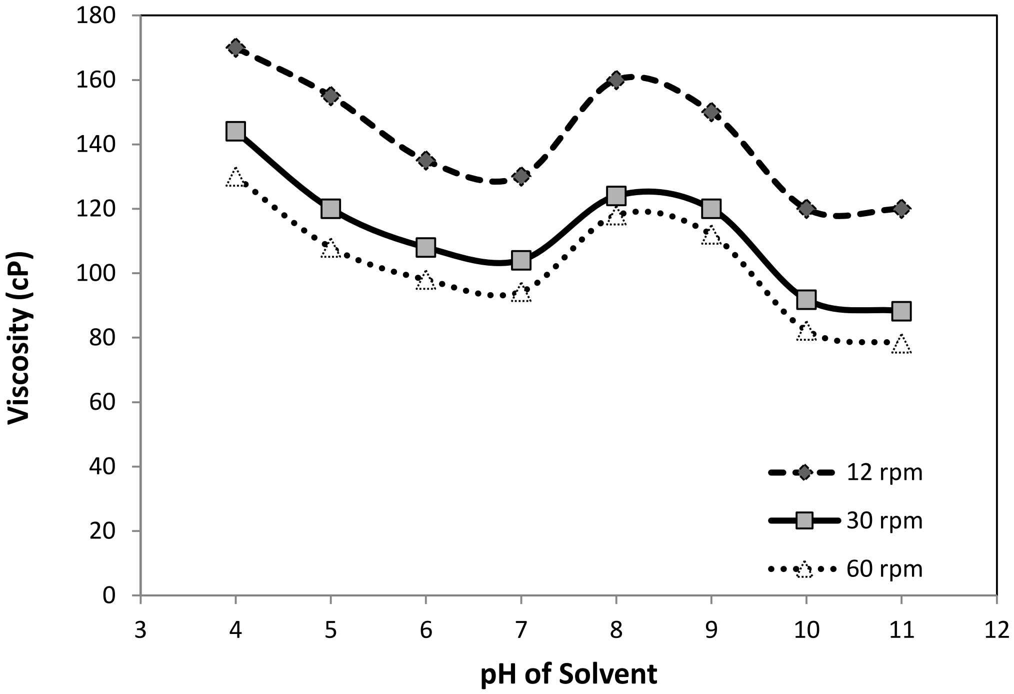

Figure 4-4 Apparent viscosity of a 75 wt.% Ti slip, with 0.3 dw.% dispersant (Dolapix CE64), 1 dw.% binder (PVA) and 1 dw.% plasticiser (PEG400) as a function of pH of solvent.

Figure 4-4 shows the effect of solvent pH on the viscosity of the Ti slip. At pH 7, a minimum point of viscosity was observed, followed by a slight increase and then a further drop at pH 10 and pH 11. This is in good agreement with previous research which concluded that the anionic polyelectrolyte Dolapix CE64 is found to have the most effective dispersing effect over the range pH 7 – 11 [84, 128]. In this case, pH 7 was chosen as the optimum environment for Dolapix CE64, which only involves pure distilled water, while pH10 and pH11 introduced foreign substrates into the slip. This may raise concerns during the debinding stage and also produce side effects on the mechanical properties of the final products.

Therefore, in a short conclusion, the dispersant with optimum performance is Dolapix CE64 at 0.3 dw.% and with a pH of 7.

4.2.2 Effect of solids content on slurry viscosity

The viscous behaviour of Ti slurries with a range of Ti powder content from 15 vol.% to 47 vol.% (corresponding to 45 to 80 wt.%) was first investigated using a fixed amount of organic additives (Figure 4-5). Krieger [77] developed a Krieger-

Dougherty (K-D) model, which described theoretically the rheological behaviour of slurry as the volume fraction of solids loading changes, as presented in Equation (2-1). In this work, the HDH Ti particles had irregular shapes and therefore the values of ϕ_m and $[\eta]$ needed to be modified. The solids loading in weight fraction has been converted to volume fraction for calculation and the relative viscosity was plotted against volume fraction. The theoretical model was fitted to the experimental data, as shown in Figure 4-5, by changing ϕ_m to 0.53 and $[\eta]$ is 5.2. Hunter et al. [129] proposed that if it is assumed there is no fluid slip at the surface of spherical particles, $[\eta]$ is 2.5, whereas with increasing aspect ratio of anisometric particles the value of $[\eta]$ increases. The maximum packing fraction (ϕ_m) of 0.53, used here, is lower than the expected packing fraction of 0.62 for close packed spheres of equal size. This can be explained by the poorer space filling when particles are asymmetrical. The experimental data showed that the relative viscosity increased gradually from 1.14 at 15 vol.% (45 wt.%) powder loading to 38 at 43 vol.% (77 wt.%) powder loading, after which there was a sharp increase to 212 at 47 vol.% (80 wt.%) powder loading. This implies that the solids loading at 43 vol.% (77 wt.%) is a critical point for this type of Ti slurry system with powders of irregular morphology. Ferreira and Diz [75] investigated the effect of solids loading and particle morpholgy on the rheological properties of a slip casting slurry and its green microstructure. The lower viscosity, and hence increased fluidity for powder loadings less than 43 vol.% (77 wt.%), promotes particle segregation resulting in a non-homogenous packing structure. This is due to a rearrangement of small particles, to occupy the lowest-free-energy positions, at the interface between the suspension and cake. On the other hand, the increased viscosity for a higher powder loading of 47 vol.% (80 wt.%), could hinder powder rearrangement and particle segregation. Since the slip requires a certain degree of fluidity to be discharged into the mould, a solids content level of 43 vol.% (77 wt.%) is an optimum level for Ti slip casting of this mixture, using organic additives.

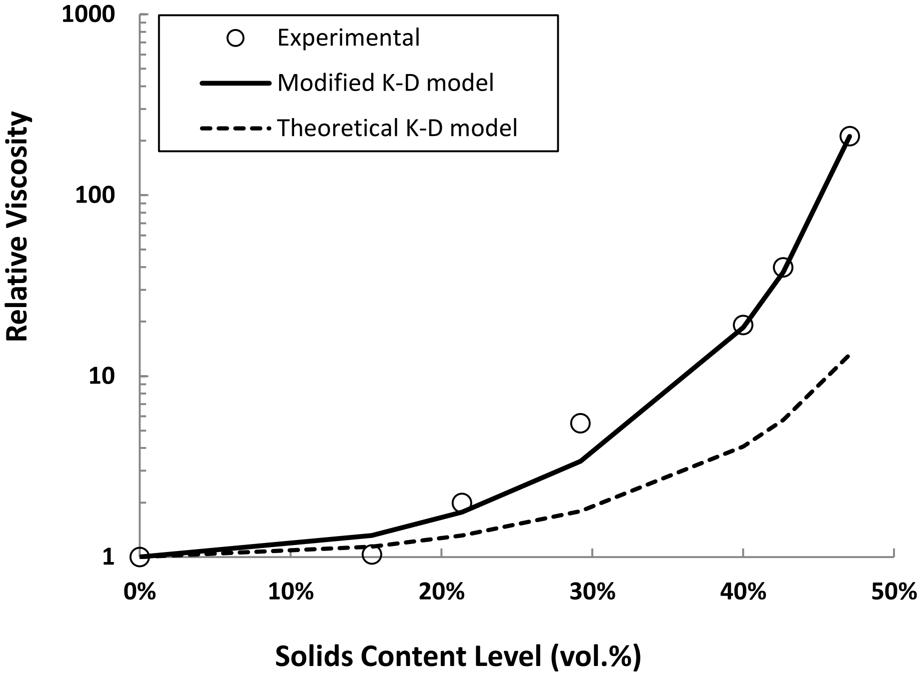

Figure 4-5 A viscosity study of a Ti slurry, with different powder loading volume fractions.

4.2.3 Effect of binder and plasticiser concentration

The binder’s function in a slip is to act as a bridge between particles to provide green strength to the compact after drying. A plasticiser is used to soften the binder in the dry or semi-dry state to impart flexibility to the compact [83]. In this study two binder to plasticiser ratios of 1:1 (0.5 dw.% : 0.5 dw.%) and 1:2 (0.5 dw.% : 1.0 dw.%) mixing with 43 vol.% (77 wt.%) of Ti powders and 0.3 dw.% of dispersant (DP64), were selected to test their effect on the casting rate and green strength. From experimental trials, a slip-cast with a binder to plasticiser ratio of 1:2 took almost twice as long to form a casting than slips with a ratio of 1:1. Nies and Messing [130] investigated the change in the gel formation temperature of a binder (PVA) with increasing content of plasticiser (PEG400). They claimed that a higher amount of plasticiser lowers the gel formation temperature to such a degree that liquid was not able to flow to the surface and be absorbed by the plaster mould. In flexure tests carried out to determine green strength, a cast with a 1:2 binder to plasticiser ratio had half the maximum flexure stress compared with a cast with a 1:1 ratio (Figure 4-6). A 1:2 ratio also had twice the degree of flexibility compared with a cast formed using a 1:1 ratio. This is because the plasticiser breaks the bonding and alignment of binder molecules, therefore higher amounts of plasticiser lowers the strength and increases the flexibility.

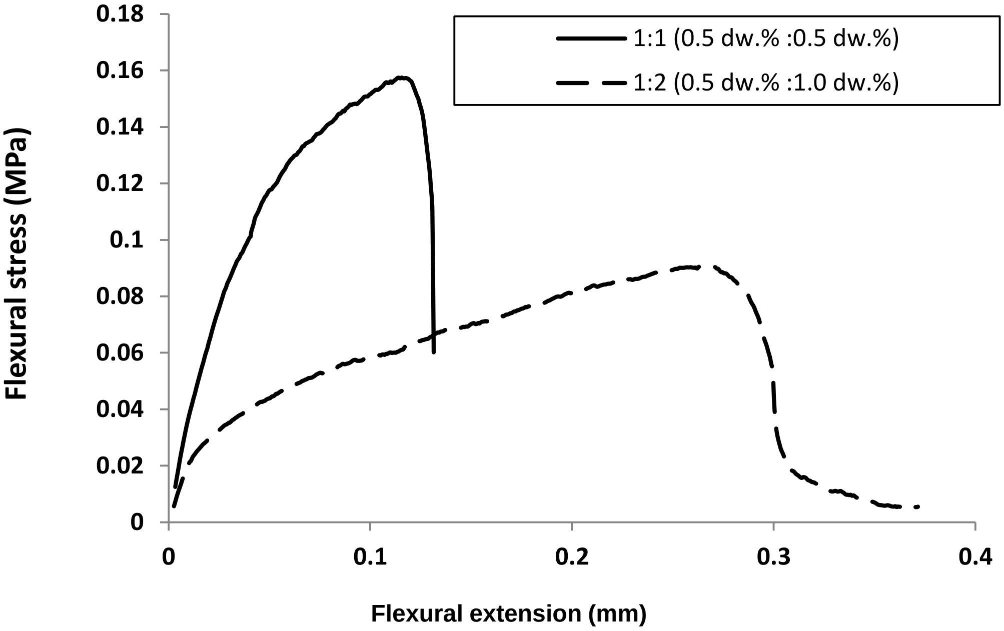

Figure 4-6 Flexural stress-extension curve of the slip, when cast with different ratios of the binder and the plasticiser.

The amount of binder and plasticiser was then studied using a 1:1 ratio. The graph below shows the relationship between green density, viscosity and binder (PVA) concentration (Figure 4-7). The viscosity increases with binder concentration, whereas the green density remains constant. The maximum bending strength as a function of the concentration of binder (PVA) is plotted In Figure 4-8. Using this information, 0.8 dw.% of binder (PVA) was chosen because it gave sufficient handling strength to allow transfer of samples after drying. Therefore, the slurry formulation was composed of 77 wt.% of Ti powders, 0.8 dw.% of binder (PVA), 0.8 dw.% of plasticiser (PEG400) and 0.3 dw.% of dispersant (DP64), with the balance being distilled water. The green compacts, rectangular compacts and tubular compacts were made from the slurry shown in Figure 4-9.

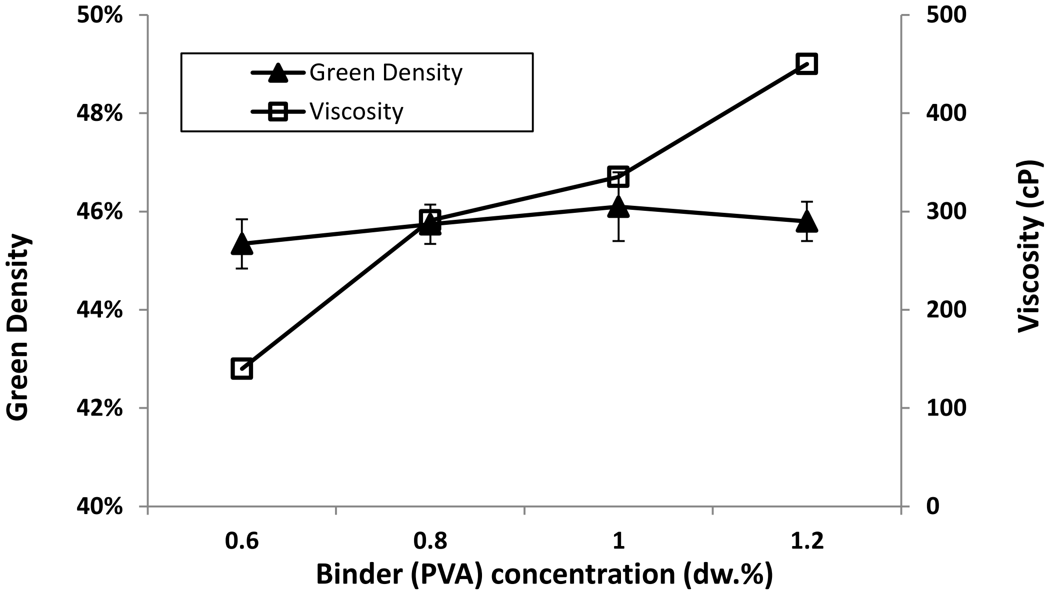

Figure 4-7 Viscosity of slips and green density of compacts after drying in terms of the binder concentration.

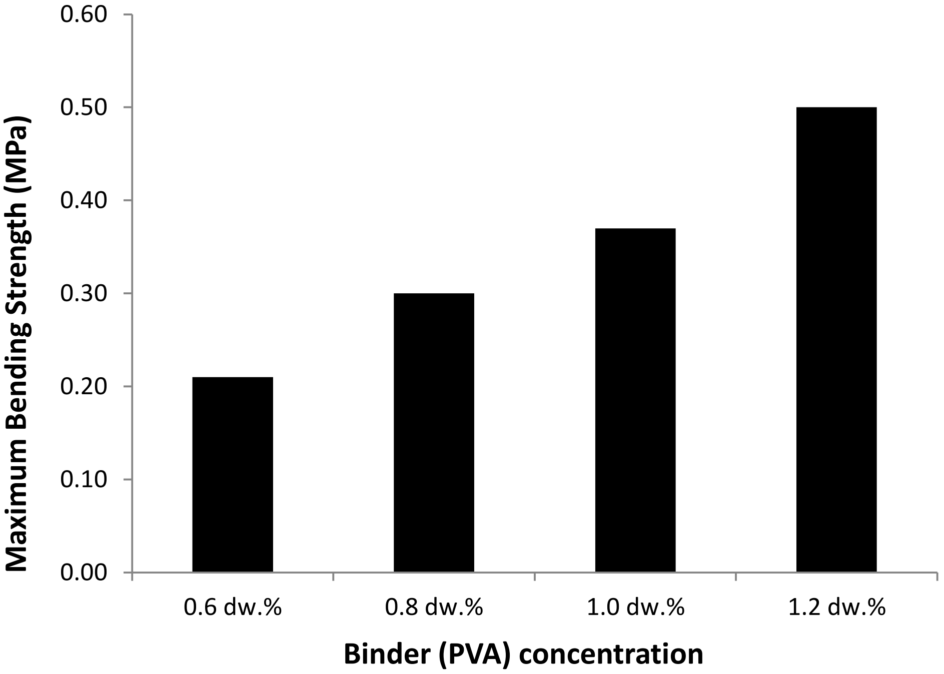

Figure 4-8 Three point bending strength of green compacts in terms of the binder concentration.

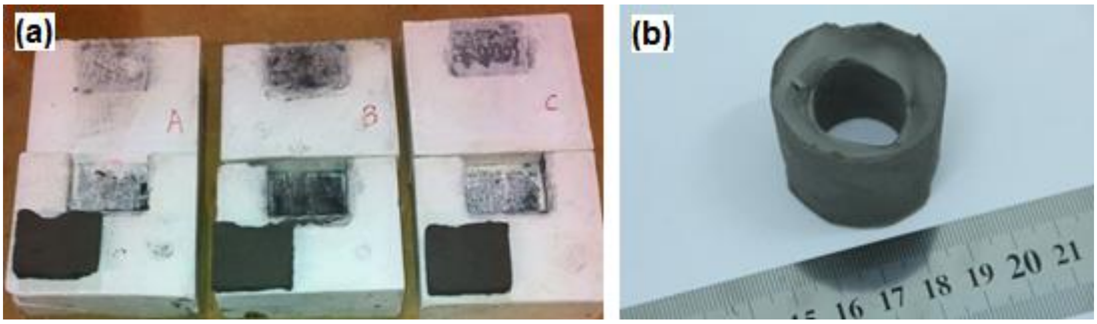

Figure 4-9 (a) green rectangular compacts; (b) green tubular compact.

4.2.4 Debinding study

Because of the large surface area of Ti in powder form, oxygen pick-up is always a problem. Using a low debinding temperature, preferably below 350°C, will be beneficial for reducing contamination from oxygen. Therefore, both thermogravimetric (TG) and differential thermal analysis (DTA) were performed on each individual organic component and its mixture, based on the optimized ratio (3:8:8), to examine thermal changes and the weight loss during the debinding stage under an argon flow of 150 ml/min (Figure 4-10). An argon atmosphere should protect the Ti compact from oxidation. The PVA component functions as the binder in this system of slurry (Figure 4-10(a)). The DTA curve in Figure 4-10a shows two endothermic peaks, at 195°C and 322°C, respectively. The first endothermic peak was due to the melting of PVA. The second peak was due to the thermal decomposition of PVA, which required heat to break down the chemical bonding. According to Lewis [131], thermal degradation of PVA undergoes a side group elimination, which removes the attached pendant side groups along its main chain. The TG curve clearly showed the rapid weight loss in the PVA from 300°C because of the onset of a decomposition reaction. At 600°C, PVA has 5 wt.% of residuals remaining. The PEG400 component, acting as the plasticiser, showed two endothermic peaks at 60°C and 347°C, respectively (Figure 4-10(b)). Because PEG400 is a liquid, as the temperature increased, evaporation took place, as indicated by the first endothermic peak. The second endothermic peak was associated with degradation. Due to the low molecular weight of PEG400, initial degradation is by random scission. Random scission refers to initiated or oxidative decomposition of a wide range of low molecular weight fragments [131]. Madorsicy and Straus [132] found that 90% of this polymer decomposes into waxy substances which are volatile at above 350°C. On the other hand, the TG curve for PEG400 showed significant weight loss from 300°C to 370°C. And at 600°C, PEG400 has only 0.3wt.% residuals remaining. DP64 is the dispersant and this showed two significant endothermic peaks at 100°C and 220°C, respectively (Figure 4-10(c)). The first endothermic peak was due to evaporation, because DP64 is in a liquid form, and the second peak at higher temperature was caused by the thermal decomposition of DP64. DP64 showed continual weight loss over the temperature range between 25°C and 600°C, but at 600°C, 8wt.% of residuals remained. By looking at the overall thermal change of the organic mixture (Figure 4-10(d)), there are three endothermic peaks at 65°C, 190°C, 305°C, respectively. These three peaks matched up with the decomposition reactions of the individual organic additives. The weight loss for the binder mixture fell significantly by 80wt. % in the temperature range 200°C to 340°C, and only 3wt.% residuals were left at 600°C. As oxygen starts to adversely affect Ti above 350°C, and based on the results shown in Figure 4-10, a maximum debinding temperature of 320°C was selected. On average, a debinding holding time of 2 hours at 320°C reduced by 80% the amount of organics in the green compacts, when using a heating rate of 1°C/min. The remaining 20% would acts as a backbone binder to provide strength to the partially debound compacts and this residue will be removed by vacuum sintering.

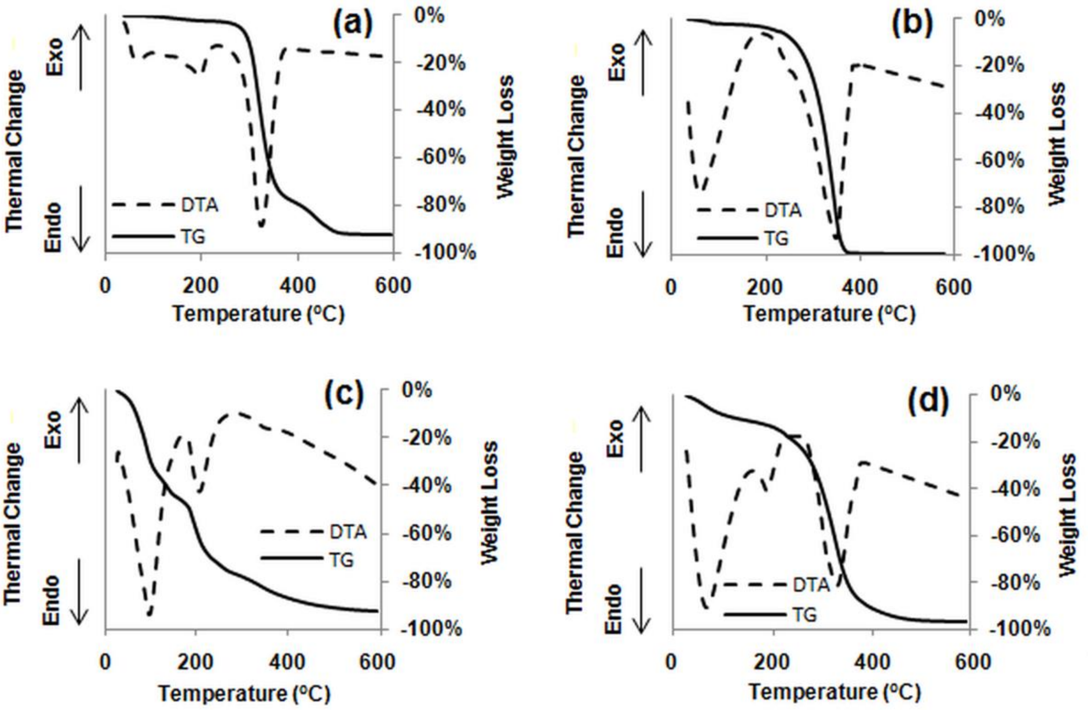

Figure 4-10 DTA/TG curves of organic additives; (a) PVA; (b) PEG400; (c) DP64; (d) the mixture of organics.

4.2.5 Sintering Study

Sintered rectangular and tubular compacts were produced (Figure 4-11). The Ti compact sintered at each of 1000°C and 1200°C for 0.5 hours gave a relative density of 70.7 ± 0.5 % with an open porosity of 24.4 ± 0.8% and a relative density of 83.2± 0.5% with an open porosity of 9.9 ± 0.4%, respectively. The tensile stress-strain curves (Figure 4-12) of sintered porous compacts showed that the higher density sintered compact at 83.2% of full density had a yield stress of 400 MPa, a fracture stress of 479.2 MPa and an elongation to fracture of 6.8%.The lower density sintered compact at 70.7% of full density had a yield stress of 238.2 MPa, a fracture stress of 276.2 MPa and an elongation of 2.6%. These results are satisfactory for the intended applications; for instance, as an anode used for chlorine generation in water disinfection. The fracture surfaces of tensile specimens are shown in Figure 4-13. It can be seen that a compact sintered at 1000°C has more pores than that sintered at 1200°C. Some ductile features (Figure 4-13(c) & (d)), for example, microvoid coalescence, as indicated by arrows, can be observed in the necked area and also pores bounded by a crystalline granular structure.

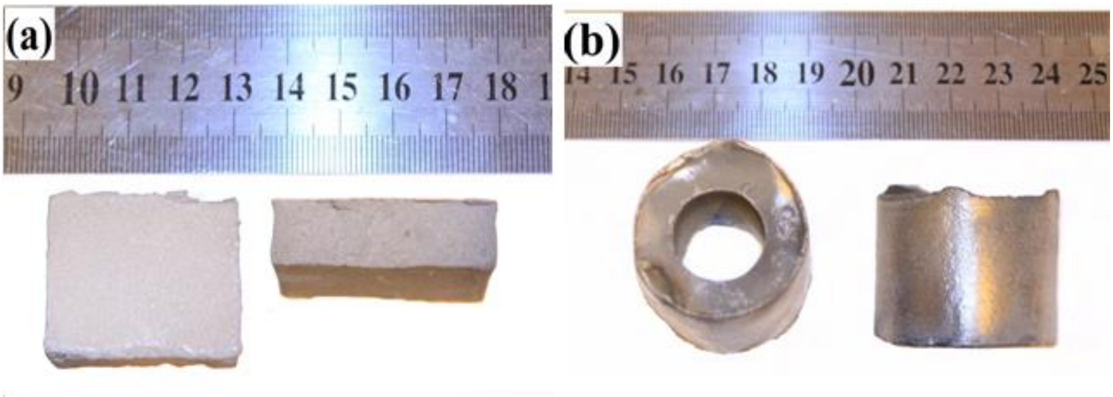

Figure 4-11 Images of sintered compacts; (a) rectangular shaped compact; (b) tubular compact.

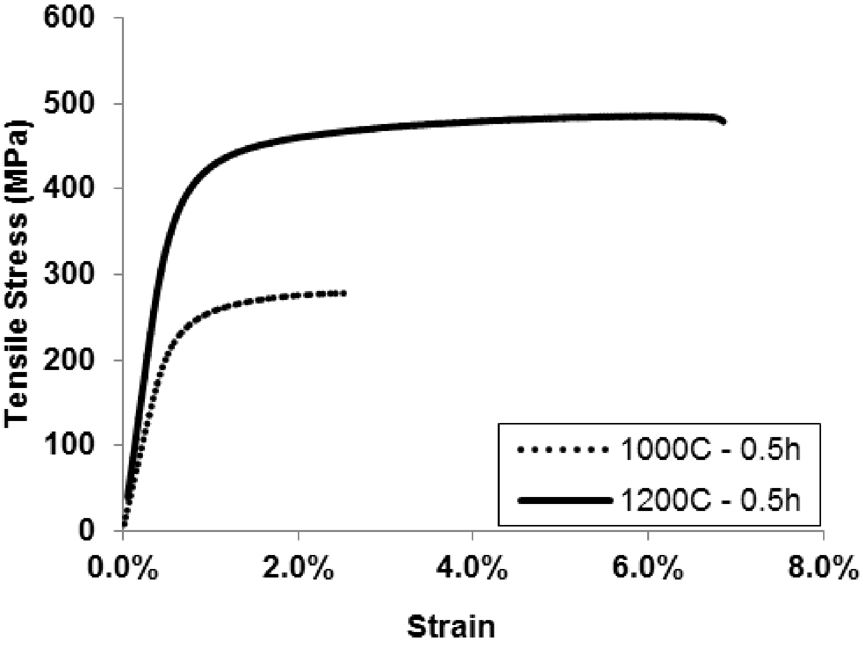

Figure 4-12 Stress-strain curves of porous compacts sintered for 0.5 hours at 1000°C and 1200°C.

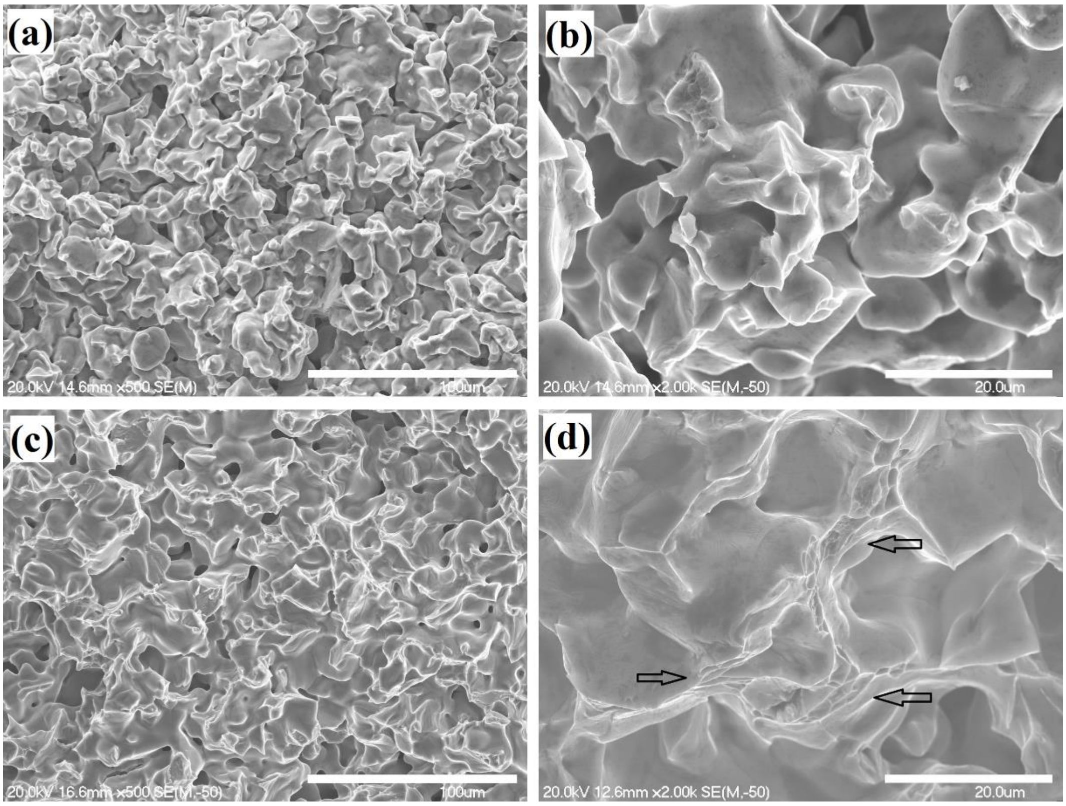

Figure 4-13 SEM images of the fracture surfaces of porous compacts after tensile testing; (a) & (b) the compacts sintered at 1000°C for 0.5 hours; (c) & (d) compacts sintered at 1200°C for 0.5 hours.

The oxygen and carbon content of the as-received Ti powder, debound Ti compact and sintered porous compacts are listed in Table 4-1. After sintering, the average increase in oxygen level was about 0.14 wt.% and the average increase in carbon level was about 0.03 wt.%. As indicated by Jaffee et al. [133], the critical value of the oxygen content is about ~0.5 wt.% for loss of tensile ductility in bulk Ti and also the maximum limit of carbon content in Ti is up to about 0.3 wt.%, which reduces ductility to some extent. Table 4-1 shows that both the oxygen and carbon content of sintered porous Ti compacts were below the critical values. The result is encouraging, since it shows the feasibility of using this slurry formulation in the slip casting process for Ti and the effectiveness of the debinding process, developed from the slurry formulation.

Table 4-1 Carbon and oxygen content of Ti powder, debound Ti compacts and sintered compacts.

Sample	Oxygen Content (wt. %)	Carbon Content (wt. %)
As-received Ti powder	0.32	0.02
Debound Ti	0.38	--
Sintered Ti (1000ºC)	0.46	0.05
Sintered Ti (1200ºC)	0.47	0.05

The peak intensities from an XRD pattern (Figure 4-14b) of sintered compacts identified the material as pure alpha Ti, which are identical to the peaks of the as-received Ti powders. It is evident that residuals from organic additives have not contaminated the Ti matrix and no TiC phase was formed at a level detected by XRD. Ohkawa et al. [16] underwent a similar study of Ti slip casting for dental applications using sodium alginate as a binder. They fabricated a relatively low porosity level of Ti products ranging from 4 vol.% to 20 vol.%. The tensile stress obtained only varied from 200 MPa to 300 MPa with a negligible amount of elongation. A major limitation in their study was the formation of a TiC phase deriving from the decomposition of organic additives. As a result, the densification process was hindered and a brittle sintered part was produced. In this study, no TiC phase was detected by XRD and promising mechanical properties, with acceptable levels of ductility were obtained. Additionally, the porosity levels of sintered compacts can be controlled by varying the sintering conditions. The results also suggest that the binder formulation used in this study has little detrimental effect on the Ti powders and the debinding process is effective in removing any organic residuals.

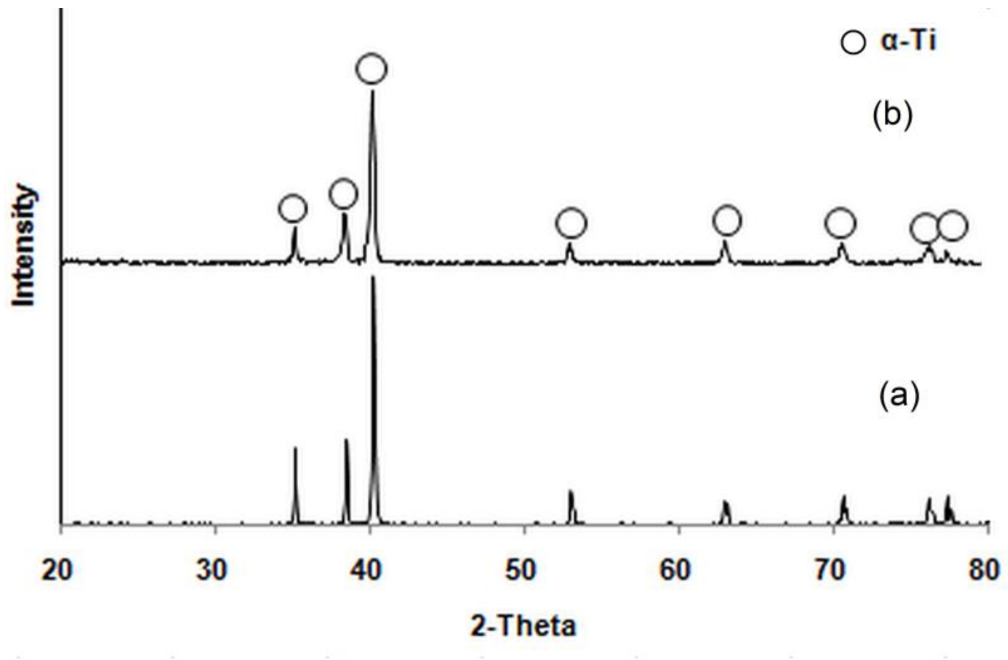

Figure 4-14 X-ray diffraction (XRD) patterns of Ti in two different forms; (a) as-received HDH Ti powders; (b) sintered Ti compact.

4.2.6 Application

A potential application for slip cast Ti compacts is as an electrode in a water purification process. A large Ti slip cast compact was produced as shown in

Figure 4-15. Five different locations were labelled to examine the homogeneity of the microstructure in the slip cast compact. In Figure 4-16, the five images show very porous microstructure and the pores are irregularly shaped. A machined electrode from the slip cast Ti compact is shown in Figure 4-17. Compared with the traditional press and sintering route, the slip casting process does not require any metal moulds and powerful presses to produce such a large dimension. In addition, the slip casting process allows for a low level of powder contact and a porous body can be easily produced.

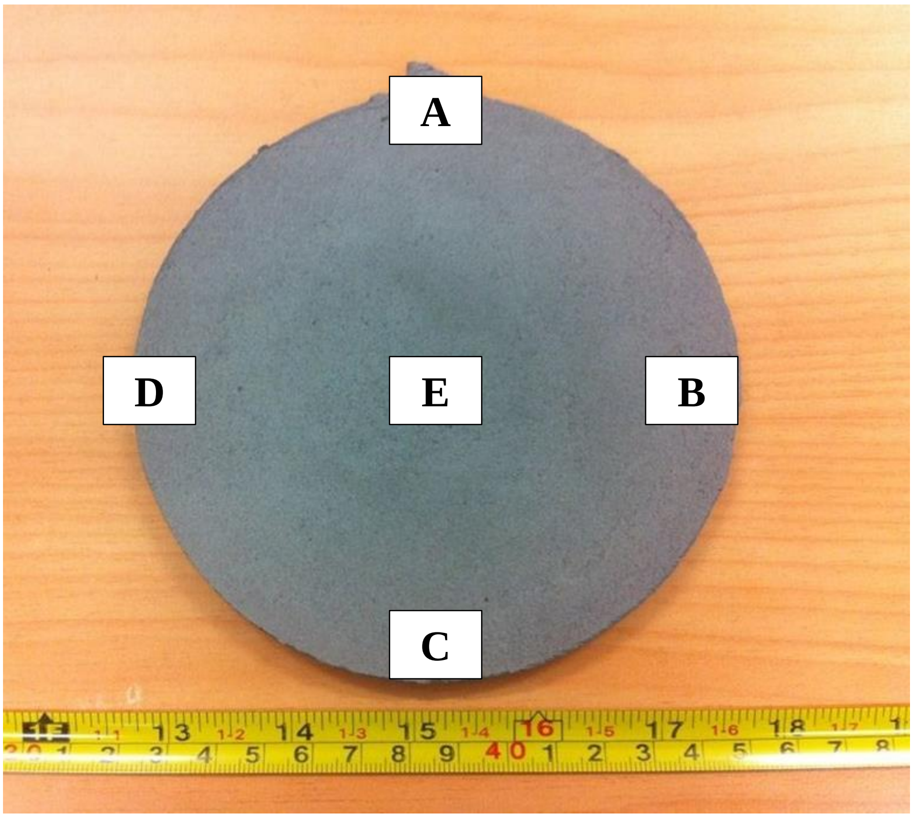

Figure 4-15 A large compact, 120mm in diameter and 8 mm in thickness. Different locations were labelled for microstructural analysis.

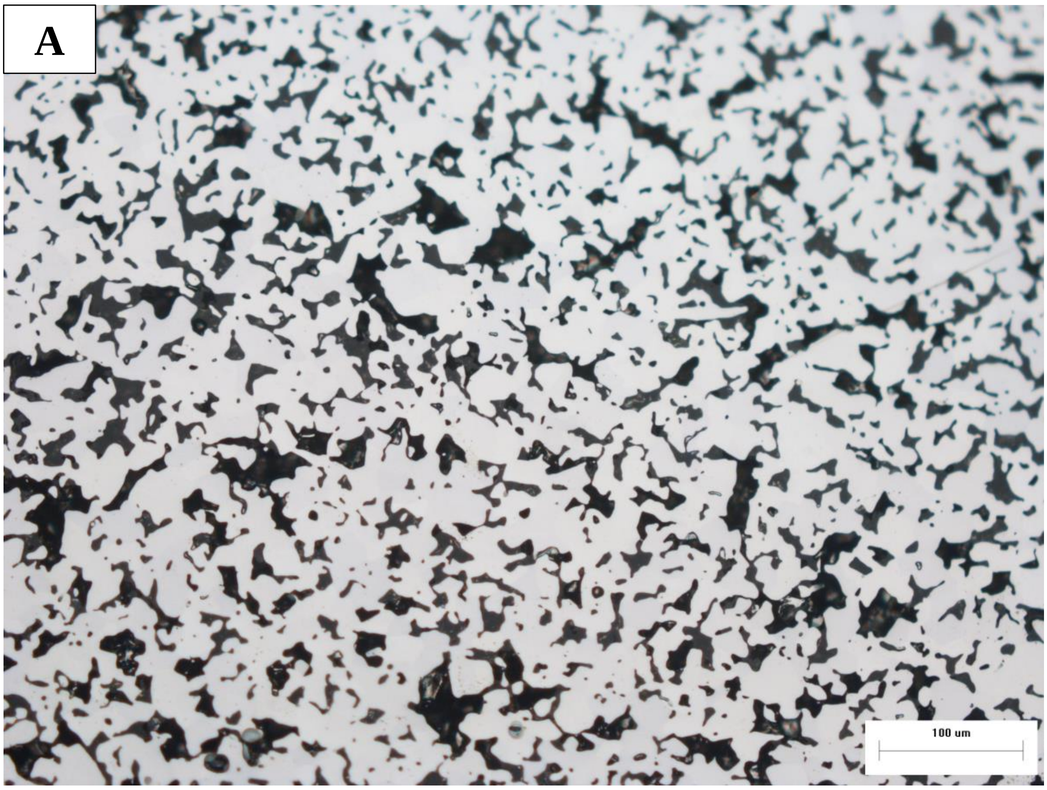

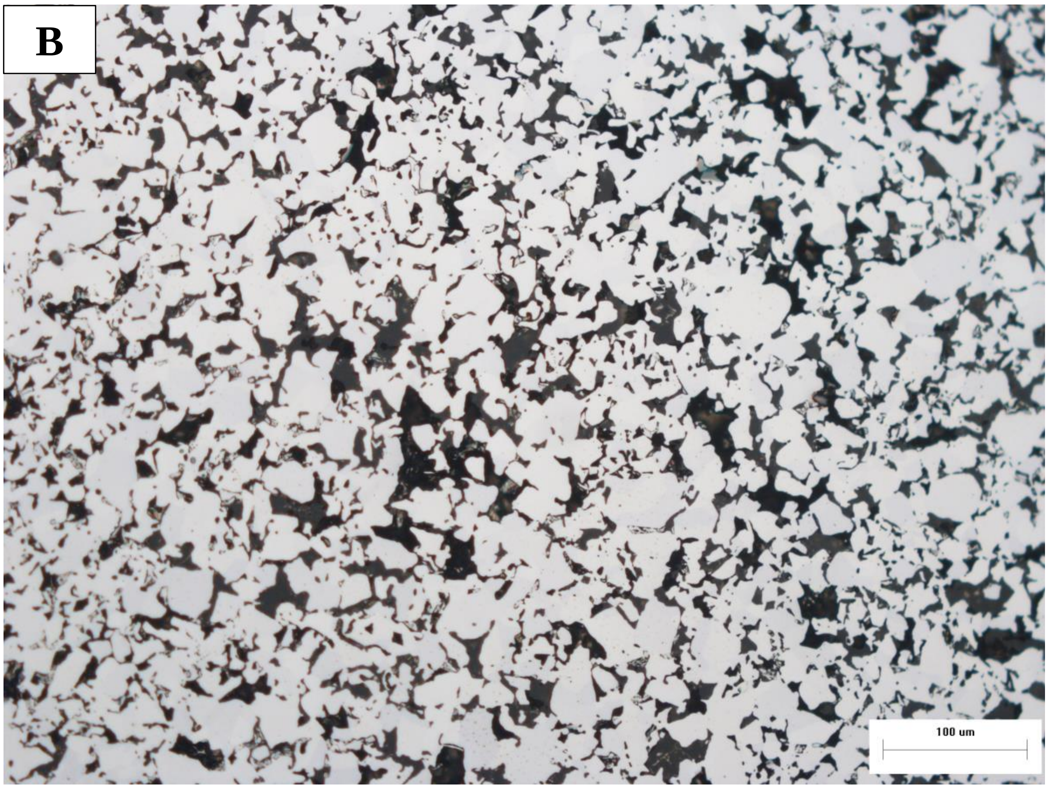
B
100 um

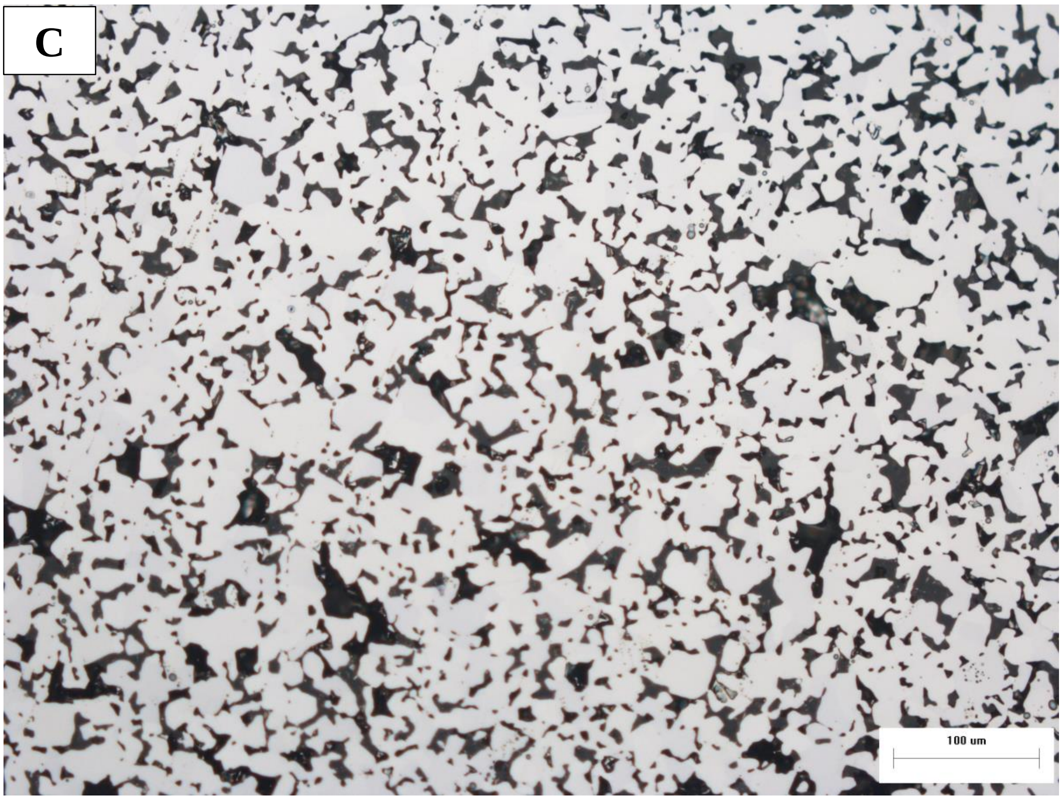
C
100 um

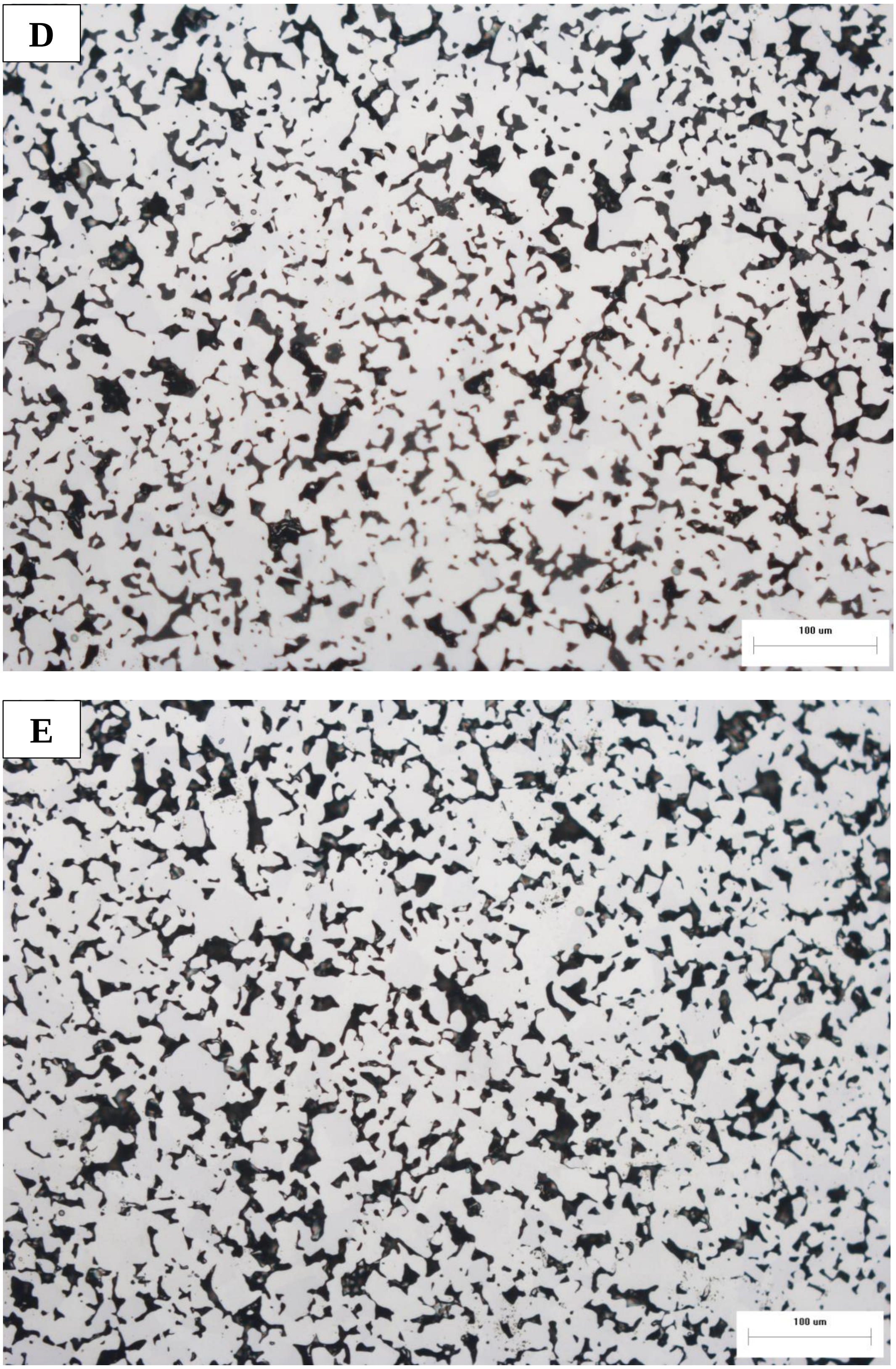

Figure 4-16 The microstructures from different locations in the compact as labelled in Figure 4-15.

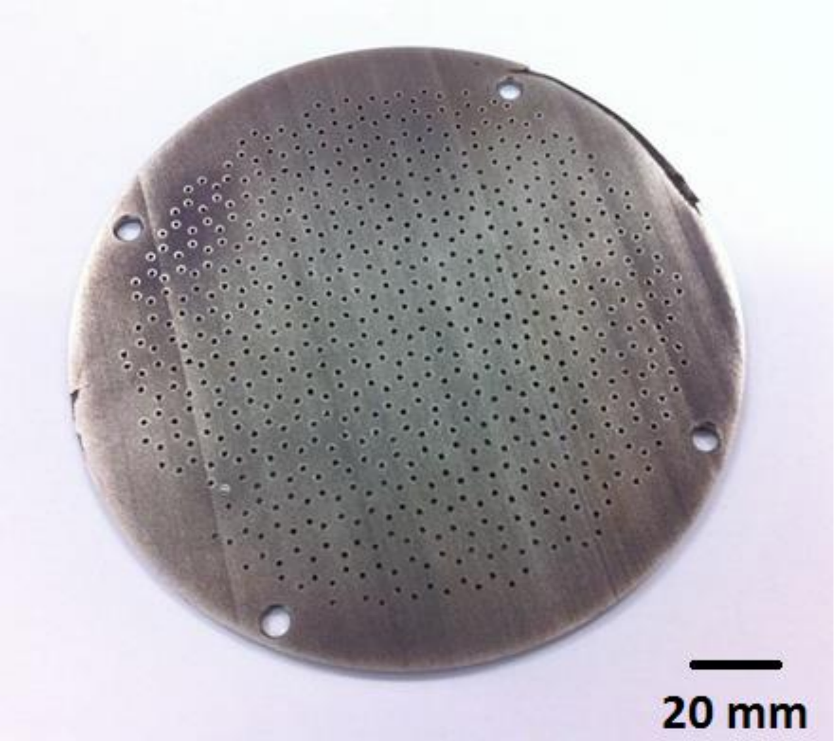

Figure 4-17 A machined electrode from a slip cast compact.

4.3 Conclusions

This work describes a slip casting process with a potential for creating a low cost, simple route to shape Ti compacts with porosity. Based on the developmental process of Ti slip casting presented above, the following conclusions can be drawn:

- A unique Ti slurry for slip casting was developed, which was composed of 43 vol.% (77 wt.%) Ti powder, 0.3 dw.% of dispersant, 0.8 dw.% of plasticiser and 0.8 dw.% of binder, mixed with a balance of distilled water. The dispersant with optimum performance is Dolapix CE64 at 0.3 dw.% and with a pH of 7.
- The debinding temperature was optimized at 320°C for 2 hours under an argon flow rate of 150ml/min, which minimizes the amount of carbon contaminants remaining on the compacts.
- The sintering study showed that the porosity of compacts can be controlled by varying the sintering conditions. Ti compacts in the form of porous rectangular plates and tubes were able to be manufactured with promising

mechanical properties. Oxygen and carbon contamination was modest. No TiC and other contaminated phases were detected by XRD.

- It was demonstrated that a large compact, 120 mm in diameter and 8 mm in thickness, was produced by the slip casting process. The microstructures were homogenous with pores in irregular shape. The potential application for such a slip casting plate is as an electrode in a water purification process.

5. Chapter 5 – Study of porosity, gas permeability and mechanical properties on the sintered slip cast compacts

5.1 Introduction

Porous Ti is an excellent filter material used in the chemical and processing industries, owing to its outstanding corrosion resistance, high strength-to-weight ratio, large specific surface area and high gas and liquid permeability [134]. A stable and permanent thin layer of TiO_2 forms on the surface of Ti at room temperature, and it is able to regenerate immediately after damage. This thin film of TiO_2 allows Ti to be used in highly corrosive environments and aggressive media in which stainless steel cannot provide sufficient corrosion resistance, such as seawater, oxidising chlorine, salt acidic solutions containing oxidants, etc [135, 136]. For ceramic filters, fragility is a main issue in practice and thermal shock is another potential problem which limits their use when there are frequent and rapid changes in process gas temperature [137]. Typical uses of porous Ti filters can be found in air and water purification processes [138, 139], filtering of Ti tetrachloride liquid [140] and in pulp and paper plants [135].

In powder metallurgy, sintering is one of the most important technological process, which is defined as a microwelding process for bonding powder particles together into a solid structure via mass transport that occurs largely at the atomic level [28]. The effects of sintering conditions on the densification of compacts in powder metallurgy have been well studied [28, 95, 141]. A number of researchers have investigated the sintering effect on the final density level, mechanical properties, pore size distribution, pore morphology and interconnectivity of compacts prepared by different powder metallurgy routes [18, 121, 142, 143]. Theoretical models have been established to understand the sintering behaviour in relation to the thermodynamics of densification [144, 145], diffusion mechanisms [146-149] and pore distribution [150-152]. Furthermore, the investigations have been undertaken to link the mechanical behaviour of the material with the porosity level, pore size distribution, pore morphology and interconnectivity [29-31, 153]. It was found that under tensile loading, interconnected pores have a more detrimental effect on the ductility of porous compacts than isolated pores, because more strain is localised around regions of interconnected porosity, whereas the strain distributes more homogenously over materials with isolated pores [30].

The porous Ti compacts in this study were produced by a slip casting route, which, in the previous chapter was demonstrated to be a feasible process for manufacturing porous Ti products. In order to obtain high efficiency in the planning and analysis of experimental data, the Taguchi's method was employed in this study. It proved to be a robust and reliable technique. There is a general understanding of the effects of porosity on materials made by powder metallurgy and this has been reported [28, 123]. To the best of our knowledge, a comprehensive and quantitative understanding of the effect of porosity on the mechanical behaviour of Ti produced by slip casting has not yet been reported. In this chapter, the effect of porosity on gas permeability, pore size distribution, pore shape, degree of interconnected pores and mechanical behaviour of slip cast Ti has been examined. Moreover, theoretical models and experimental work from previous researchers have been compared with the current experimental results to enhance our understanding of the slip casting process.

5.2 Results & Discussion

5.2.1 Taguchi design of experiments

Porous Ti compacts with porosities in a range of 10.7 vol.% to 35.3 vol.% were fabricated by slip casting (Table 5-1). The porosity range was controlled using different sintering conditions, such as sintering temperature (1000°C, 1100°C & 1200°C), sintering time (0.5 h, 1 h & 2 h), heating rate (5°C/min, 7°C/min & 10°C/min) and cooling rate (5°C/min, 10°C/min & Furnace Cooling (F/C)) and Taguchi Design of Experiment were applied to the porosity measurements to establish the significance of the different conditions. Detailed sintering parameters were presented in Chapter 3, section 3.5.

The analysis of variance (ANOVA) technique was performed to establish the relative significance of the factors. Table 5-2 shows the results of the ANOVA analysis. The sintering temperature presents the most significant effect on the total porosity level of compacts, followed by the sintering time. The cooling rate has a slight effect compared with the heating rate because the cooling rates have large differences, whereas the heating rates only vary from 5°C/min to 10°C/min. For our typical vacuum furnace, a furnace cooling rate is about 100°C/min when the furnace temperature is above 1000°C, followed by a slightly slower cooling rate of 50°C/min when the furnace temperature drops below 800°C. The vacuum furnace cooling rates can be modelled as an exponential decay curve as shown in Figure 3-5.

Table 5-1 The total porosity of porous Ti compacts sintered under various conditions, prepared by slip casting.

Run No.	Replication, porosity (%)			Total Porosity (%)
	1	2	3	
T1	29.3%	31.0%	28.9%	29.7% ± 1.1%
T2	19.2%	23.1%	21.4%	21.2% ± 2.0%
T3	15.9%	16.8%	16.6%	16.4% ± 0.5%
T4	11.6%	12.2%	13.1%	12.3% ± 0.8%
T5	35.5%	35.0%	35.4%	35.3% ± 0.3%
T6	21.9%	19.3%	22.3%	21.1% ± 1.6%
T7	14.6%	15.0%	15.0%	14.8% ± 0.2%
T8	10.7%	11.8%	9.7%	10.7% ± 1.1%
T9	25.9%	29.4%	27.8%	27.7% ± 1.7%

Table 5-2 ANOVA analysis of sintering parameters.

Factor	DOF	Sum of Squares	Variances	F value	Percentage
Sintering Time (h)	2	0.015	0.007271	43.7	8.46%
Cooling Rate (°C/min)	2	0.006	0.003024	18.1	3.52%
Heating Rate (°C/min)	2	0.002	0.000905	5.4	1.05%
Temperature (°C)	2	0.147	0.073272	439.6	85.23%
Error (e)	18	0.003	0.000167		1.74%
Total	26	0.169			100%

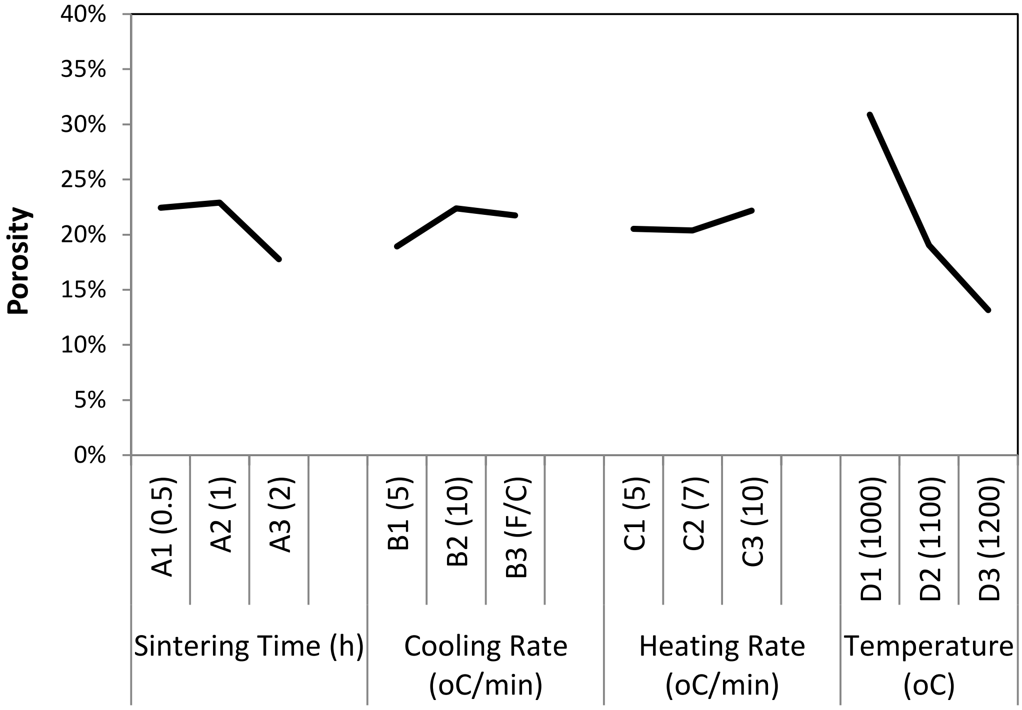

Figure 5-1 Response graph of total porosity against sintering conditions.

Figure 5-1 illustrates the responses of the average total porosity level from four sintering factors. To predict the total porosity level, an expression [154] was used:

$$\boldsymbol{P'_{total} = \overline{P}_{avg} + (P'_{time} - \overline{P}_{avg}) + (P'_{cr} - \overline{P}_{avg}) + (P'_{hr} - \overline{P}_{avg}) + (P'_{temp} - \overline{P}_{avg})} \qquad \textbf{(5-1)}$$

where P'_{total} is the predicted total porosity level of a compact, P'_{time} is the corresponding porosity level for the sintering time appearing in Figure 5-1, P'_{cr} is the corresponding porosity level for the cooling rate, P'_{hr} is the corresponding porosity level for the heating rate, P'_{temp} is the corresponding porosity level for the sintering temperature and $\overline{P}_{avg}$ is the average porosity value (21 vol.%) from the nine Taguchi experiments. From Equation 5-1, in this sintering practice, the maximum controllable porosity could be up to 33.7 vol.% and the minimum porosity could be 7.2 vol.%.

Based on this information above, a further confirmation test was allocated to produce porous compacts with a 30 vol. % porosity level. To find the optimum process, the sintering temperature is the first factor to consider because it has the most significant impact on the porosity, followed by the sintering time. In this case, from Figure 5-1, a sintering temperature at 1000°C gives about 30 vol.% of porosity and a sintering time of 2 hours gives about 21 vol.% of porosity. From an industrial perspective, a slow heating rate and cooling rate would consume more energy and prolong the operation time, which raises processing costs. As these two parameters have less effect on the porosity level, a heating rate at 10°C/min with furnace cooling is preferred. As a result, a theoretical porosity of 29.5 vol.% was obtained.

The 90% confidence interval (CI) for the expected yield from the confirmation tests can be obtained by using the following expression:

$$\boldsymbol{CI = \sqrt{F(1,18)V_e/3} = \sqrt{3.007 * 0.000167/3} = 1.3\%} \qquad \textbf{(5-2)}$$

Where F is the factor value, obtained from an F-table, and V_e is variance of error, obtained from Table 5-2. As shown in Table 5-3, it was found that the average total porosity obtained from the confirmation test, fell within the predicted 90% CI.

Table 5-3 Confirmation tests of the predicted total porosity level.

No.	Sintering Temperature (°C)	Heating Rate (°C/min)	Cooling Rate (°C/min)	Sintering Time (h)	Total Porosity (%)	Predicted total porosity (%)
A	1000	10	F/C	2	30.6% ± 2.0%	29.5% ± 1.3%

5.2.2 Open pores and permeability

Figure 5-2 shows the open porosity level (P_{open}) and permeability in the sintered Ti materials as a function of the total porosity (P_{total}), ranging from 12.3 vol.% to 35.3 vol.%. The gas permeability showed a strong positive linear correlation with the total porosity of sintered Ti compacts. A linear relationship was indicated between the total porosity and the open porosity for the sintered porous Ti compacts. The empirical relationship can be expressed as:

$$P_{open} = 1.02 * P_{total} - 0.06 \qquad 0 \le P_{total} \le 50\% \qquad \textbf{(5-3)}$$

It is interesting to note that the open porosity level of sintered porous Ti compacts reaches zero when the total porosity is about 6 vol.%. In other words, it is expected that all the pores are closed when the porosity level is below 6 vol.%. A similar finding was also concluded by Coleman and Beere [155]. They investigated the sintering of open and closed porosity using urania (UO_2), which showed that all the pores are closed when the residual porosity is below 8 vol.%.

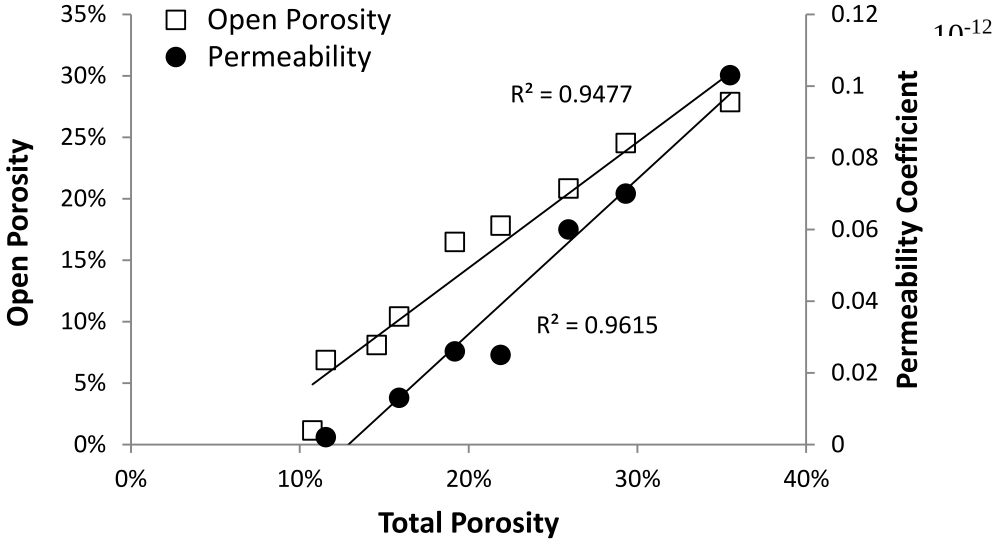

Figure 5-2 Open porosity level and permeability of sintered porous Ti compacts as a function of total porosity.

The open porosity fraction in Ti compacts, as a function of the total porosity produced by different processing techniques, is compared in Figure 5-3. Oh, et al. [18] showed the highest open porosity fraction in the porous Ti compacts, which were produced by powder press and vacuum sintering, using spherical Ti powders. The porosity level was controlled by the use of different sintering conditions (sintering temperature & sintering pressure) and the powder particle size varied from 65 μm to 374 μm. The high open porosity fraction was due to the large powder particle size. Erk, Dunand & Shull [15] employed thermoreversible gel casting of Ti hydride (TiH_2, ≤ 45 μm) with polypropylene spaceholders (35 μm) to fabricate porous Ti products. The volume of pores in their work depended on the volume fraction of spaceholders. After sintering for 10 hours at 1000°C, the pore size in their material ranged from 30 μm to 50 μm. A relatively low open porosity fraction at a similar level of total porosity was therefore produced. However, at a total porosity level above 35 vol.%, the corresponding open porosity fraction was close to 1, which was comparable with the result of [18]. By comparing the data from this study with these two techniques, slip casting showed an open porosity fraction at intermediate values.

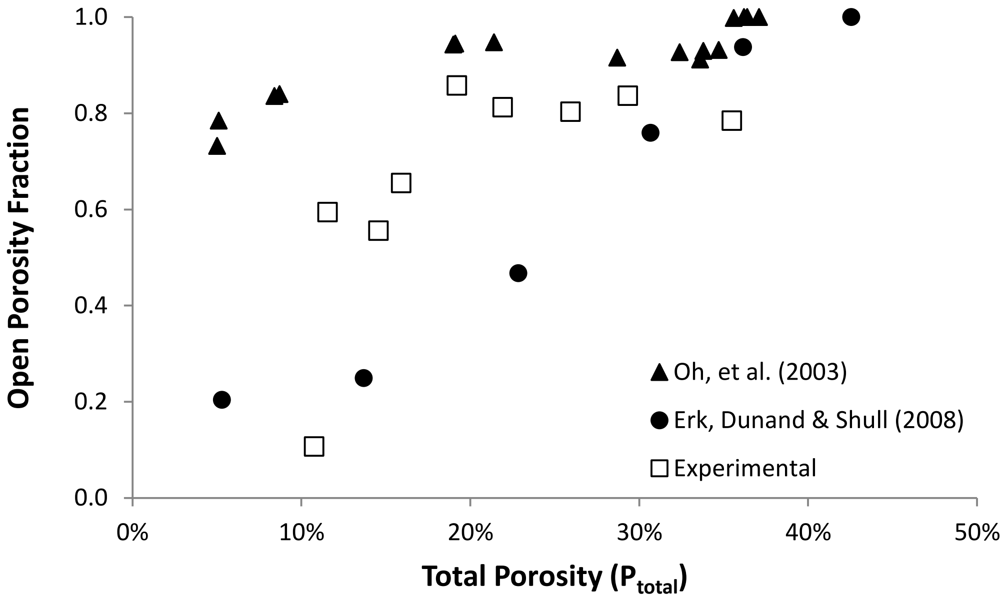

Figure 5-3 open porosity fraction in the porous Ti compacts as a function of total porosity.

5.2.3 Pore throat size analysis

As mentioned before, for each pore, the pore throat size is a measure of the most constricted diameter of the pore. As shown in Table 5-4, the average pore size in the compacts decreased with decreasing porosity level. However, the maximum pore size in the compacts was random. The measurement range of the pore size analyser is from 0. 1 µm to 100 µm, therefore, the average pore size in a porous compact, with 12.3 vol.% porosity, was too small to measure.

The powder particle size of the raw Ti materials has a significant impact on the pore size. Hirschhorn [156] fabricated porous Ti compacts using powder ranging from 88 µm to 149 µm. He noted that at porosity levels of 35 vol.% to 40 vol.%, the average pore size in the compacts was from 10 – 15 µm. At a porosity level of about 15 vol.%, the average pore size was about 1 – 2 µm. For the slip casting process in this study, very fine powder (≤ 44 µm) was used, which produced much smaller pores in the Ti compacts. This information could be a way of controlling the pore size to give different levels of porosity.

Table 5-4 The pore throat size analysis on the different porosity level of sintered Ti compacts.

Porosity	Average Pore Throat Size (µm)	Maximum Pore Throat Size (µm)
27.7%	0.5	3.5
21.2%	0.3	2.2
16.4%	0.2	2.9
12.3%	--	1.6

5.2.4 Interconnected pore characterisation

In order to characterise the interconnected pores, ammonium meta-tungstate (AMT) was used as a medium to seep through the porous Ti compacts. At temperatures above 450^{o}C, AMT formed tungsten trioxide. In Figure 5-4, energy-dispersive x-ray spectroscopy (EDX) mapping shows a typical interconnected pore in the treated porous Ti compacts, which demonstrates that tungsten oxide can fill up, or at least coat the inside of the interconnected pores. Pores that showed no evidence of the presence of WO_3 were assumed to be isolated pores and not connected in any way to the surface. In Figure 5-5, Ti compacts with different porosity levels (27.7 vol.%, 21.9 vol.%, 16.4 vol.% & 12.3 vol.%) were treated with AMT and the backscattered electron images revealed the interconnected pores, which shows up as the lighter areas in the micrographs. As the porosity level decreased, the percentage of interconnected porosity was reduced. In Figure 5-5(c), a few isolated pores were observed, as pointed out by the arrows. At a porosity of 12.3 vol.%, the pore size decreased further and there was less porosity, so the magnification used for SEM imaging was lowered to better illustrate the overall distribution of interconnected pores in the compact. There is also an increase in the number of isolated pores that can be observed and the pore shape is more spherical (Figure 5-5(d)).

Dullien [157] mentioned a similar interconnected pore characterisation technique using Wood’s metal, which is a eutectic alloy with a low melting point of 70^{o}C. The porous metal is impregnated with molten Wood’s metal. When cooling, the interconnected pores are easy to distinguish using backscattered electrons. However, Wood’s metal is extremely harmful to human health, especially the vapour from molten Wood’s metal, due to the involvement of lead and cadmium in the composition. The method presented here, using ammonium meta-tungstate, is more effective.

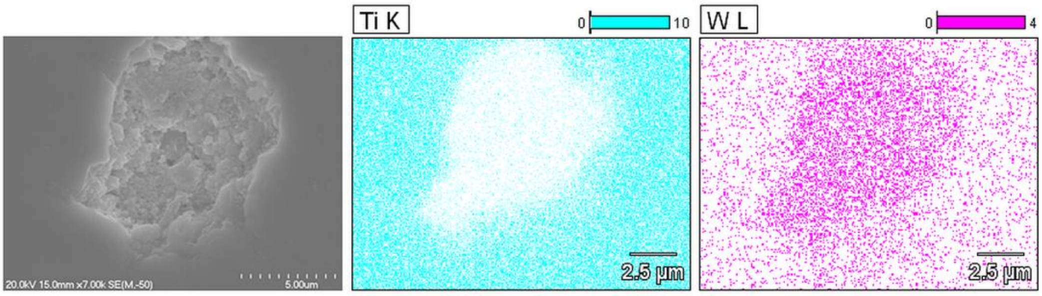

Figure 5-4 Energy-dispersive X-ray spectroscopy (EDX) mapping analysis of an AMT impregnated porous Ti compact after heat treatment. Bright areas are low concentration and dark areas are high concentration.

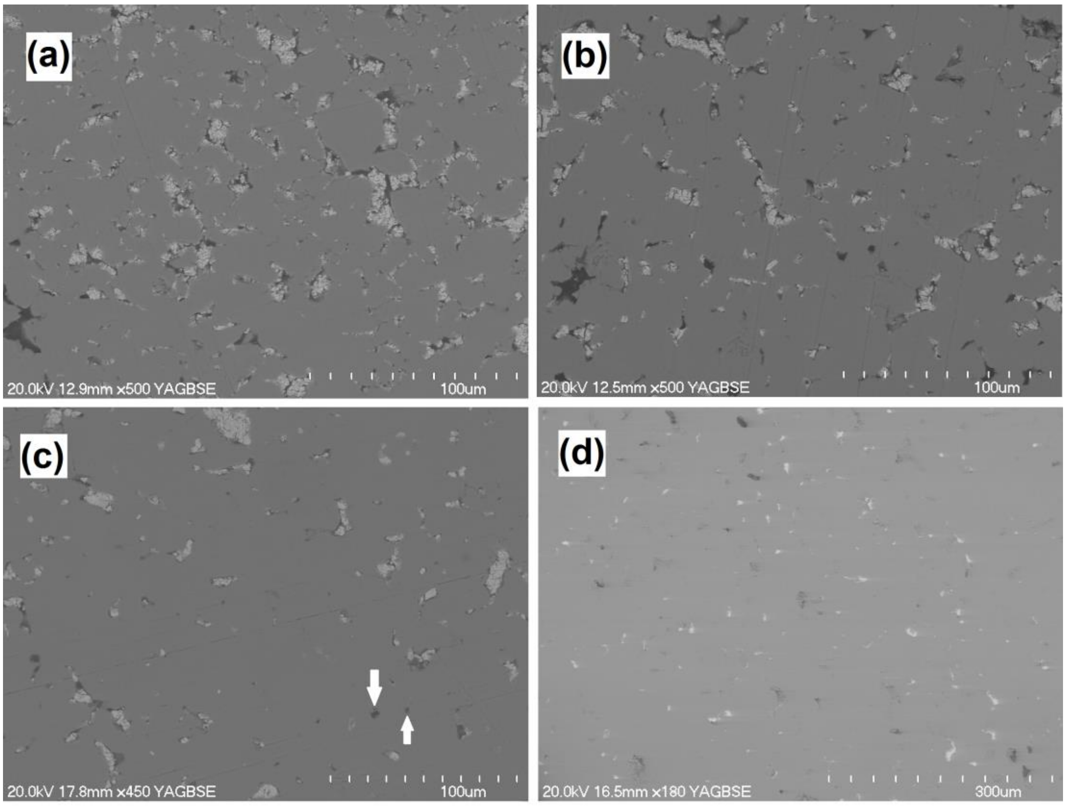

Figure 5-5 Backscattered electron (BSE) images of interconnected pores in the porous Ti compacts at different porosity levels; (a) 27.7 vol.% porosity; (b) 21.9 vol.% porosity; (c) 16.4 vol.% porosity; (d) 12.3 vol.% porosity. Isolated pores are pointed out by the arrows.

5.2.5 Tensile properties

The tensile tests were carried out on the slip cast Ti compacts at different porosity levels from 12.3 vol.% to 35.5 vol.%. The general looks of the tensile specimen and tensile fractured specimen were shown in Figure 5-6. Because the pores sizes are very tiny in micrometre, no obvious porous structure can be observed from the compact by eyes. The typical stress-strain curves were displayed in Figure 5-7 at different levels of porosity. The graph showed the yield strength point clearly and plastic deformation behaviour can be seen. However, no ultimate tensile strength can be obtained from the data whereas the fracture tensile stress produced the maximum value of tensile stress. In the following sections, the fracture tensile stress was used to express the tensile stress. The data of tensile stress and elongation were summarised by correlating with the level of porosity.

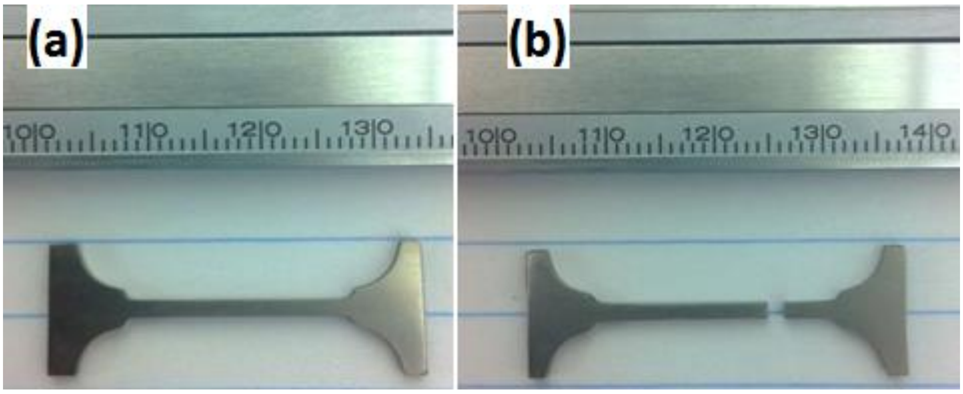

Figure 5-6 Tensile specimen machined from the slip cast Ti compact; (a) before tensile test sample; (b) tensile fractured sample.

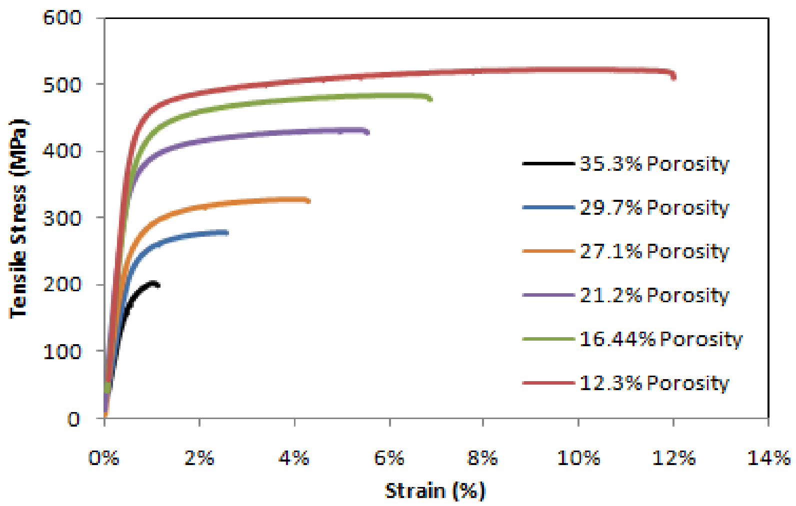

Figure 5-7 Typical stress-strain curves of the slip cast Ti compacts at different porosity levels.

5.2.5.1 Tensile strength (TS) of sintered porous Ti

Tensile testing results from Ti compacts with different levels of porosity showed that tensile strength was strongly dependent on the degree of porosity. From the data in Figure 5-8, by using regression analysis, an empirical relationship between the TS and porosity can be expressed as:

$$\frac{\sigma_t}{\sigma_o} = 1.3(1-2P), \; 0.1 \le P_{total} \le 0.5 \qquad \textbf{(5-4)}$$

where σ_t is the TS (MPa) of the porous material, σ_o is the TS of the bulk material (550MPa for Grade 4 Ti bulk material – ASTM B348-11) and P is the fractional porosity of a sintered compact. From Equation (5-4), it is reasonable to predict that $\sigma_t = 0$ MPa when P = 50.0 vol.%, which is close to the green density of a slip cast compact. However, Equation (5-4) also shows that σ_t = 730 MPa when P = 0 vol.%, which is above the TS of the bulk Ti material (550 MPa). Thus, it may only be feasible to use this equation for porosity levels above 10 vol.%.

In Figure 5-8, by fitting Griffiths's model, Fleck and Smith's brick model and Haynes's model to the experimental data, Haynes's model shows the best fit, which is almost identical to the trendline. For the Haynes's model, the *K* and *M* values were found to be 1.5 and 3, respectively. The *K* value can be an indicator of effective stress concentration factor. The *M* value implies that a moderate effect of both the geometry of the pores, and the interaction effect of stress concentrations around the pores, have been taken into account. Both the Griffiths's model and Fleck and Smith's brick model show a lower bound to the experimental data. In this case, the less successful Fleck and Smith's brick model, for predicting the relationship between strength to porosity, indicates that the interaction of stress concentration is an important factor that must be considered in porous Ti compacts produced by slip casting. In the Griffiths's model, the λ value is found to be 0.981 when using 550 MPa as the tensile strength of the bulk Ti. It is interesting to notice that by modifying the Griffiths's model, by using 730 MPa as the tensile strength of the bulk Ti and by altering the λ value to 1.3, as shown in Figure 5-8, the modified Griffiths's model displays a reasonable fit with the experimental data. However, 730 MPa is not a realistic value for the tensile strength of Grade 4 Ti materials, therefore, it implies that the Griffiths's model has limitations in predicting the tensile strength variation as a function of material porosity, whereas Haynes's model is more feasible to predict the tensile strength of porous Ti compacts produced by slip casting.

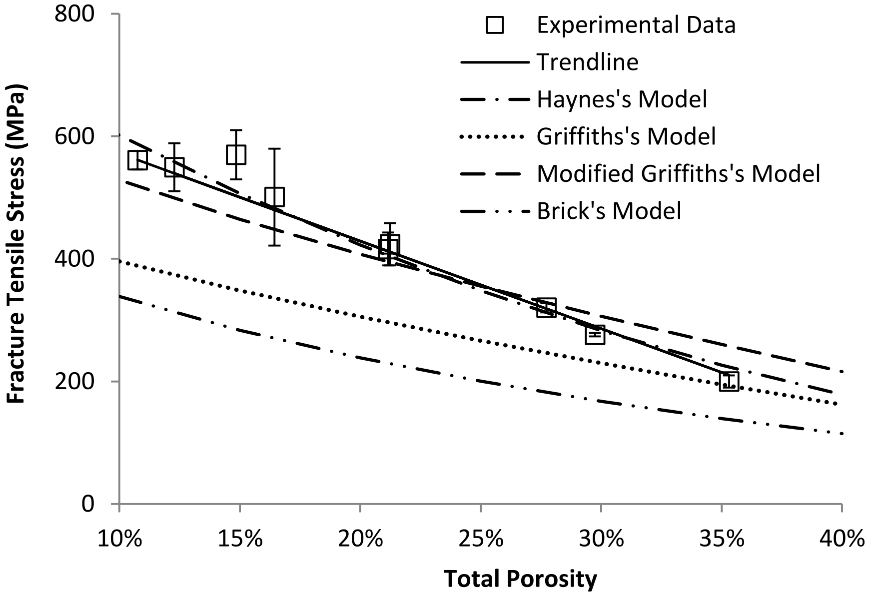

Figure 5-8 Plot of tensile strength against the porosity of sintered Ti compacts.

5.2.5.2 Ductility of sintered porous Ti

The relative ductility (the ductility of porous Ti divided by the ductility of bulk Ti) of sintered porous Ti compacts, prepared by slip casting, varied exponentially with the porosity level in the compacts (Figure 5-9 (a)). A linear trendline showed a poorer fit with the data. The elongation of the bulk Ti was 15%, which was obtained by extrapolating the trend line.

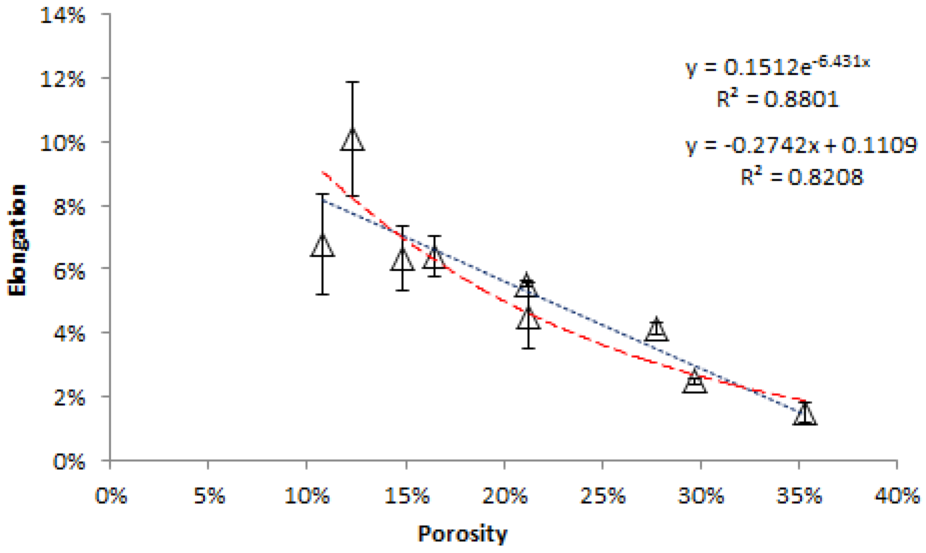

Figure 5-9 Plot of elongation against the total porosity of sintered Ti compacts.

As it can be seen in Figure 5-10, at a porosity of 12.2 vol.%, the average relative ductility of a porous Ti compact was 0.71, which is equivalent to an elongation of 10.7%. As the porosity increased to 35.5 vol.%, the relative ductility decreased to only 0.07, which is equivalent to an elongation of 1%. The *C* value in Haynes's equation (Equation 2-6) is adjustable, which is defined as a measure of the sensitivity of the ductility to the porosity content in the material. By fitting Haynes's equation with the data, the value obtained for *C* was 80 (Figure 5-10(d)). The ductility data from Hirschhorn et al.'s work [156], which investigated the ductility of porous Ti in a porosity range from 4 vol.% to 34 vol.%, is also presented in Figure 5-10b. Hirschhorn et al. produced Ti compacts with different porosity levels by varying the compaction pressure from 0.3 MPa to 965 MPa and then sintering. The elongation of bulk Ti materials used in the model was about 20%, which was estimated from their elongation graph. Comparing his data with the modified Haynes's model, the *C* value was also found to be 80. Furthermore, the data from Bourcier et al. [158] has been included in Figure 5-10(c). They fabricated porous Ti compacts with a porosity range from 0.3 vol.% to 8.7 vol.%, by a press and sinter approach, using a similar level of powder particle size as Hirschhorn et al.'s work. The elongation of bulk Ti used in this model was about 38%, which was also estimated from their data. By fitting the Haynes's model to

Bourcier et al.’s data, the *C* value obtained was increased to 1600, which is almost 200 times more than the *C* values obtained from the current work and Hirschhorn et al.’s work (Figure 5-10(e)). In Haynes’s model, the *C* value is defined as a parameter which measures the sensitivity of the ductility to the porosity content in the material. As Haynes mentioned in his paper, the *C* value may be an indicator of the ability of the material to strain harden. A low *C* value indicates that the material strain hardens strongly. In this work, the interstitial element oxygen may play a key role to affect the *C* values and also the ability of Ti to strain harden. The increased amount of the interstitial oxygen could strain harden Ti by increasing dislocation density [159]. In other words, the Ti products with the high oxygen content strain harden more strongly than those with a low oxygen content. The oxygen content level in Bourcier’s work was below 0.15 wt.%, which satisfied the requirements of Grade 1 commercially pure Ti (ASTM B348-11). Although Hirschhorn et al. did not mention the oxygen level in their as-sintered Ti compacts, the tensile strength of bulk Ti from their work was about 400 to 450 MPa and the elongation of bulk Ti was about 20%. To some extent, they were consistent with the standards of Grade 3 commercially pure Ti (ASTM B348-11). Grade 3 commercially pure Ti normally has a slightly higher oxygen content (0.35%) than Grade 1 commercially pure Ti. Furthermore, the average oxygen content in the current work was about 0.46%. Therefore, the differences in the *C* values should indicate the ability of Ti to strain harden, which is caused by the different amounts of interstitial oxygen.

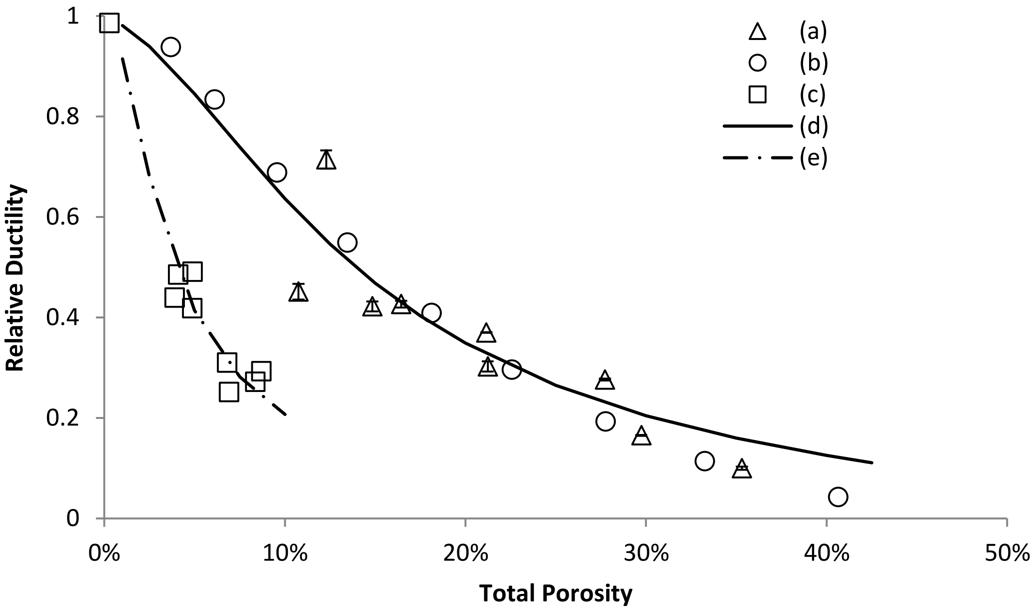

Figure 5-10 Plot of relative ductility against the total porosity of sintered Ti compacts. (a) experimental data from current work; (b) Data from Hirschhorn's work; (c) Data from Bourcier's work; (d) Modified Haynes's model with C = 80; (e) Modified Haynes's model with C = 1600.

5.2.6 Fractography

Figure 5-11 shows the fracture surfaces, and a view of the longitudinal plane for porous Ti specimens with different porosity levels, after tensile testing. At 29.7 vol.% porosity, the fracture zone was concentrated in the sintered necks (Figure 5-11(a)). The necked region was limited to the points between particles, as pointed out by the arrows. A significant number of sharp tips can be seen in the vicinity of the fracture in Figure 5-11(b). These are formed by discrete particles. This can be explained by the inefficient bonding strength between particles at this stage, causing some particles to be pulled out by the tension force. The pores were interconnected and irregular in shape, created by the initial packing structure of the sintered powder particles. At 21.2 vol.% porosity, there is a more densified microstructure in which some of the pores had become rounded and the necking area slightly larger due to the neck growth during densification , as pointed out by the arrows (Figure 5-11(c)). In the crack region, fewer sharp tips can be seen (Figure 5-11(d)). At 16.4 vol.% porosity, the fracture surface showed slip planes which indicated that the material had undergone some degree of ductile deformation under tension, as outlined in Figure 5-11(e), and the fracture necks are pointed out by arrows. In Figure 5-11(f), the fracture surface in the crack region is smoother than those seen in the previous two samples due to the lower porosity in the material. At 12.3 vol.% porosity, a few ductile dimples can be observed at some locations in the fracture surface, as pointed out by the arrows and the relatively small area indicates that densification of the Ti compact was not high enough. A large number of quasi-cleavage features can also be found in the material, as outlined in Figure 5-11(g). The fracture profile in Figure 5-11(h), shows a more flat surface, owing to the effect of lower porosity and smaller pore size in the material. Overall, the SEM micrographs of the fracture surfaces of the porous Ti samples show that cracks were propagated through the pores in the material. A high porosity level in sintered Ti leads to a brittle fracture surface and low porosity produces some areas of ductility in the fracture surface. Therefore, the porosity level and the pore size in the sintered Ti material have a significant effect on the tensile behaviour.

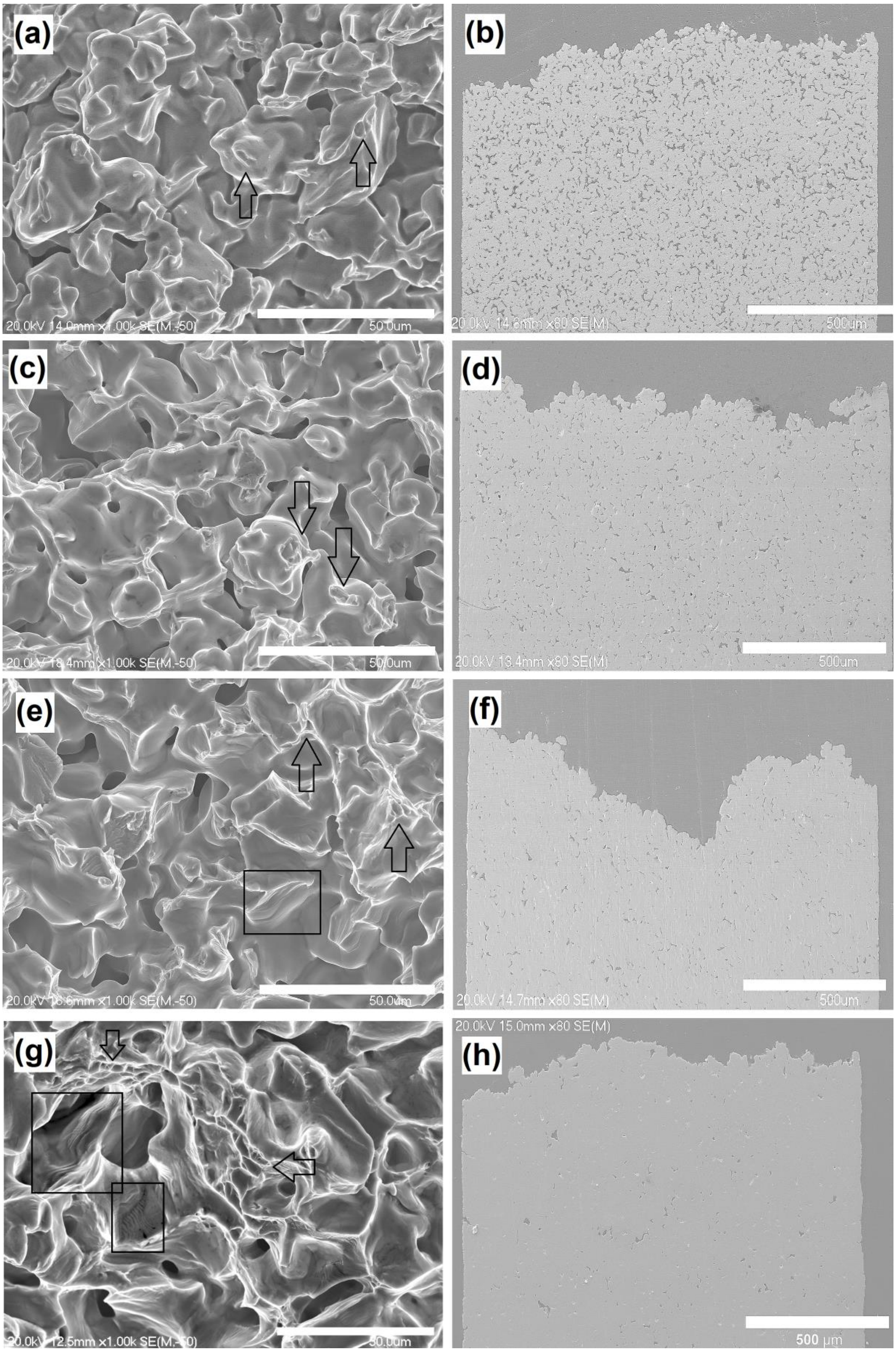

Figure 5-11 Fracture surfaces, from test pieces with varying amounts of porosity, examined by SEM; (a) (b) 29.7 vol.%, (c)(d) 21.2 vol.%, (e)(f) 16.4 vol.%, (g) (h)12.3 vol.%. The fracture necks are pointed out by the arrows and the slip planes are outlined by the rectangular boxes.

5.2.7 Pore Shape Analysis

Pore shape analysis was performed at different locations on the fractured tensile samples from the porous Ti as outlined in Figure 5-12. Point 1 is at the fractured tip of a tensile specimen, point 2 is at the end of the shoulder of the tensile specimen, and point 3 is at the end of the grip section. Two porosity levels were selected, 29.7 vol.% and 12.3 vol.%, respectively. In addition, an analysis was also done for comparison on as-sintered samples that had not been tensile tested. In Figure 5-13(a), at point 1 and point 2, the pore shape factor distributions were comparable; the pore shape factor distribution at point 3 and in the as-sintered sample was similar. Points 1 and 2 have more irregular pores compared with point 3 and pores found in the as-sintered samples. This is because points 1 and 2 have been subjected to more severe tensile loading and point 3 to the least tensile loading. As the porosity was decreased to 12.3 vol.% (Figure 5-13(b)), and although there were four different pore shape factor distributions, points 1 and 2 still showed more irregular pores than point 3 and those in the as-sintered sample. By comparing the pore shape factor of as-sintered samples in Figure 5-13(a) and (b), as expected, the higher porosity level of porous Ti compacts had more irregular pores than the lower porosity ones. Under tension, the pores in lower porosity compacts are opened up to form irregular pores. To some extent, the lower value of pore shape factor also indicates an elongated pore, since a long rectangular shape would give a low value for the shape factor parameters according to Equation (3-4). In other words, spherical pores are being stretched in tension to an elongated shape and cracks are propagated through the pores, which are acting as linkage sites.

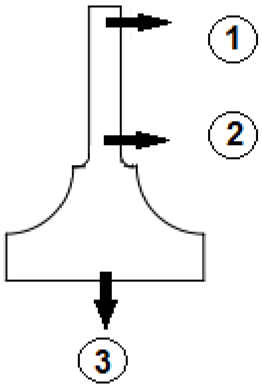

Figure 5-12 Locations taken in a fractured tensile specimen for image analysis.

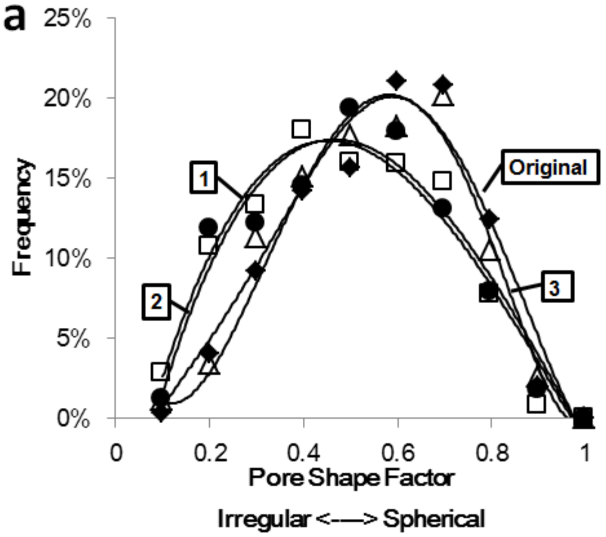

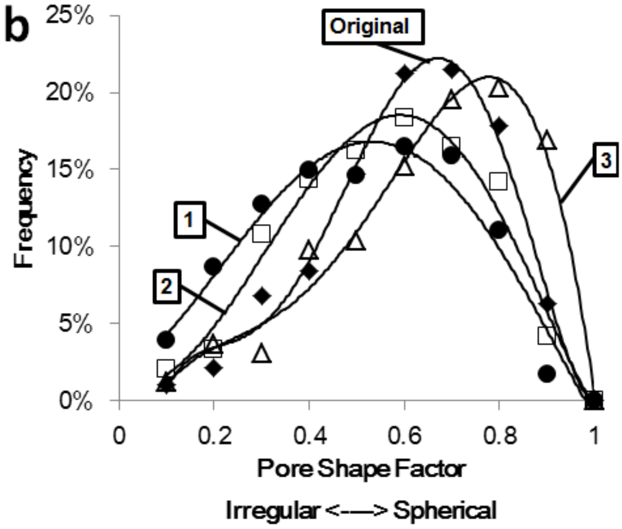

Figure 5-13 Pore shape factor distributions of two porous Ti compacts: (a) 29.7 vol.% porosity, (b) 12.3 vol.% porosity.

5.2.8 Tensile Fracture Model for Porous Materials

Based on the results shown above, a fracture model for sintered porous metal materials under tensile loading is proposed in Figure 5-14, assuming spherical powder particles. The mechanical behaviour of porous materials at two different porosity levels has been illustrated. At high porosity levels, the strength and ductility of the material relies on the necking between particles, due to the small amount of densification. At this stage, the pore shape is irregular. As the densification process develops further, the pores become rounder and the porosity level decreases significantly so that the strength and ductility of a material is increased. In this case, the loading stretches the spherical pores first to produce more irregular pores. Tiny pores are then generated to form a dimple fracture surface in the materials under the tension force. As a result, the pores grow and the cracks propagate through the pores causing the failure.

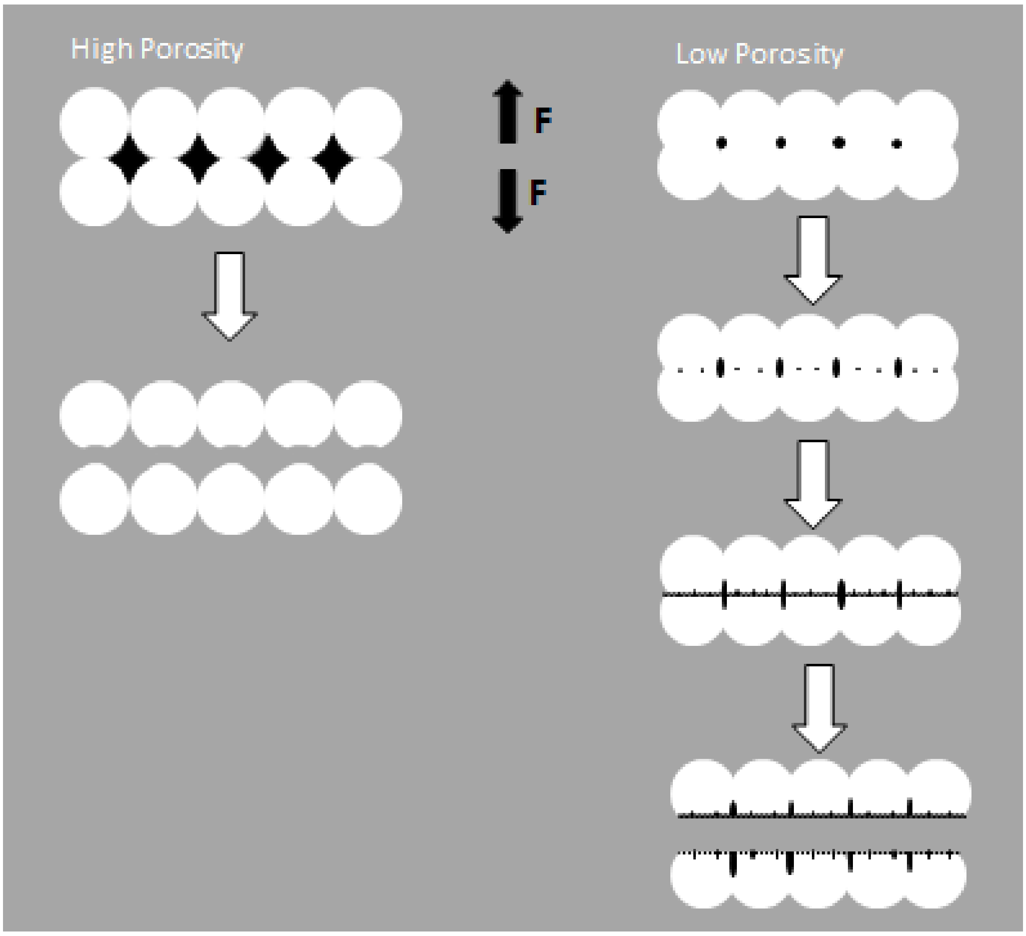

Figure 5-14 Tensile fracture models for porous materials.

5.3 Conclusions

This chapter has systematically investigated the effect of the pore volume fraction on the pore interconnectivity, mechanical behaviour and pore size and shape of Ti compacts prepared by slip casting. The following conclusions can be made:

- By using Taguchi's method, it was found that sintering temperature has the most significant effect on the total porosity level of compacts, followed by the sintering time. A confirmation test was undertaken, which showed that the experimental results fell within a 90% confidence interval of the predicted result.
- Decreasing porosity resulted in a linear reduction in the amount of open porosity and a linear reduction in permeability. A slip casting process for making porous Ti showed a moderate fraction of open pores compared with a press and sintering route and a gel-casting route.
- A novel way of observing the degree of interconnected porosity using ammonium meta-tungstate solution was presented, which proved to be an effective approach.
- A linear relationship existed between tensile strength and the degree of porosity in compacts. The Haynes's model gave a good data fit; the pore geometry and interaction of stress concentrations should be considered.
- The relative ductility of porous Ti compacts produced by slip casting was comparable with porous Ti compacts produced by a press and sintering route. Haynes's model produced a good prediction of the relative ductility to porosity relationship. It showed the value of constant (C) in Haynes's model would be affected by the ability of Ti to strain harden and that interstitial oxygen was the main cause.
- The pore size in the sintered Ti compacts decreased with decreasing level of porosity. Lower porosity compacts gave more spherical pores and higher porosity compacts gave more irregular pores. When subject to tensile loading, the spherical pores opened up to form irregular pores.
- The tensile fracture models of porous Ti compacts have been illustrated, for material with both high and low porosity levels and spherical powder particles. Ti compacts with high levels of porosity fail in a brittle manner. However, in those with low porosity, the tensile forces lengthen the spherical

pores to irregular and/or elongated shapes, which then act as linkage sites and allow cracks to propagate through the material and cause failure.

6. Chapter 6 – Study of Ti compacts with controllable porosity by slip casting of binary powder mixtures

6.1 Introduction

The effect of the particle size distribution on packing and sintering behaviour of compacts have been described in a number of publications [28, 148, 160]. Tari [74] found the coarse alumina powder particles with a bimodal particle size distribution near to that predicted by the Furnas model gave a highest particle packing density in the slip casting process. However, adding fine alumina powder particles into this type of coarse powder particles lowers the particle packing density. No further sintering process was undertaken in this study to present the final properties, in terms of sintered density, mechanical properties, etc. Smith and Messing [111] investigated the green density and sintered density for a mixture of 5μm and 0.5μm alumina powder by using the press and sinter method. The highest sintered density occurs with the 100% fine powder particles, even though it showed the lowest green packing density. This is because when the small particles constitute the bulk of the structure, large particles generate stresses that inhibit densification [28].

Robertson and Schaffer [161] have summarised some general observations applicable to Ti powder; firstly, for a bimodal powder mixture, the maximum green packing density in which the fine particles occupy the cavities between the coarse particles, occurs when the powder mixture contains 20-30 vol.% of fine particle mixed with coarser particles an order of magnitude larger in size; secondly, the higher driving force from the finer particles leads to an increased sintered density and this usually increases monotonically as the content of fine particles increases.

The advantages of using coarse powder particles in the processing include low materials cost and limited sintering shrinkage. In particular, previous investigations on the slip casting of Ti powder used pure fine HDH powder particles with an average powder particles size of 14 μm (Chapters 4 & 5). In this chapter, it is of interest to study the influence of particle size distribution on the slip casting of Ti powder, with regard to the green packing density, porosity, permeability, microstructure and mechanical properties. By understanding these properties, a slip casting compact, with a porosity level gradient, was also designed.

Ti powder with two powder particle sizes was used for the work presented in this chapter. The coarse powder particles had an average size of 56 µm and the fine powder particles have an average size of 14 µm. The slurries were prepared by mixing these two types of Ti powder at different volume fractions. In this case, it is difficult to obtain a stable slurry made from pure coarse powder particles because of the fast sedimentation rate caused by the gravity forces. Therefore, this study did not investigate a slip cast compact composed of pure coarse powder particles. Green packing density was first measured on fully dried slip casting compacts, to find out their packing density. Three different sintering temperatures were investigated, 1000^{o}C, 1100^{o}C and 1200^{o}C. Upon sintering, the total porosity level, open porosity level, permeability, pore diameter and tensile properties were examined. The microstructures and fracture surfaces were also characterised.

6.2 Results

6.2.1 Particle size distribution

The slip casting process requires stable slurries. In a bimodal powder where there is an unstable suspension, because of the gravity force, large powder particles tend to form a sediment at the bottom more quickly than small powder particles. This results in a powder compact microstructure with a porosity gradient and uneven shrinkage after sintering. To ensure the homogeneity of the slip cast Ti compacts, the particle size distribution in green slip cast rectangular bars (100 × 20 × 10mm^3) were measured from top to bottom, as shown in Figure 3-7. In Figure 6-1, the particles size at d(0.1), d(0.5) and d(0.9) are presented. It can be seen that as the proportion of fine powder particles increased, the average particle size in the slip cast compacts gradually decreased. The particle sizes from the top to the bottom of a compact were reasonably consistent. These results indicated that all of the slip cast Ti compacts had homogeneous microstructures along the length of the samples and so were assumed to produce sintered compacts also with homogeneous microstructures.

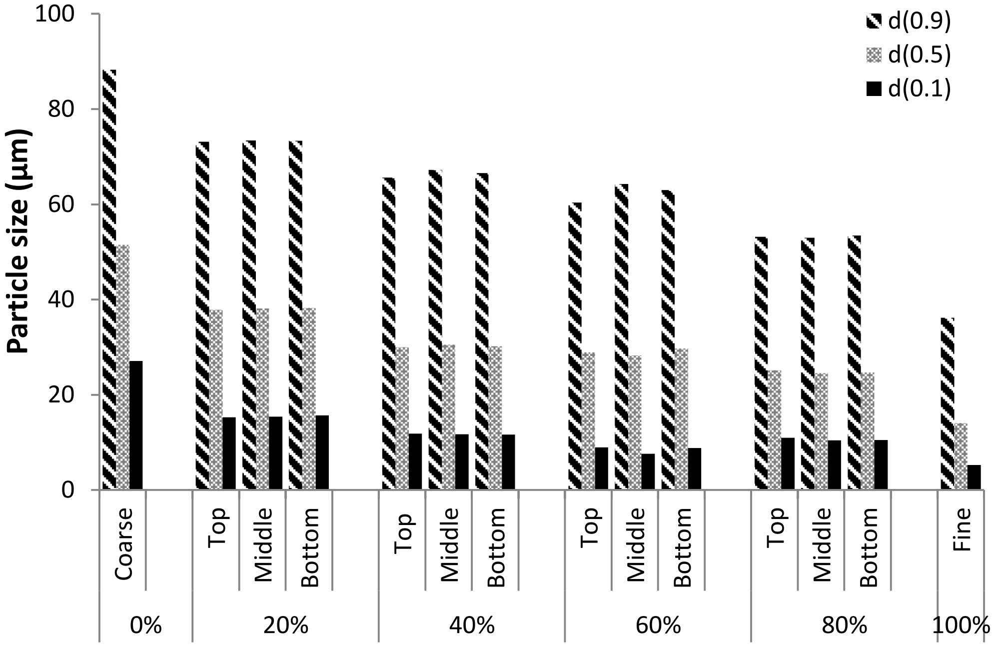

Figure 6-1 Particles size distribution of the slip casting compact made from a bimodal powder mixture.

6.2.2 Packing density

The relative green packing densities of slip cast compacts were measured as a function of fine powder composition, as illustrated in Figure 6-2. It can be seen that a green compact made from 100 vol.% of fine powders (V_f) has the lowest green packing density (46%). However, the relative packing density as a function of volume fraction of fine powder particles fluctuated and no clear trend was observed (Figure 6-2(a)). The packing behaviour of a bimodal powder mixture was first computed by Furnas [105]. This is based on a fine distribution of particles in the interstices of larger particles for reducing the porosity. The calculation of an ideal packing density assumes that the size ratio of coarse particles to fine particles is infinitely large. Subsequent studies on the particle size ratios have shown that the experimental values deviate significantly from the theoretical values predicted by Furnas [103]. Based on Furnas's equation (2-1) to predict the maximum packing density of a bimodal mixture, from Figure 6-2(b), using the data labelled (a) in Figure 6-2, the packing density of coarse particles, V_c is 48% and that of the fine particles, V_f is 46%, then, V_{max} obtained is 72%.

Zheng et al. [102] proposed an improved equation to describe the packing density as a function of the initial packing efficiencies of particles, the particle size ratio, and the volume fraction variations of the system, as shown in equation (2-2). However, this model has a better fit with mono-sized particles and when the packing efficiencies for both coarse and fine particles are the same. By fitting Zheng's model with the experimental conditions, the curve showed a steady increase in relative packing density as the volume fraction of fine powder increased to 0.35 and reached a peak packing density value (55%) at this volume fraction. This was followed by a gradual decrease to 46% as the volume fraction of fine powder increased further, as shown by the data labelled (b) in Figure 6-2. However, there was no well-defined maximum green density in the experimental results.

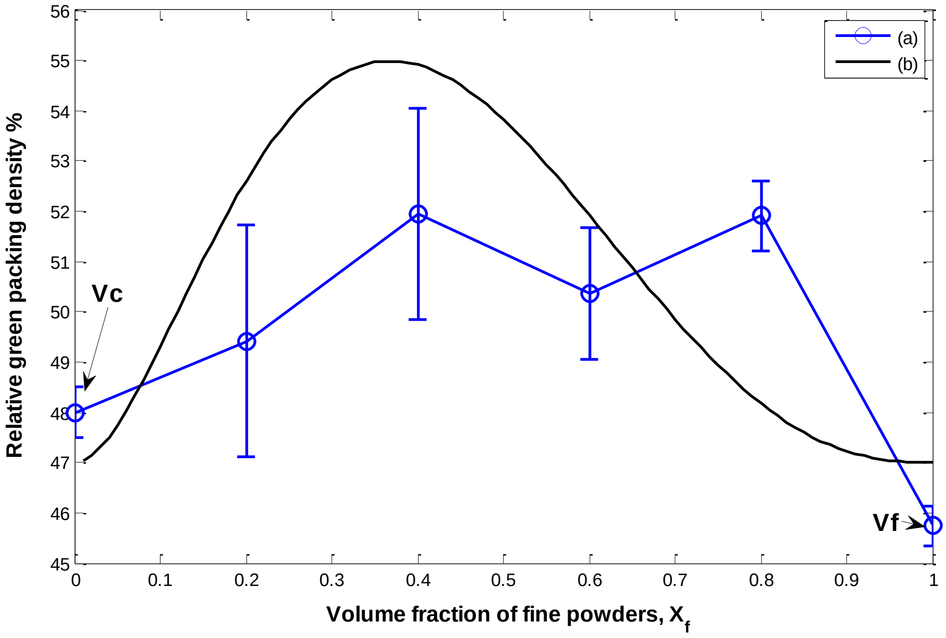

Figure 6-2 Plot of green packing density of Ti compacts as a function of fine powder composition; (a) Zheng's model; (b) Experimental data.

6.2.3 Porosity, open porosity & gas permeability

The total porosity levels in sintered slip cast compacts were investigated for three different sintering temperatures, 1000°C, 1100°C and 1200°C (Figure 6-3). Due to the difficulty of obtaining a slip cast compact made from 100 vol.% of coarse powder particles, those compacts were not taken into account in the results which follow. As the sintering temperature increased from 1000°C to 1200°C, the total porosity level decreased from 30 vol.% on average to less than 20 vol.%. In the meantime, at each sintering temperature, the total porosity level also decreased gradually as the volume fraction of fine powder particles increased. The most loosely packed green powder structure was produced using 100% of fine powder particles and this gave a relatively low sintered porosity level.

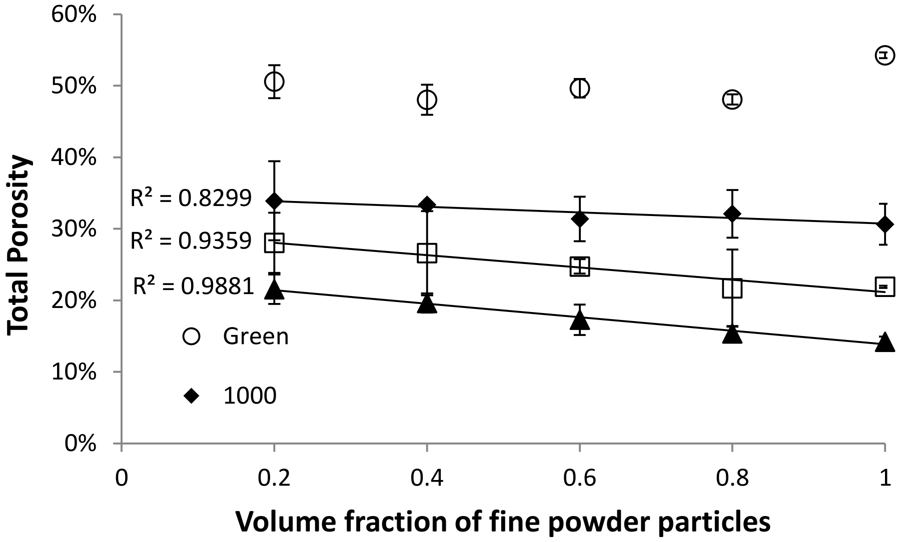

Figure 6-3 Plot of total porosity level of sintered slip casting compacts at 1000°C, 1100°C and 1200°C, respectively, as a function of volume fraction of fine powder particles.

The gas permeability of Ti compacts composed of different volume fraction of fine powder particles (from 20 vol.% to 100 vol.%) and sintered at three different temperatures (1000°C, 1100°C & 1200°C) were also investigated. Exponential decay curves could be fitted to the data for permeability and the volume fraction of fine powder particles (Figure 6-4). In particular, as the sintering temperature increased from 1000°C to 1200°C, the constants for the best fit equations decreased from 0.4974 to 0.0723. This is because an increase in the sintering temperature resulted in a decrease in the amount of open porosity level.

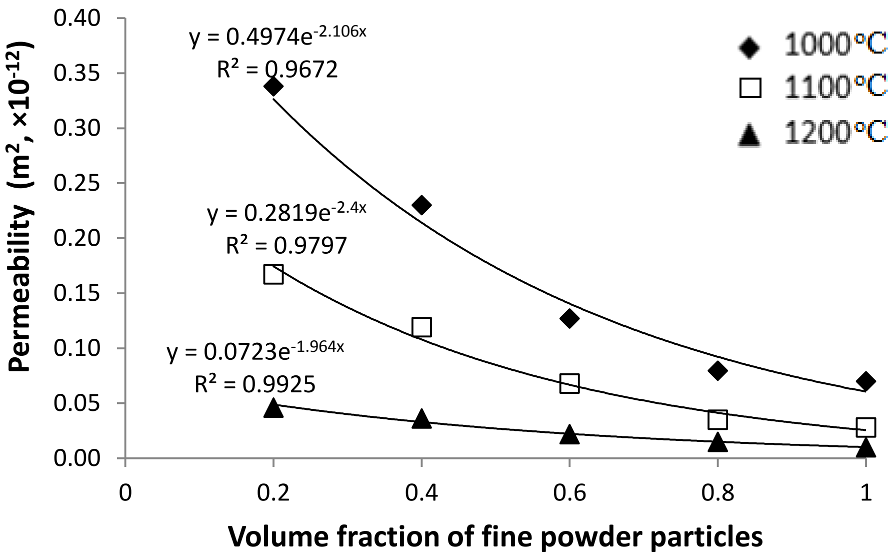

Figure 6-4 A plot of gas permeability of sintered Ti compacts as a function of volume fraction of fine powder particles.

The open porosity and the gas permeability of sintered compacts as a function of the total porosity are plotted in Figure 6-5. A strong positive linear relationship exists (dashed line in Figure 6-5) between the amount of open porosity and the total porosity (this includes closed porosity and open porosity). On the other hand, there is no strong correlation between the gas permeability and the total porosity. However, when the data points were grouped into three different sintering temperatures, at 1100°C and 1200°C, the value of R^2 is quite high indicating a very strong correlation; but at 1000°C, the value of R^2 dropped slightly indicating a moderately strong correlation, as shown by the solid lines in Figure 6-5.

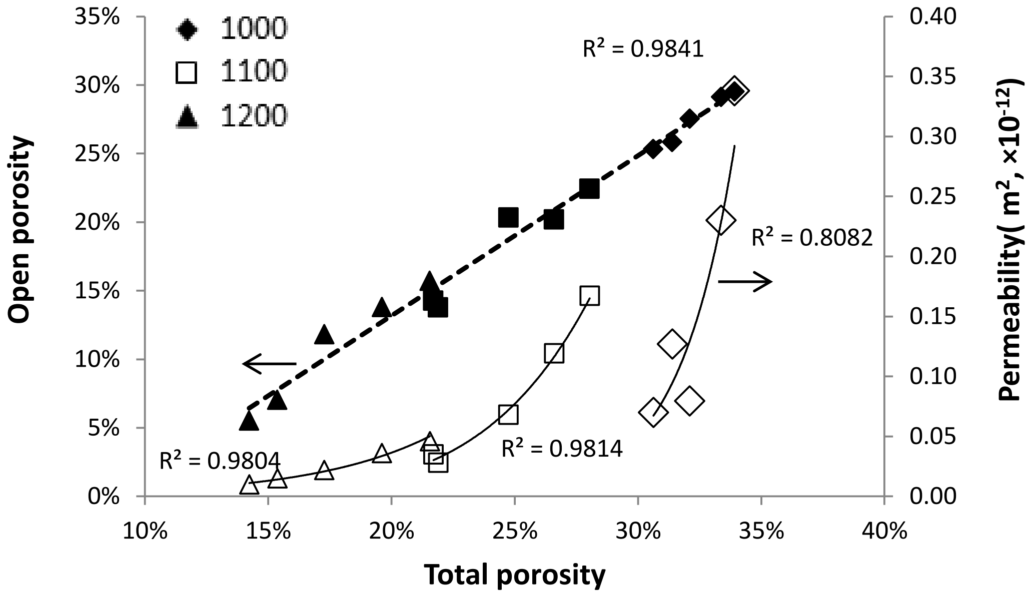

Figure 6-5 A plot of open porosity and gas permeability for sintered Ti compacts as a function of total porosity level. The data for open porosity are shown by the filled points and the data for permeability are the unfilled points.

6.2.4 Microstructural analysis and pore diameter

Optical micrographs of sintered Ti compacts are shown in Figure 6-6. Nine sintered Ti compacts made from different compositions of fine powder particles (20 vol.%, 60 vol.% & 100 vol.%) with different sintering temperatures (1000°C, 1100°C & 1200°C) were selected for comparison. In Figure 6-6, the micrographs are arranged so that each row is for a different composition of fine powders and each column is for a different sintering temperature. Image analysis was used to determine the change in average pore diameter with changes in volume fraction of fine powder particles and sintering temperature. The average pore diameter as a function of porosity is summarised in Figure 6-7.

It can be seen that an increase in sintering temperature and in the volume fraction of fine powder particles reduces the pore size. At 1000°C, the pores shown in the micrographs in the first column are irregularly shaped (Figure 6-6 (a), (d) & (g)). The average pore size decreased from 10.2 μm to 8.3 μm as the fine powder particle content increased from 20 vol.% to 100 vol.%. The pores were formed between the powder particle contact points. At a higher sintering temperature of 1100°C (Figure 6-6 (b), (e) & (h)), the average pore size was reduced from 9.8 μm to 7.4 μm as the amount of fine powder particles increased from 20 vol.% to 100 vol.%. The pores were mainly located at the grain boundaries. At 1200°C (Figure 6-6 (c), (f) & (i)), the microstructures showed that densification had occurred. The shape of the pores became rounder in the Ti compact made from 100 vol.% of fine powder particles. The average pore size decreased from 8.3 μm to 6.5 μm as the amount of fine powder particles increased from 20 vol.% to 100 vol.%. Some intra-granular pores can be observed due to exaggerated grain growth.

At 1000°C, the grain size in the compact made from 20 vol.% of fine powder particles is larger than that in the compact made from 100 vol.% of fine powder particles. As the sintering temperature increased to 1100°C, the grain size in all three compacts increased slightly, but the smallest grain size was found in the compact made from 100 vol.% of fine powder particles. When the sintering temperature was 1200°C, the grain sizes in the compacts were similar. The rate of grain growth in the compact with 100 vol.% of fine powder compact is more rapid than that in the other compacts with a smaller amount of fine powder particles.

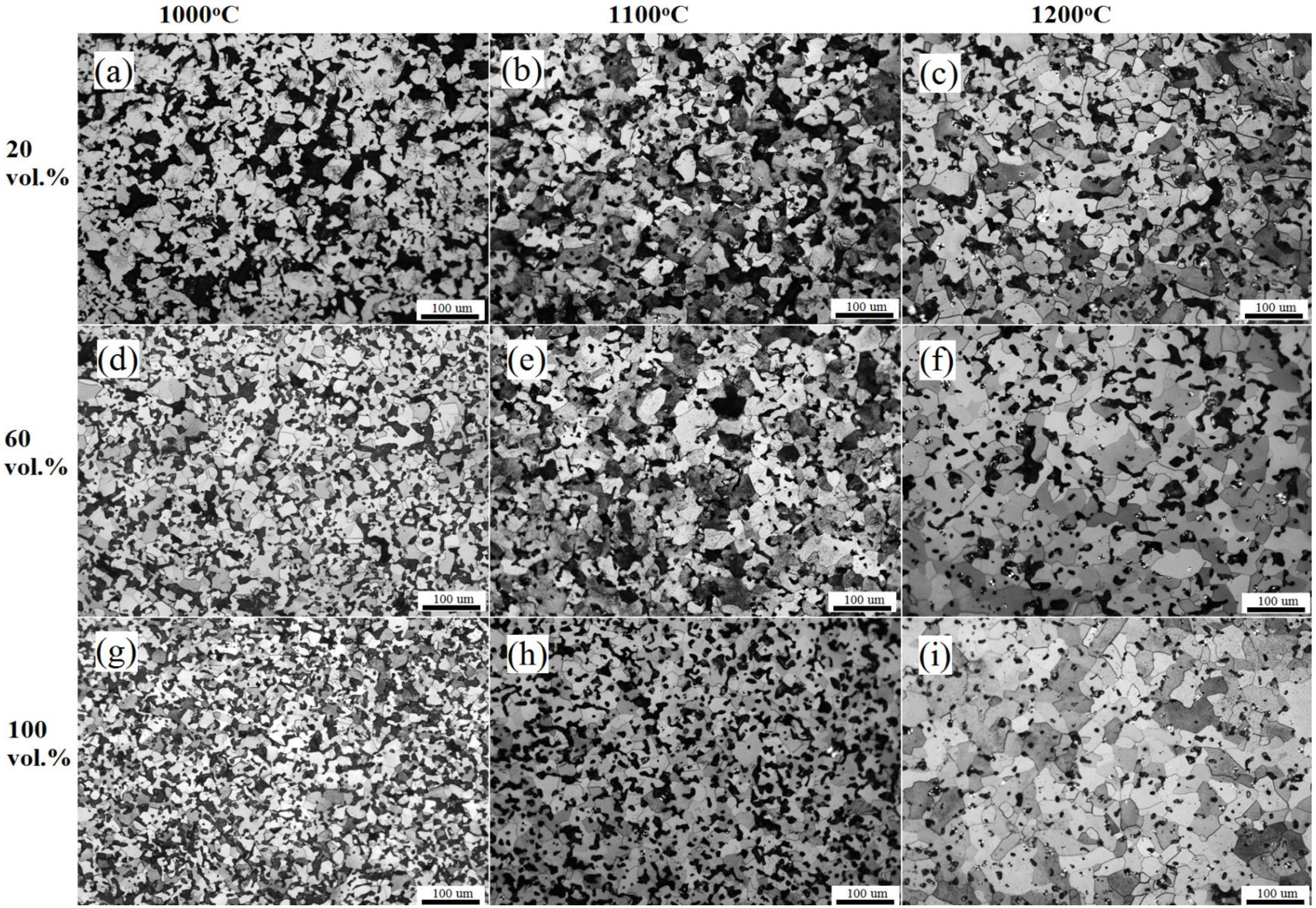

Figure 6-6 Optical microscopy images of sintered Ti compacts; (a) (b) (c) Ti compact composed of 20 vol.% of fine powder; (d)(e)(f) Ti compact composed of 60 vol.% of fine powder; (g)(h)(i) Ti compact composed of 100 vol.% of fine powder.

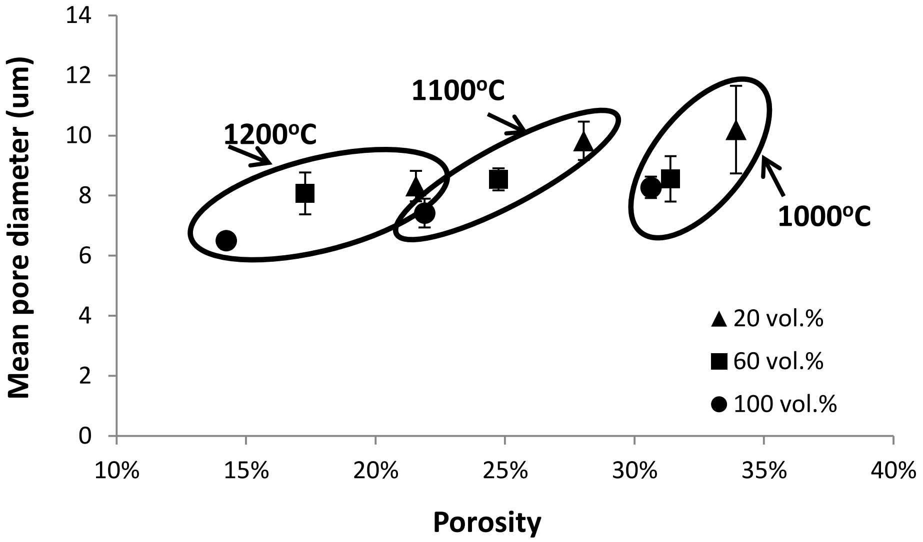

Figure 6-7 Image analysis of the mean pore diameter from optical micrographs of sintered samples.

6.2.5 Tensile Properties

6.2.5.1 Analysis of oxygen and carbon content

Interstitial elements, such as oxygen and carbon, could affect the mechanical behaviour of Ti [133]. In this case, to ensure that differences in mechanical behaviour of the different sintered Ti compacts was because of processing variables and not influenced by differences in the amounts of residual oxygen and carbon. Compacts containing 20 vol.% and 100 vol.% of fine powder particles and sintered at the three different temperatures were analysed for oxygen and carbon content. The results are summarised in Table 6-1. The oxygen and carbon contents in the sintered Ti were reasonably consistent. Therefore, the influence of variations in the oxygen and carbon on the mechanical properties of sintered Ti should be minimal.

Table 6-1 Oxygen and carbon content in the sintered Ti compacts prepared by respective 20 vol.% and 100 vo.% of fine powder particles.

Sintering temperatures (°C)	Oxygen content		Carbon content	
	20 vol.%	100 vol.%	20 vol.%	100 vol.%
1000	0.43	0.48 wt.%	0.042	0.051 wt.%
1100	0.40	0.44 wt.%	0.053	0.043 wt.%
1200	0.45	0.43 wt.%	0.047	0.046 wt.%

6.2.5.2 Tensile strength

The data in Figure 6-8 shows that the fracture stress increases with both an increase in sintering temperature and an increase in the volume fraction of fine powder particles. A compact containing 20 vol% of fine powder particles and sintered at 1000 ^{o}C had a tensile fracture stress of 160 MPa. This increased to 533 MPa when the sintering temperature was increased to 1200^{o}C and the compact consisted of 100 vol% of fine powder. There is a positive linear relationship between the tensile fracture stress and the volume fraction of fine powder particles. As shown in Figure 6-3, there is a negative linear relationship between the total porosity level and the volume fraction of fine powder particles. In other words, the total porosity level in a sintered Ti compact governs the magnitude of the tensile fracture strength. The data in Figure 6-9 shows the relationship between the total porosity and the tensile fracture stress. A strong negative linear relationship exists between these two variables. From Figure 6-8, the Ti compact made using 100 vol.% of fine powder particles and sintered at 1000^{o}C showed a tensile fracture stress comparable with the compacts made with 20 vol.%, 40 vol.% or 60 vol.% of fine powder particles and sintered at 1100^{o}C. However, from Figure 6-9, it can be seen that these four compacts have different levels of porosity ranging from 24 vol.% to 30 vol.%. Also, compacts made with 100 vol.% of fine powder particles and sintered at 1100 ^{o}C have a similar tensile fracture stress to those compacts containing 20 vol.% or 40 vol.% of fine powder particles and sintered at 1200^{o}C. These are shown within the rectangular boxes in Figure 6-9.

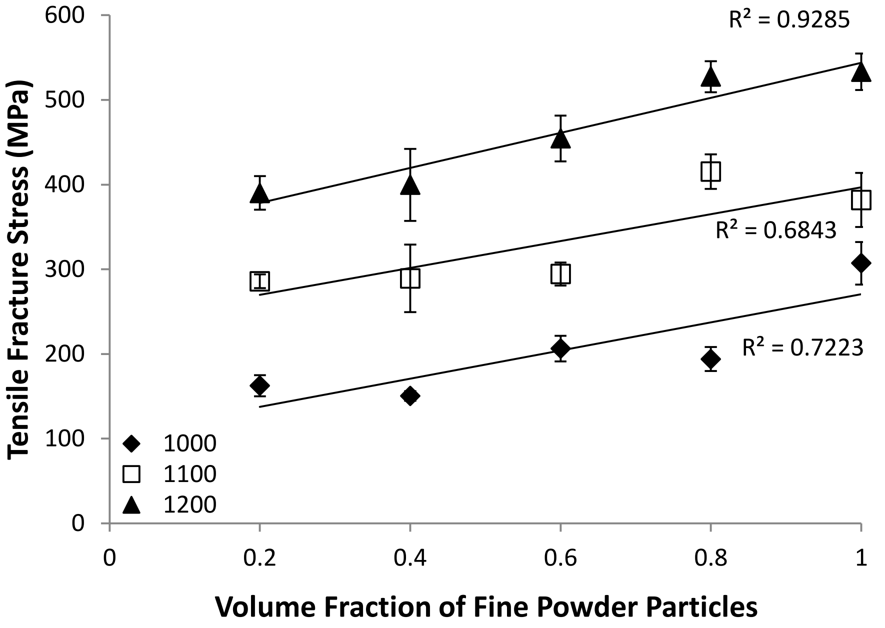

Figure 6-8 Plot of tensile fracture stress of sintered Ti compacts as a function of volume fraction of fine powder particles.

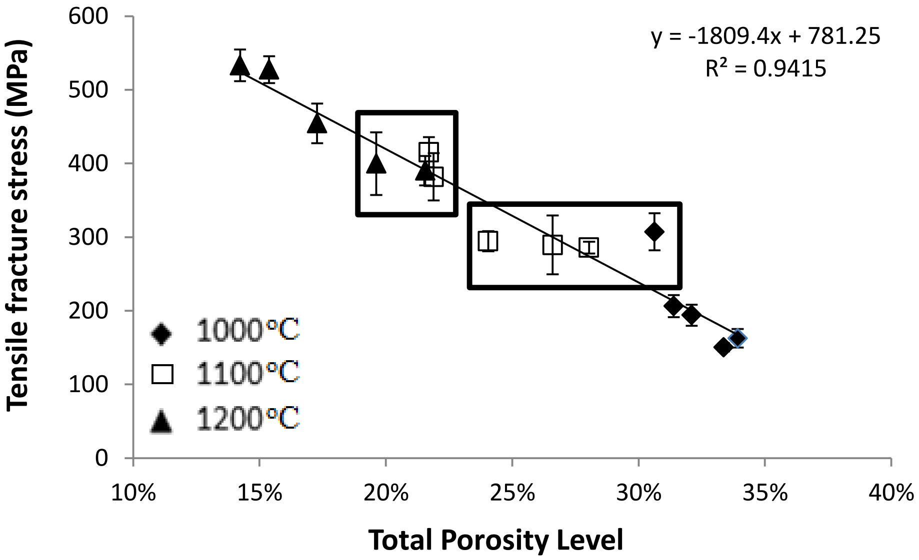

Figure 6-9 Plot of tensile fracture stress of sintered Ti compacts as a function of total porosity level. The boxes outlined the compacts with similar tensile fractures stresses but different levels of porosity.

6.2.5.3 Elongation

The relationship between the elongation to fracture of sintered Ti compacts and the volume fraction of fine powder particles is shown in Figure 6-10. After sintering at 1000°C, the elongation to fracture increases very slightly, from 1.4% to 2.0%, as the fine powder particles content of a compact increases. When sintered at 1100°C, the elongation to fracture is more variable as the amount of fine powder particles increases. A Ti compact made using 100 vol.% of fine powder and sintered at 1100°C would be expected to give the highest elongation to fracture, compared with other compacts sintered at the same temperature. However, the elongation to fracture was relatively small (3.0%) and lower than the elongation values for compacts made using 60 vol.% or 80 vol.% of fine powder particles. When the sintering temperature is 1200°C, there is a slightly stronger exponential relationship between the elongation and the volume fraction of fine powder particles. A significant increase in elongation, from 4.1% to 10.0%, can be seen as the volume fraction of fine powder particles increases from 20 vol.% to 100 vol.%. A strong exponential relationship between the total porosity level and the elongation to fracture is shown in Figure 6-11. This indicates that the total porosity level in a sintered Ti compact has a major influence on the elongation to fracture.

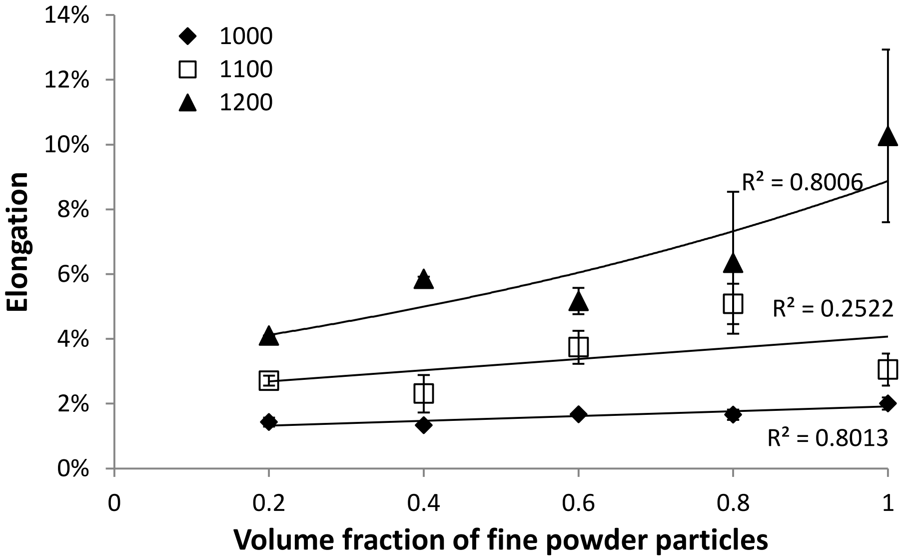

Figure 6-10 A plot of elongation of sintered Ti compacts as a function of volume fraction of fine powder particles.

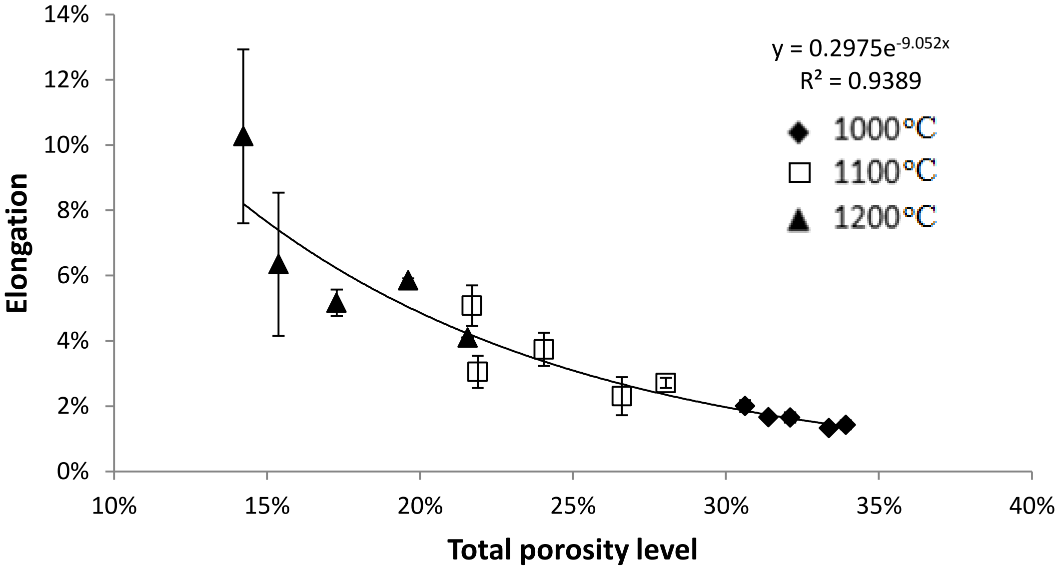

Figure 6-11 A plot of elongation of sintered Ti compacts as a function of total porosity level.

6.2.6 Young's Modulus

The relationship between Young's modulus and the volume fraction of fine powder particles sintered at different temperatures is shown in Figure 6-12. However, the R^2 values at 1000^oC and 1100^oC are only 0.0161 and 0.2639, respectively, which indicate a scatter of variation in the data. At 1200^oC, the R^2 value is 0.822, which shows a moderately strong relationship between the volume fraction of the fine powder particle and Young's modulus.

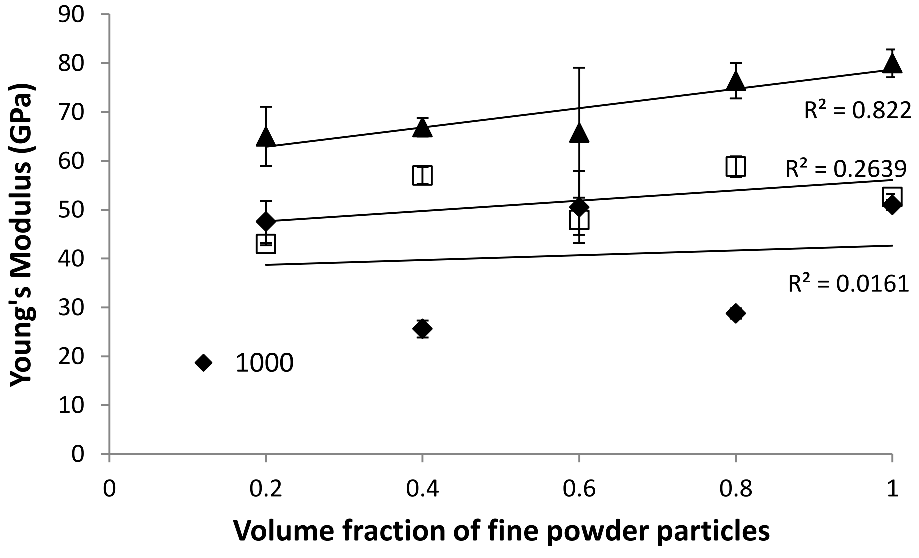

Figure 6-12 A plot of Young's modulus of sintered Ti compacts as a function of volume fraction of fine powder particles.

In Figure 6-13, the Young's modulus of the porous Ti compacts is plotted against the total porosity level. A linear best fit line is presented in the graph. It is clear that at a total porosity level less than 22 vol.%, the Young's modulus values are close to the best fit line; whereas at a total porosity level of more than 22 vol.%, the data points show more scatter. This might be because of increased brittleness at higher porosities and therefore more variation is to be expected.

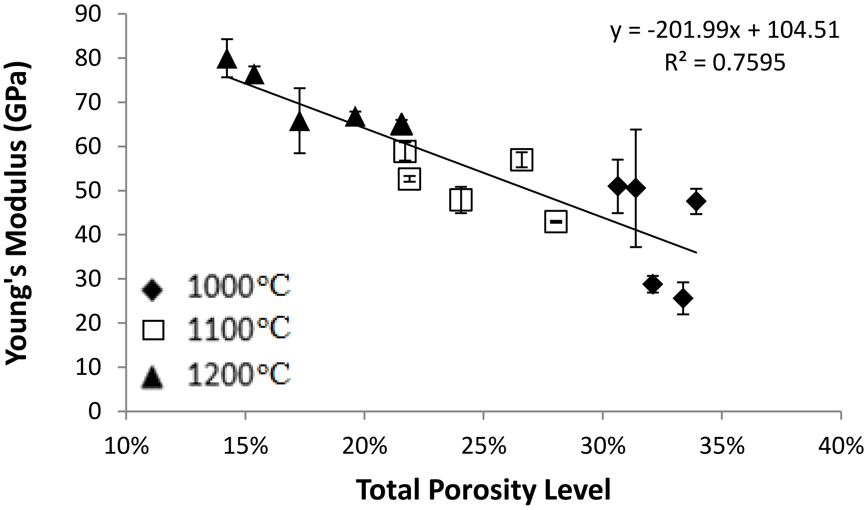

Figure 6-13 A plot of elongation of sintered Ti compacts as a function of total porosity level.

6.2.7 Fracture Surface

The tensile fracture surfaces of sintered Ti compacts composed of 20 vol.%, 60 vol.% and 100 vol.% were compared in Figure 6-14. Figure 6-14(a) shows that the fracture surface, after sintering at 1000°C, contains porosity and necked regions that are limited to the contact points between the particles. Figure 6-14(d) also shows a porous fracture surface with evidence of brittle cleavage, as outlined in the rectangular box. For the compact made using 100 vol.% of fine powder particles and sintered at 1000°C (Figure 6-14 (g)), there is a less porous fracture surface compared with the previous two figures. At this stage, due to the low sintering temperature, the pores were interconnected and irregular in shape, created by the initial packing structure of the sintered powder particles. As the sintering temperature increased to 1100°C, the fracture surfaces of the compacts showed a more densified microstructure in which some of the pores become round (Figure 6-14 (b), (e) & (h)). At 1200°C, the ductile features, microvoids, can be found in the fracture surface of the compacts, as pointed out by the arrows (Figure 6-14 (c), (f) & (i)). In particular, the compact made from 100 vol.% of fine powder showed the densest microstructure (Figure 6-14 (i)).

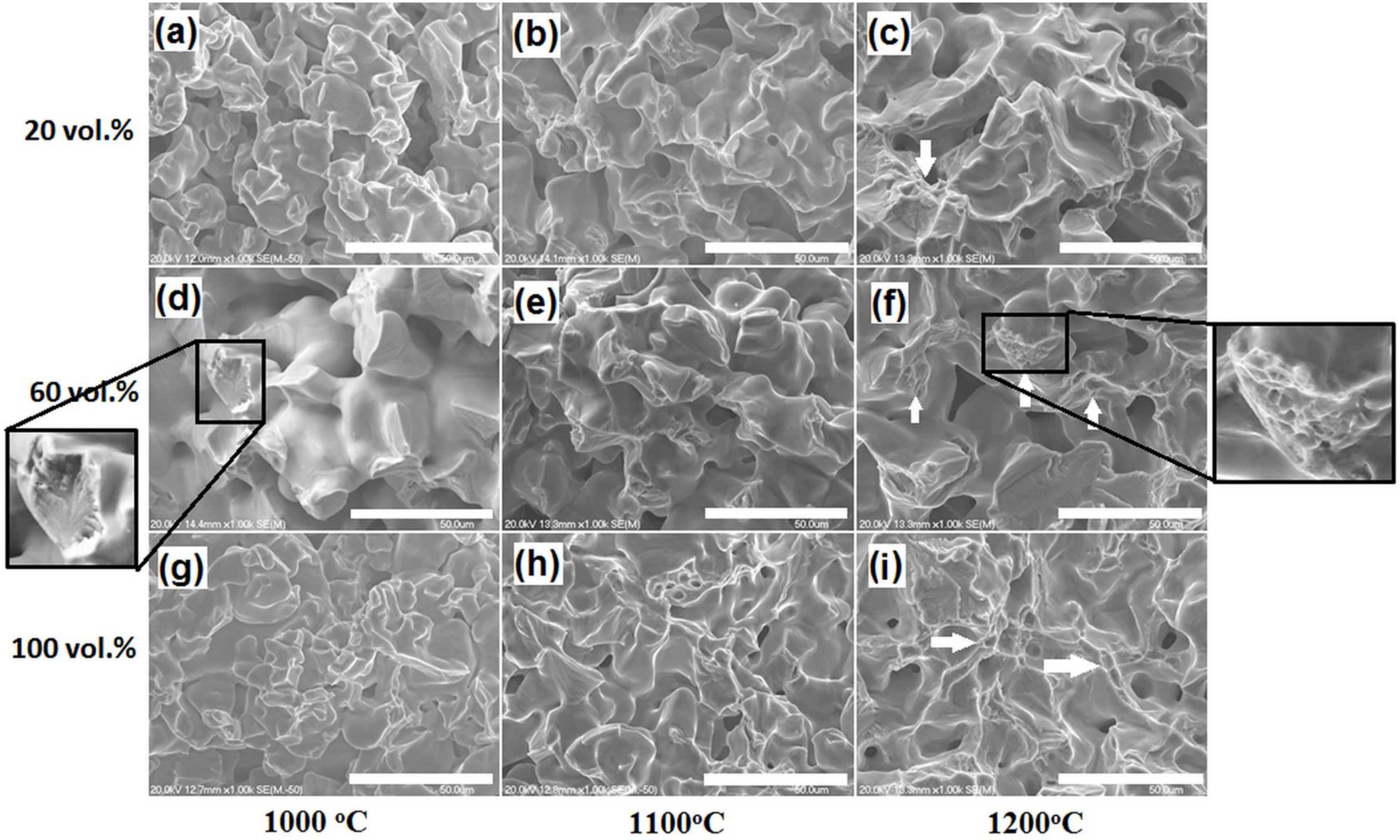

Figure 6-14 fracture surface of sintered Ti compacts examined by SEM; (a) (b) (c) Ti compact composed of 20 vol.% of fine powder; (d)(e)(f) Ti compact composed of 60 vol.% of fine powder; (g)(h)(i) Ti compact composed of 100 vol.% of fine powder.

6.3 Discussion

6.3.1 Packing density

The experimental data of relative packing density as a function of volume fraction of fine powder particles were compared with Zheng's theoretical model shown in Figure 6-2. By fitting with the experimental values of V_f and V_C, Zheng's model gave a maximum packing density of 55% at 0.35 volume fraction of fine powder particles. Nevertheless, from the experimental data, by taking account of error bars, the compacts made using between 0.4 and 0.8 volume fractions of fine powder showed similar levels of relative packing densities. There is no well-defined maximum green packing density. Zheng's model is based on two assumptions. One is that the particle shape is spherical and the other is that the initial packing densities of both coarse and fine powder particles are equal. The irregularly shaped hydride-dehydride particles make it impossible to place the right particle in the right inclusion. As investigated by Smith and Midha [162], an increase in particle irregularity results in a decrease of green packing density. Furthermore, the space between the coarse powder particles may not be completely filled by the fine powder particles. Karlsson and Spring [163] studied the packing behaviour of irregular particles and found that the accuracy of Furnas's model can be improved by considering the volume expansion that takes place when mixing coarse and fine powder particles. In this case, because the volume of a slip casting compact is constrained by the plaster mould, the relative packing density may fluctuate slightly when the volume fraction of fine powder is between 0.4 and 0.8. Therefore, in this case, it is difficult to obtain the maximum relative packing density at a specific volume fraction of fine powder particles.

6.3.2 Effect of binary powder system on the properties of slip casting sintered Ti compacts

The increase of the volume fraction of fine powder particles in the as-sintered slip casting Ti compact decreases the porosity level, permeability and pore diameter

(Figure 6-3, Figure 6-4, Figure 6-5 & Figure 6-7). In Figure 6-3, the coefficient of determination R^2 was about 0.83 at 1000^{o}C, and at 1200^{o}C, it increased to 0.99. This indicates that the negative linear relationship between the total porosity level and the volume fraction of fine powder particles becomes stronger as the sintering temperature increases. The sintered porosity level can be governed either by the packing density or sintering shrinkage, depending on the sintering conditions. For a low sintering temperature or a short sintering time, the packing density variation with powder composition is dominant. For a high sintering temperature or a long sintering time, the smallest porosity level occurs at a composition with 100% fine powder particles [28]. This is attributed to the surface energy per unit volume, which depends on the inverse of the particle diameter. In other words, fine powder particles with high specific surface area have higher energy [18]. This allows a compact composed of 100% fine powder particles undergo a faster sintering densification in spite of an initially lower packing density under same sintering conditions.

By using fine powder particles, the microstructures of compacts, after sintering at 1000^{o}C and 1100^{o}C showed finer grains, as illustrated in Figure 6-6. However, when the sintering temperature was increased to 1200^{o}C, all the compacts showed a similar grain size. The grains in the compact made using 100 vol.% of fine powder particles grew more rapidly, indicating that the compact underwent a faster sintering densification. This resulted in similar grain sizes in the compacts sintered at 1200^{o}C. However, as the sintering densification increases further, coarsening occurs, which causes grain growth in the compact (Figure 6-6). The pores are all closed and the pore size increases due to an Ostwald Ripening effect. However, in this case, the pore growth could not be seen because the sintering temperature was not high enough.

6.3.3 The relationship between porosity, permeability and pore diameter

The relationships between the total porosity level, permeability, open porosity and pore diameters were plotted in Figure 6-5 and Figure 6-7. It is interesting to note that the permeability of compacts, made using 100 vol.% of pure HDH Ti powder particles with an average diameter of 14 μm, have a strong linear relationship with the total porosity level in the compacts [164]. However, the permeability results obtained from the binary powder particle mixtures in the present study produce non-linear and weak relationships. The difference may be because the porosity, permeability and pore diameters in the compacts made from 100 vol.% of fine powder are only controlled by the sintering process, whereas the same properties in compacts made from a binary powder mixture are affected by both the powder composition and the sintering process. The combined effects from the powder compositions and the sintering process may control the permeability in a more complicated way. Permeability measures the volumetric flow rate of a fluid through unit area of a porous body for a given pressure gradient [123]. One of the most commonly used equations to describe the relationship between porosity and permeability is the capillary tube model, developed from the Kozeny – Carman equation [118, 119], the Hagen-Poiseuille Law and Darcy's Law, as shown in equation (2-7). This equation is assuming the porous media as a bundle of capillary tubes filled with a non-porous cementing material. From this equation, the permeability is normalised by the average pore diameter squared ($k/\bar{d}^2$) as a function of total porosity level, as plotted in Figure 6-15. The experimental data shows an improved power relationship between the normalised permeability and the total porosity compared with Figure 6-5. In this case, this implies that the capillary tube model can be used to explain the relationship between the permeability, pore diameter and total porosity. Moreover, the shape factor for a pore and the tortuosity are also variables which change with the total porosity level to give a power correlation between the normalised permeability and the total porosity. The tortuosity is expected to range from 1 to more than 2, depending on the shape of the pore channels [165]. Carniglia [166] pointed out that if cylindrical pores truly dominate in a material, its tortuosity factor should lie within the range of 1 to 2. Herein, the meaning of cylindrical pores assumes that the overall mean dimensions for pore volume and surface area are of "cylindrical" form and does not impute cylindricity to each pore.

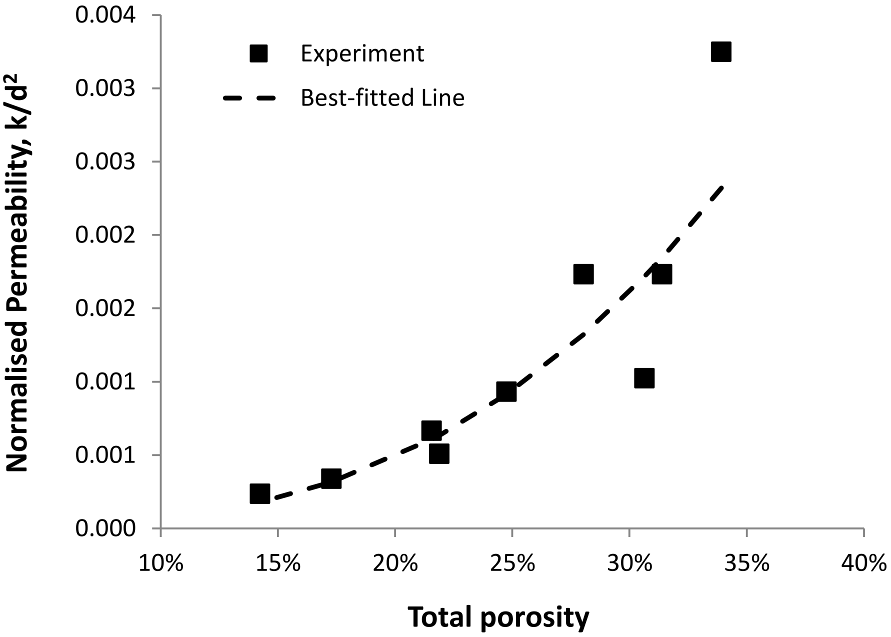

Figure 6-15 A plot of permeability normalised by the average pore diameter squared (d^2) as a function of total porosity level.

In Figure 6-4 and Figure 6-5, the compacts composed of 20 vol.% or 40 vol.% of fine powder particles and sintered at 1100°C showed similar permeability as the compacts composed of more than 60 vol.% of fine powder but sintered at 1000°C. The pore size is also affecting the permeability. To help demonstrating the pore size effect on the permeability, two compacts with different porosity levels and different pore size were illustrated in Figure 6-16. It assumes the pores have same shape factors and the tortuosity factor is 1.

The porosity in compact A is, $P_A = \frac{V_{porosity}}{V_{total}} = \frac{\pi d^2 h}{4V_{compact}}$

The porosity in compact B is, $P_B = \frac{V_{porosity}}{V_{total}} = 16 * \frac{\pi d^2 h}{16 V_{compact}} = \frac{\pi d^2 h}{V_{compact}}$;

so, $P_A / P_B = 1/4$;

Using the capillary tube model as shown in Equation (2-7), it can obtain $\frac{k_A}{k_B} = \frac{P_A}{P_B} * \frac{d^2}{\frac{d^2}{4}} = 1$.

Therefore, although the compact B has more pores than the compact A, the permeability for both compacts are the same, because the compact A has more than twice the pore diameter of the compact B. From this calculation, it gives the reason why some compacts sintered at a higher temperature with less total porosity and open porosity were more permeable than that sintered at a lower temperature with more total porosity and open porosity. Furthermore, it should also be noticed that tortuosity and pore shape factor will also govern the behaviour of permeability. In reality, the increasing sintering temperature will increase the tortuosity in the compact and alter the pore shape. As mentioned before, in chapter 5, the permeability of compacts, made using 100 vol.% of pure HDH Ti powder particles with an average of 14 μm, have a strong linear relationship with the total porosity level in the compacts. In this case, according to the capillary tube model, it implies that the changing of pore diameter, tortuosity and pore shape factor at the same time as the changing of porosity and permeability in order to obtain a linear relationship. This model only applies to the sintered compacts with more than 25 vol.% of porosity. At a lower porosity level, the amount of open pores is limited and the pore size contributing to the permeability would be much smaller.

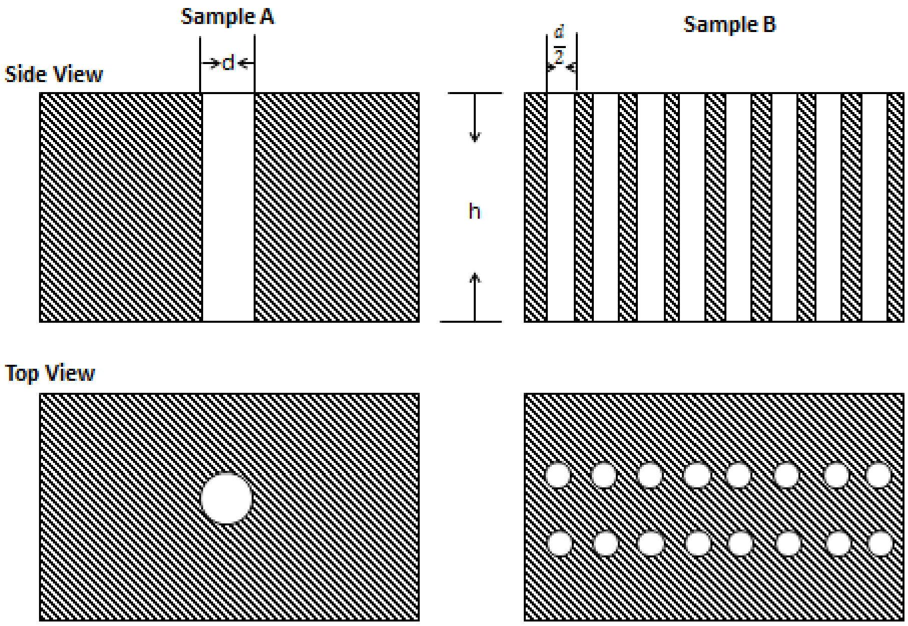

Figure 6-16 An illustration of pore size effect on the permeability of compact.

6.3.4 Tensile properties

From Figure 6-9 & Figure 6-11, it can be seen that the higher tensile properties in porous Ti produced by slip casting are associated with lower porosity levels. It is also interesting to note that in Figure 6-9, the data contained in the boxes indicated that compacts made from 100 vol.% of fine powder particles and sintered at a lower temperature have a comparable tensile fracture stress to other compacts with a lower fine powder particle content and sintered at a higher temperature, as outlined in the boxes. This is because the pore diameter in those compacts made from 100 vol.% of fine powder particles is smaller than that in other compacts, as shown in Figure 6-7. A large pore size leads to a reduction of the effective load bearing area.

By comparing with the tensile properties of Ti compacts made by pure fine HDH powder (-325 mesh), as studied in chapter 5, it shows a reasonable level of similarity, as shown in Figure 6-17. The compositions of the binary powder particle mixture and pore diameter appear to have less effect on the tensile properties of porous Ti compacts than the overall level of porosity. A number of research studies have indicated that porosity is the dominant influence on the mechanical properties of sintered Ti [18, 161, 167-169]. Oh et al. reported results for the compressive and three point bending strength of porous Ti compacts made by a press and sintering route using spherical powder particles with a range of particles sizes [18]. Both proof stress and bending strength increased with decreasing porosity, regardless of processing conditions.

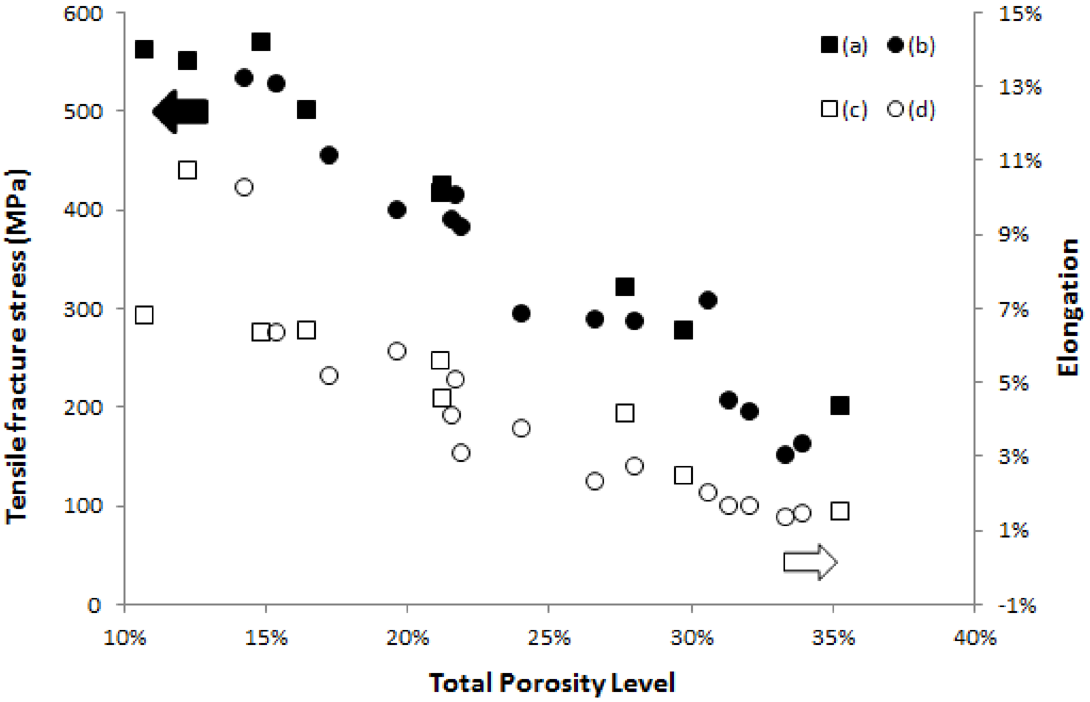

Figure 6-17 A comparison of tensile properties obtained from sintered Ti compacts using a binary powder mixture and pure fine powder particles; (a) tensile fracture stress for a pure fine powder particle composition; (b) tensile fracture stress for a binary powder mixture composition from the present work; (c) elongation to fracture for a pure fine powder particle composition; (d) elongation to fracture for a binary powder mixture composition from the present work.

6.4 Summary

This research has provided a detailed study of the effect of bimodal Ti powder particles on the green packing density, porosity level, pore size, tensile properties and pore interconnectivity of slip cast compacts. The following conclusions can be drawn from this study:

- By mixing coarse and fine Ti powder particles, the green packing density of slip cast compacts showed a slightly loose packed structure when the slip cast compacts were made from pure coarse powder particles or pure fine powder particles. The maximum packing density of a slip cast compact was not observed due to the irregularity of Ti powder particles.
- After sintering, slip cast compacts made using a high content of fine powder particles have a relatively low porosity level, less pore interconnectivity, small pore diameters and high tensile properties. A compact made using 100 vol.% of fine powder particles and sintered at 1000°C and 1100°C showed the smallest grain size. After sintering at 1200°C, because of the higher densification rate, the grain size is similar to that found in other compacts made of using a smaller amount of fine powder particles.
- The open porosity level has a direct linear relationship with the overall porosity level in sintered Ti compacts. However, the permeability showed a non-linear relationship with the porosity level due to differences in pore diameter in the compacts. By using the capillary tube model, a normalised permeability, (the permeability divided by the average pore diameter squared), showed an improved fit with the porosity level.
- The tensile strength of the compacts varied linearly with the porosity level, whereas an exponential relationship existed between the elongation to fracture and the porosity level. A comparison of the tensile properties for compacts made from bimodal powder particle mixtures, with those made

from pure fine powder particles, indicates that the tensile properties of porous Ti compacts are strongly dependent on the porosity level.

7. Chapter 7 – Conclusions and Future Study

7.1 Conclusions

The aim of this work was to develop a novel powder technique to fabricate porous Ti products in a cost efficient way and to investigate the influence of porosity on the properties of sintered Ti compacts. From a review of the literature, it has been found that the slip casting process, as a well-established ceramics process, is rarely being used for metal processing. It was of interest to transfer the ceramics processing technique and adapt it to metal processing and to open up a new area for further research.

Using a slip casting route, porous Ti products have been developed and manufactured. A key step in this study of slip casting was to obtain a stable slurry over a certain time by investigating characteristics of dispersants. Three kinds of dispersants, Dispex N-40, Synthecol SD375 and Dolapix CE64, were studied for their influence on the stability of Ti slips. This study showed that the optimum performance derives from using Dolapix CE64 at 0.3 dw.% and with a pH of 7. Then, a typical formulation suitable for Ti slip casting was invented, which was composed of 77 wt.% Ti powder, 0.8 dw.% binder (PVA), 0.8 dw.% plasticiser (PEG400), 0.3 dw.% dispersant (Dolapix CE64) and the balance being distilled water. Differential thermal analysis and thermogravimetrical analysis were performed on the PVA, PEG400, Dolapix CE64 and a mixture of these organics to investigate their thermal stability, in terms of thermal change and mass loss as a function of increasing temperature (with a constant heating rate). The optimum debinding condition was determined to be at 320^{o}C and with an argon flow rate of 150 mL/min. It was found that the increase in oxygen and carbon content in the slip cast compacts after sintering was reasonably consistent, about 0.15 wt.% and 0.03 wt.% on average, respectively. No TiC and other contaminant phases were detected by XRD. By using this formulation, compacts in the form of rectangular and tubular shapes were fabricated. In addition, large slip cast Ti compacts were made, with a diameter of 120 mm and a thickness of 8 mm, for application in water purification.

By following a successful development of the formulation for Ti slip casting, Taguchi’s method was employed to investigate the sintering behaviour of the slip cast compacts, with regard to sintering temperature (1000°C, 1100°C, 1200°C), sintering time (0.5 h, 1 h & 2 h), heating rate (5°C/min, 7°C/min & 10°C/min) and cooling rate (5°C/min, 10°C/min, F/C). The sintering temperature had the major dominant effect on the total porosity level in compacts, followed by the sintering time. A confirmation test was undertaken to produce a compact with 30 vol.% porosity, by using designed sintering parameters. The experimental results fell within a 90% confidence interval of the predicted result.

A range of porosity levels in the sintered Ti compacts was produced with the aid of Taguchi’s method. Further investigations were carried out to study the influence of porosity on the properties of sintered Ti compacts. It was found that decreasing porosity resulted in a linear reduction in the amount of open porosity and a linear reduction in permeability. A slip casting process for making porous Ti showed a moderate fraction of open pores compared with a press and sintering route and a gel-casting route. A linear relationship also existed between tensile strength and the degree of porosity in compacts. The Haynes’s model gave good data fit; this indicated that the pore geometry and interaction of stress concentrations should be considered. The relative ductility of porous Ti compacts produced by slip casting was comparable with porous Ti compacts produced by a press and sintering route. Haynes’s model produced a good prediction in the relative ductility to porosity relationship. It showed the value of constant (C) in

Haynes’s model is affected by the ability of Ti to strain harden and that interstitial oxygen was the main influence in controlling this.

The pore throat sizes in sintered Ti compacts were also measured using a pore size analyser. The pore throat size decreased with a decreasing level of porosity. Lower porosity compacts gave more spherical pores and higher porosity compacts gave more irregularly shaped pores. When subject to tensile loading, the spherical pores opened up to form irregular pores. The tensile fracture models of porous Ti compacts were illustrated, for material with both high and low porosity levels and spherical powder particles. Ti compacts with high levels of porosity fail in a brittle manner. However, in those with low porosity, the tensile forces lengthen the spherical pores to irregular and/or elongated shapes, which then act as linkage sites and allow cracks to propagate through the material and cause failure.

A novel way of observing the degree of interconnected porosity using ammonium meta-tungstate solution was presented, which proved to be an effective approach. The interconnected pores were filled with tungsten oxide that could be clearly seen using backscattered electron imaging.

The effect of bimodal Ti powder particles on the green packing density, porosity level, pore size, tensile properties and pore interconnectivity of slip cast compacts was also thoroughly investigated. By mixing the coarse and fine HDH Ti powder particles at different compositions, the green packing density of slip cast compacts showed a slightly loose packed structure when the slip cast compacts were made from pure coarse powder particles or pure fine powder particles. However, the maximum packing density in a slip cast compact cannot be easily defined, which might be caused by the irregularity of the Ti powder particles.

Upon sintering, slip cast compacts made with a high content of fine powder particles produces a relatively low porosity level, less pore interconnectivity, small pore diameter and high mechanical properties. Again, the open porosity level has a direct linear relationship with the porosity level in the sintered Ti compacts. However, the permeability displayed a non-linear relationship with the porosity level due to the influence of the pore diameter in the compacts. The normalised permeability, defined as the permeability divided by the average pore diameter squared, showed an improved fit with the porosity level. The capillary tube model was used to well explain the effect of pore diameter on the permeability, when the porosity level is less than 25 vol.%.

The tensile stress of compacts has a directly negative linear relationship with the porosity level, whereas an exponential decay relationship exists between the elongation and the porosity level. A comparison of the tensile properties obtained from a bimodal mixture of powder particles, and that obtained from pure fine powder particles, indicates that the tensile properties of the porous Ti compacts are strongly dependent on the porosity level.

7.2 Future Study

7.2.1 Graded porosity material

Based on the previous investigations, a sintered Ti compact with a porosity gradient microstructure was designed and fabricated. The microstructure at a typical cross section in the sintered Ti compact is shown in Figure 7-1. The graded porosity microstructure was produced by stacking slurries with two different powder particle compositions into layers using slip casting. One layer was composed of 100 vol.% of fine powder particles and the other layer was composed of 20 vol.% of fine powder particles and 80 vol.% of coarse powder particles. Once the slurry was dried to form a compact, it was then debound at 320°C and sintered at 1000°C. The part with a larger pore diameter was made from 20 vol.% of fine powder particles and 80 vol.% of coarse powder particles and the part with a small pore diameter was made from 100 vol.% of fine powder.

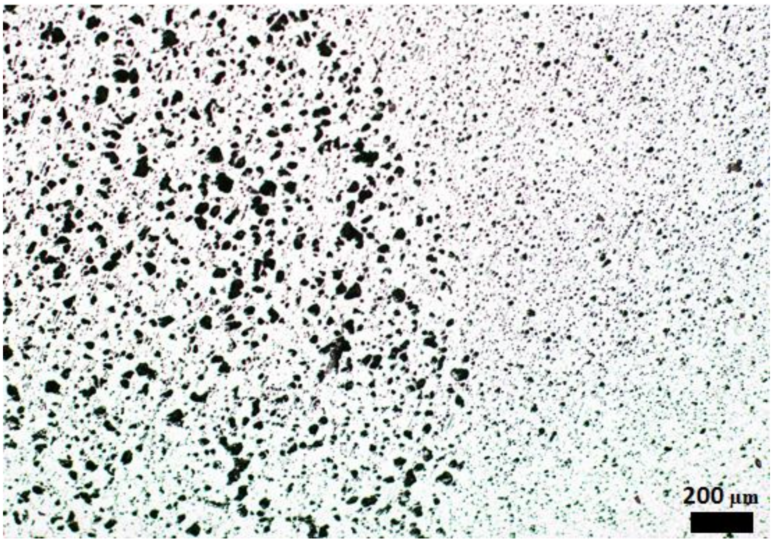

Figure 7-1 Microstructure of a porosity graded Ti specimen prepared by slip casting.

Compared with more conventional material with uniform porosity, functionally graded materials (FGMs), with a microstructure and/or composition gradient, can have superior mechanical strength and biological properties [170-172]. A number of techniques, such as loose powder sintering [43], space holder techniques [173], freeze casting [174], gel casting [15], selective laser sintering [175], etc., have been developed to fabricate Ti parts with a porosity gradient. Among these techniques, Thieme et al [43] fabricated graded porous Ti by employing different powder particle sizes, which was similar to the technique presented in this paper. However, they used ceramic moulds to hold the powder particles together during sintering. Ceramic moulds are expensive and can potentially contaminate the Ti matrix at high sintering temperatures. Using a slip casting route, compacts can be sintered without the use of ceramics moulds. This reduces processing costs and the level of impurities in the finished product.

The results presented here are from a preliminary study. At this stage there is no specific application identified for this porosity gradient material, although a potential application is for use in bio-implants. The porosity in the Ti implants reduces stiffness, which mitigates stress shielding and also is beneficial for the tissue growth into the pores to provide a better bone integration.

Last, but not least, to undertake further study, a few recommendations based on the current study are shown below:

- Figure 7-1 illustrates only two porosity level combinations in a compact. Compacts with a range of porosity gradient should be made using slip casting or different gradient structures.
- It is of interest to undertake a study of the mechanical behaviour of porosity gradient compacts. In particular, the mechanical behaviour at the interface between two different porosity regions should be studied.

References

1. Leyens, C. and M. Peters, eds. *Titanium and titanium alloys. Fundamentals and applications*. 2003, Wiley-VCH GmbH & Co. KGaA: German.

2. Yook, S.W., H.E. Kim, and Y.H. Koh, *Fabrication of porous titanium scaffolds with high compressive strength using camphene-based freeze casting.* Materials Letters, 2009. **63**(17): p. 1502-1504.

3. Yook, S.W., et al., *Porous titanium (Ti) scaffolds by freezing TiH_2/camphene slurries.* Materials Letters, 2008. **62**(30): p. 4506-4508.

4. Li, J.C. and D.C. Dunand, *Mechanical properties of directionally freeze-cast titanium foams.* Acta Materialia, 2011. **59**(1): p. 146-158.

5. Chino, Y. and D.C. Dunand, *Directionally freeze-cast titanium foam with aligned, elongated pores.* Acta Materialia, 2008. **56**(1): p. 105-113.

6. Fife, J., et al., *Morphological analysis of pores in directionally freeze-cast titanium foams.* Journal of Materials Research, 2009. **24**(1): p. 117-124.

7. Murray, N. and D. Dunand, *Effect of thermal history on the superplastic expansion of argon-filled pores in titanium: Part II modeling of kinetics.* Acta materialia, 2004. **52**(8): p. 2279-2291.

8. Dabrowski, B., et al., *Highly porous titanium scaffolds for orthopaedic applications.* Journal of Biomedical Materials Research, Part B: Applied Biomaterials, 2010. **95B**(1): p. 53 - 61.

9. Nouri, A., P. Hodgson, and C. Wen, *Effect of process control agent on the porous structure and mechanical properties of a biomedical Ti-Sn-Nb*

alloy produced by powder metallurgy. Acta biomaterialia, 2010. **6**(4): p. 1630-1639.

10. Hong, T., Z. Guo, and R. Yang, *Fabrication of porous titanium scaffold materials by a fugitive filler method.* Journal of materials science: materials in medicine, 2008. **19**(12): p. 3489-3495.

11. Imwinkelried, T., *Mechanical properties of open pore titanium foam.* Journal of Biomedical Materials Research, Part A, 2007. **81**(4): p. 964-970.

12. Wen, C., et al., *Processing of biocompatible porous Ti and Mg.* Scripta Materialia, 2001. **45**(10): p. 1147-1153.

13. Li, Y., et al., *Porosity and mechanical properties of porous titanium fabricated by gelcasting.* Rare Metals, 2008. **27**(3): p. 282-286.

14. Sánchez-Herencia, A., et al., *Aqueous colloidal processing of nickel powder.* Acta Materialia, 2001. **49**(4): p. 645-651.

15. Erk, K.A., D.C. Dunand, and K.R. Shull, *Titanium with controllable pore fractions by thermoreversible gelcasting of* TiH_2. Acta Materialia, 2008. **56**(18): p. 5147-5157.

16. Ohkawa, S., et al., *Slip casting of titanium powder for dental prosthetic appliances.* Materials Transactions, JIM, 2004. **45**(4): p. 1132-1139.

17. Neirinck, B., et al., *Preparation of titanium foams by slip casting of particle stabilized emulsions.* Advanced Engineering Materials, 2009. **11**(8): p. 633-636.

18. Oh, I., et al., *Mechanical properties of porous titanium compacts prepared by powder sintering.* Scripta Mater, 2003. **49**: p. 1197 - 1202.

19. Dunand, D.C., *Processing of titanium foams.* Advanced Engineering Materials, 2004. **6**(6): p. 369-376.

20. Xu, Q., et al., *The development of porous titanium products using slip casting.* Journal of Materials Processing Technology, 2013. **213**(8): p. 1440-1446.

21. Chen, L., et al., *Porous titanium implants fabricated by metal injection molding.* Transactions of Nonferrous Metals Society of China, 2009. **19**(5): p. 1174-1179.

22. Thabarealam, T., *Production, processing and characterisation of porous TiA alloy produced using space holder method*, in *Department of Engineering*. 2009, University of Waikato: Hamilton, NZ. p. 73.

23. Rak, Z.S. and J. Walter, *Porous titanium foil by tape casting technique.* Journal of materials processing technology, 2006. **175**(1-3): p. 358-363.

24. Thellmann, E.L., P.M. Phillips, and C. Ohio, *Method of slip casting titanium structures*, U.S. Patent, Editor. 1970.

25. Ohkawa, S., et al., *Slip casting of titanium powder for dental prosthetic appliances.* Materials transactions-JIM, 2004. **45**(4): p. 1132-1139.

26. Asthana, R., A. Kumar, and N.B. Dahotre, *Materials processing and manufacturing science*. 2006: Elsevier Academic Press, Boston.

27. Onoda Jr, G.Y. and G.L. Messing, *Packing and sintering relations for binary powders*, in *Processing of Crystalline Ceramics*. 1978, Springer. p. 99-112.

28. German, R.M., *Sintering theory and practice*. 1996: Wiley-VCH.

29. Chawla, N., B. Jester, and D. Vonk, *Bauschinger effect in porous sintered steels.* Materials Science and Engineering: A, 2003. **346**(1): p. 266-272.

30. Chawla, N. and X. Deng, *Microstructure and mechanical behavior of porous sintered steels.* Materials Science and Engineering: A, 2005. **390**(1): p. 98-112.

31. Polasik, S., J. Williams, and N. Chawla, *Fatigue crack initiation and propagation of binder-treated powder metallurgy steels.* Metallurgical and Materials Transactions A, 2002. **33**(1): p. 73-81.

32. Nonferrous, R. *Porous titanium, porous titanium plate, porous titanium exposure, porous titanium filter*. 2011 [cited 2011 7/07]; Available from: http://www.sinomaterial.com/html_products/Porous-Titanium-Porous-Titanium-Plate-Porous-Titanium-exposure-Porous-Titanium-Filter-67.html.

33. Co., A.M. *New porous titanium plate now available*. 2005 [cited 2011 4/07]; Available from: http://www.accumetmaterials.com/new/Ti_plates_release.htm.

34. Kriszt, B. and H. Degischer, *Handbook of cellular metals: Production, processing, applications.* Weinheim: Wiley-VCH, 2002: p. 2002.

35. Org, N. *Dryden flight research centre - Fact sheet*. 1996; Available from: http://www.nasa.gov/centers/dryden/about/Organizations/Technology/Facts/TF-2004-12-DFRC.html.

36. Banhart, J., *Manufacture, characterisation and application of cellular metals and metal foams.* Prog Mater Sci, 2001. **46**: p. 559 - 632.

37. Takemoto, M., et al., *Mechanical properties and osteoconductivity of porous bioactive titanium.* Biomaterials, 2005. **26**: p. 6014 - 6023.

38. Cachinho, S., *Titanium scaffolds for osteointegration: Mechanical, in vitro and corrosion behavior.* J Mater Sci Mater Med, 2008. **19**: p. 451 - 457.

39. Zou, C., et al., *Preparation and characterization of porous [beta]-tricalcium phosphate/collagen composites with an integrated structure.* Biomaterials, 2005. **26**(26): p. 5276-5284.

40. Li, J., *Porous titanium for biomedical applications: Development; characterisation and biological evaluation*. 2007, the University of Twente: Enschede, The Neitherlands. p. 239.

41. Dunand, D., A. Mortensen, and J. Sommer, *Synthesis of bulk and reinforced nickel aluminides by reactive infiltration.* Metallurgical Transactions, A (Physical Metallurgy and Materials Science);(United States), 1993. **24**(10).

42. Cirincione, R., et al., *An investigation of the effects of sintering duration and powder sizes of the porosity and compression strength of porous Ti-6Al-4V.* Processing and properties of lightweight cellular metals and structures, 2002: p. 189.

43. Thieme, M., et al., *Titanium powder sintering for preparation of a porous functionally graded material destined for orthopaedic implants.* Journal of materials science: materials in medicine, 2001. **12**(3): p. 225-231.

44. Hurysz, K., et al., *Steel and titanium hollow sphere foams.* 1998.

45. Lefebvre, L.P. and Y. Thomas, *Method of making open cell material*. 2003, Google Patents.

46. Wheeler, K.R., M.T. Karagianes, and K.R. Sump, in *Conference of Titanium alloys in surgical implants*. 1983, ASTM: Philadelphia.

47. Bram, M., et al., *High porosity titanium, stainless steel, and superalloy parts.* Advanced Engineering Materials, 2000. **2**(4): p. 196-199.

48. Zhang, Y., et al., *High porosity and large pore size shape memory alloys fabricated by using pore-forming agent (NH4HCO3) and capsule-free hot isostatic pressing.* Journal of materials processing technology, 2007. **192**: p. 439-442.

49. Degischer, H.P. and B. Kriszt, *Handbook of cellular metals: production, processing, applications*, ed. G. Rausch and J. Banhart. 2002: Vch Verlagsgesellschaft Mbh.

50. Li, J.P., et al., *Improvement of porous titanium with thicker struts.* Key Engineering Materials, 2002. **240**: p. 547-550.

51. Kearns, M.W., *Formation of porous bodies*. 1987, Google Patents.

52. Kearns, M.W. and P. Blenkinsop, *Manufacture of a novel porous metal.* Int. J. Powder Metall., 1988. **24**(1): p. 59-64.

53. Biasotto, M., et al., *Porous titanium obtained by a new powder metallurgy technique: Preliminary results of human osteoblast adhesion on surface polished substrates.* Journal of applied biomaterials and biomechanics, 2003. **1**(3): p. 172-177.

54. Murray, N. and D. Dunand, *Microstructure evolution during solid-state foaming of titanium.* Composites science and technology, 2003. **63**(16): p. 2311-2316.

55. Dunand, D. and J. Teisen, *Superplastic foaming of titanium and Ti-6 Al-4 V.* 1998.

56. Murray, N. and D. Dunand, *Effect of thermal history on the superplastic expansion of argon-filled pores in titanium: Part I kinetics and microstructure.* Acta materialia, 2004. **52**(8): p. 2269-2278.

57. Murray, N., C. Schuh, and D. Dunand, *Solid-state foaming of titanium by hydrogen-induced internal-stress superplasticity*. Scripta Materialia, 2003. **49**(9): p. 879-883.

58. Janney, M.A. and O.O. Omatete, *Method for molding ceramic powders using a water-based gel casting*. 1991, Google Patents.

59. Janney, M.A., *Gelcasting superalloy powders*. 1995, Oak Ridge National Lab., TN (United States).

60. Li, Y., Z. Guo, and J. Hao, *Gelcasting of 316L stainless steel.* Journal of University of Science and Technology Beijing, Mineral, Metallurgy, Material, 2007. **14**(6): p. 507-511.

61. Ceramics, B.T. *From powder to part*. [cited 2011 18/08]; Available from: http://www.keramverband.de/brevier_engl/4/1/4_1_3.htm.

62. Deville, S., *Freeze-Casting of Porous Ceramics: A Review of Current Achievements and Issues.* Advanced Engineering Materials, 2008. **10**(3): p. 155-169.

63. Sulinski, H.V. and S. Lipson, *Slip casting of copper powder*. 1995: Springer.

64. Takeda, T. and K. Minagawa, *Slip casting of duplex phase stainless steel fine powders.* Journal of the Japan Society of Powder and Powder Metallurgy, 1990. **37**(2): p. 198-202.

65. Sammes, N. and C. Hatchwell, *Optimization of slip-cast* $La_{0.8}Sr_{0.2}CrO_3$ *perovskite material for use as an interconnect in SOFC applications.* Materials Letters, 1997. **32**(5): p. 339-345.

66. Yao, X., S. Tan, and D. Jiang, *Improving the properties of porous hydroxyapatite ceramics by fabricating methods.* Journal of materials science, 2005. **40**(18): p. 4939-4942.

67. Rao, R.R. and T.S. Kannan, *Dispersion and slip casting of hydroxyapatite.* Journal of the American Ceramic Society, 2001. **84**(8): p. 1710-1716.

68. Hotta, Y., et al., *Slip casting using wet-jet milled slurry.* Journal of the European Ceramic Society, 2007. **27**(2): p. 753-757.

69. Takao, Y., et al., *Microstructure of alumina compact body made by slip casting.* Journal of the European Ceramic Society, 2002. **22**(4): p. 397-401.

70. Tsetsekou, A., C. Agrafiotis, and A. Milias, *Optimization of the rheological properties of alumina slurries for ceramic processing applications Part I: Slip-casting.* Journal of the European Ceramic Society, 2001. **21**(3): p. 363-373.

71. Xu, X., et al., *Effect of dispersant on the rheological properties and slip casting of concentrated sialon precursor suspensions.* Journal of the European Ceramic Society, 2003. **23**(9): p. 1525-1530.

72. Moreno, R., *The role of slip additives in tape-casting technology. I: Solvents and dispersants.* American Ceramic Society Bulletin, 1992. **71**(10): p. 1521-1531.

73. Ferreira, J. and H. Diz, *Effect of the amount of deflocculant and powder size distribution on the green properties of silicon carbide bodies obtained by slip casting.* Journal of Hard Materials(UK), 1992. **3**(1): p. 17-27.

74. Tari, G., et al., *Influence of particle size distribution on colloidal processing of alumina.* Journal of the European Ceramic Society, 1998. **18**(3): p. 249-253.

75. Ferreira, J.M.F. and H.M.M. Diz, *Effect of solids loading on slip casting performance of silicon carbide slurries.* Journal of the American Ceramic Society, 1999. **82**(8): p. 1993-2000.

76. Olhero, S. and J. Ferreira, *Influence of particle size distribution on rheology and particle packing of silica-based suspensions.* Powder technology, 2004. **139**(1): p. 69-75.

77. Krieger, I.M., *Rheology of monodisperse latices.* Advances in Colloid and Interface Science, 1972. **3**(2): p. 111-136.

78. Blugan, G., et al., *Development of a tape casting process for making thin layers of Si3N4 and Si3N4á+ áTiN.* Journal of the European Ceramic Society, 2007. **27**(16): p. 4789-4795.

79. Ryu, B.H., M. Takahashi, and S. Suzuki, *Rheological characteristics of aqueous alumina slurry for tape casting.* Nippon seramikkusu kyokai gakujutsu ronbunshi, 1993. **101**(6): p. 643-648.

80. Xu, X., et al., *Effect of dispersant on the rheological properties and slip casting of concentrated sialon precursor suspensions.* Journal of the European Ceramic Society, 2003. **23**(9): p. 1525-1530.

81. Yang, J.F., et al., *Synthesis of porous Si_3N_4 ceramics with rod shaped pore structure.* Journal of the American Ceramic Society, 2005. **88**(4): p. 1030-1032.

82. Masson, C.R., S.G. Whiteway, and C.A. Collings, *Slip casting calcium fluoride and lime stabilised zirconia.* American Ceramic Society Bulletin, 1963. **42**(12): p. 745-47.

83. Hotza, D. and P. Greil, *Review: aqueous tape casting of ceramic powders.* Materials Science and Engineering: A, 1995. **202**(1-2): p. 206-217.

84. Sarraf, H., L. Skarpova, and P. Louda, *Influence of different anionic polyelectrolyte dispersants on the rheological and electrokinetic properties of carbon nanotubes.* Annual Transactions-Nordic Rheology Society, 2007. **15**: p. 253.

85. Singh, B.P., S. Bhattacharjee, and L. Besra, *Optimisation of performance of dispersants in aqueous plasma dissociated zircon suspension.* Ceramics international, 2002. **28**(4): p. 413-417.

86. Kim, M., et al., *Dispersion stability of Y-TZP/Ce-TZP powder system and slip casting.* Journal of Materials Science, 2002. **37**: p. 1661 - 1665.

87. Ushifusa, N. and M.J. Cima, *Aqueous processing of mullite containing green sheets.* Journal of the American Ceramic Society, 1991. **74**(10): p. 2443-2447.

88. Pagnoux, C., T. Chartier, and G. de F, *Aqueous suspensions for tape-casting based on acrylic binders.* Journal of the European Ceramic Society, 1998. **18**(3): p. 241-247.

89. Nagata, K., *Dynamic viscoelastic measurements of suspension for the drying process in tape casting.* Nippon seramikkusu kyokai gakujutsu ronbunshi, 1992. **100**(11): p. 1352-1356.

90. Burnfield, K.E. and B.C. Peterson, eds. *Cellulose ethers in tape casting formulation*. Ceramics Transactions, ed. M.J.Cima. Vol. 26. 1992, American Ceramic Society: Westerville OH. 191 - 196.

91. Nagata, K., *Rheology behavior of suspension and properties of green sheet-effect of compatibility between dispersant and bicder.* J. Ceram. Soc. Jpn, 1992. **100**(10): p. 1271–1275.

92. Mistler, R. and E. Twiname, *Tape casting: Theory and practice*. 2000, Westerville, OH: The American Ceramic Society. 293.

93. Schuetz, J., I. Khoury, and R. Dichiara, *Water-based binder for tape casting.* Ceramics industry, 1987. **66**(10): p. 42 - 44.

94. Thian, E., et al., *Effects of debinding parameters on powder injection molded Ti-6Al-4V/HA composite parts.* Advanced Powder Technology, 2001. **12**(3): p. 361-370.

95. German, R., *Powder injection moulding*. 1990, Princeton, NJ: Metal Powder Industries Federation.

96. Finn, C.W., *Vacuum binder removal and collection.* International Journal of Powder Metallurgy, 1991. **27**(2): p. 127-132.

97. Moore, J., et al., *Atmosphere control during debinding of powder injection molded parts.* Journal of Materials Engineering and Performance, 1995. **4**(3): p. 275-282.

98. Barone, M. and J. Ulicny, *Liquid phase transport during removal of organic binders in injection molded ceramics.* Journal of the American Ceramic Society, 1990. **73**(11): p. 3323-3333.

99. Heaney, D.F. and R.M. German, *Advances in the Sintering of Titanium Powders*, in *PM Lightweight and Porous Materials*. 2004: Vienna, Austria. p. 222-227.

100. Arockiasamy, A., et al., *Effect of additives on sintering response of titanium by powder injection moulding.* Powder Metallurgy, 2011. **54**(3): p. 420-426.

101. Qian, M., *Cold compaction and sintering of titanium and its alloys for near-net-shape or preform fabrication.* International Journal of Powder Metallurgy, 2010. **46**(5): p. 29-44.

102. Zheng, J., W.B. Carlson, and J.S. Reed, *The packing density of binary powder mixtures.* Journal of the European Ceramic Society, 1995. **15**(5): p. 479-483.

103. Westman, A., *The packing of particles: Empirical equations for intermediate diameter ratios.* Journal of the American Ceramic Society, 1936. **19**(1-12): p. 127-129.

104. Westman, A. and H. Hugill, *The packing of particles.* Journal of the American Ceramic Society, 1930. **13**(10): p. 767-779.

105. Furnas, C., *Grading aggregates-I.-Mathematical relations for beds of broken solids of maximum density.* Industrial & Engineering Chemistry, 1931. **23**(9): p. 1052-1058.

106. Messing, G.L. and G.Y. Onoda, *Inhomogeneity‐packing density relations in binary powders.* Journal of the American Ceramic Society, 1978. **61**(1-2): p. 1-5.

107. Messing, G.L. and G.Y. Onoda, *Inhomogeneity‐packing density relations in binary powders—experimental studies.* Journal of the American Ceramic Society, 1978. **61**(7-8): p. 363-366.

108. Zok, F., F.F. Lange, and J.R. Porter, *Packing density of composite powder mixtures.* Journal of the American Ceramic Society, 1991. **74**(8): p. 1880-1885.

109. Abdullah, E. and D. Geldart, *The use of bulk density measurements as flowability indicators.* Powder Technology, 1999. **102**(2): p. 151-165.

110. Poster, A., C. Craig, and H. Hausner, *The effect of powder particle size distribution on the sintering of molybdenum.* Progress in Powder Metallurgy, 1960. **16**: p. 56-70.

111. Smith, J.P. and G. Messing, *Sintering of bimodally distributed alumina powders*. Journal of the American Ceramic Society, 1984. **67**(4): p. 238-242.

112. Griffiths, T.J., R. Davies, and M.B. Bassett, *Analytical study of effects of pore geometry on tensile strength of porous materials.* Powder Metallurgy, 1979. **3**: p. 119-123.

113. Fleck, N. and R. Smith, *Use of simple-models to estimate effect of density on fracture-behavior of sintered steel.* Powder Metallurgy, 1981. **3**: p. 121-125.

114. Haynes, R., *Reviews on the deformation behavior of materials. The mechanical behavior of sintered metals.* Freund Publishing House, 1981: p. 101.

115. Haynes, R., *A study of the effect of porosity content on the ductility of sintered metals.* Powder Metallurgy, 1977. **20**(1): p. 17-20.

116. Kim, S., J. Paek, and B. Kang, *Flow and heat transfer correlations for porous fin in a plate-fin heat exchanger.* Journal of Heat Transfer, 2000. **122**(3): p. 572-578.

117. Kim, S.Y., J.-M. Koo, and A.V. Kuznetsov, *Effect of anisotropy in permeability and effective thermal conductivity on thermal performance of an aluminum foam heat sink.* Numerical Heat Transfer: Part A: Applications, 2001. **40**(1): p. 21-36.

118. Kozeny, J., *Ueber kapillare leitung des wassers im boden.* Sitzungsber. Akad. Wiss. Wien, 1927. **136**: p. 271-306.

119. Carman, P., *Fluid flow through granular beds.* Transactions-Institution of Chemical Engineeres, 1937. **15**: p. 150-166.

120. *Instruction Manual, Particle Charge Dectection - PCD-03*. 1997: Mutek, German.

121. Ji, C., et al., *Sintering study of 316L stainless steel metal injection molding parts using Taguchi method: final density*. Materials Science and Engineering: A, 2001. **311**(1): p. 74-82.

122. Standard, A., *F316-03.* Standard test methods for pore size characteristics of membrane filters by bubble point and mean flow pore test, ASTM International, West Conshohocken, PA, 2003.

123. German, R.M., *Handbook of mathematical relations in particulate materials processing*. Vol. 3. 2009, New Jersey: Wiley-Interscience.

124. Mooney, R., et al., *The dehydration of ammonium metatungstate.* Journal of the Electrochemical Society, 1962. **109**(12): p. 1179-1182.

125. DeHoff, R.T. and F.N. Rhines, eds. *Quantitative microscopy*. McGrow-Hill, New York. 1968.

126. Cachinho, S.C.P. and R.N. Correia, *Titanium porous scaffolds from precursor powders: rheological optimization of* TiH_2 *slurries.* Powder Technology, 2007. **178**(2): p. 109-113.

127. Zhang, J., et al., *Aqueous processing of fine ZrO2 particles.* Colloids and Surfaces A: Physicochemical and Engineering Aspects, 2005. **254**(1-3): p. 199-205.

128. Li, J., C. Van Blitterswijk, and K. De Groot, *Factors having influence on the rheological properties of Ti6A14V slurry.* Journal of materials science: materials in medicine, 2004. **15**(9): p. 951-958.

129. Hunter, R.J., L.R. White, and D.Y.C. Chan, *Foundations of colloid science*. Vol. 1. 1987, Oxford: Clarendon Press

130. Nies, C. and G. Messing, *Effect of glass‐transition temperature of polyethylene glycol‐plasticized polyvinyl alcohol on granule compaction.* Journal of the American Ceramic Society, 1984. **67**(4): p. 301-304.

131. Lewis, J.A., *Binder removal from ceramics.* Annual Review of Materials Science, 1997. **27**(1): p. 147-173.

132. Madorsicy, S. and S. Straus, *Thermal degradation of polyethylene oxide and polypropylene oxide.* Journal of Polymer Science Part A: Polymer Chemistry, 1959. **36**(130): p. 183-194.

133. Jaffee, R., H. Ogden, and D. Maykuth, *Alloys of titanium with carbon, oxygen, and nitrogen.* Trans. AIME, 1950. **188**: p. 1261-1266.

134. Ashby, M.F., et al., *Metal foams: A design guide*. 2000: Butterworth-Heinemann.

135. Leyens, C. and M. Peters, *Titanium and titanium alloys*. 2003: Wiley Online Library.

136. Liu, P. and K. Liang, *Review Functional materials of porous metals made by P/M, electroplating and some other techniques.* Journal of Materials Science, 2001. **36**(21): p. 5059-5072.

137. Scott, K., *Handbook of industrial membranes*. 1995: Oxford: Elsevier Advanced Technology.

138. Ochiai, T., et al., *Anodizing Effects of Titanium-Mesh Surface for Fabrication of Photocatalytic Air Purification Filter.* Nanoscience and Nanotechnology Letters, 2012. **4**(5): p. 544-547.

139. Ochiai, T., et al., *Fabrication of a TiO2 nanoparticles impregnated titanium mesh filter and its application for environmental purification.* Catalysis Science & Technology, 2011. **1**(8): p. 1324-1327.

140. He, Y., et al., *Fabrication of Ti–Al Micro/Nanometer-Sized Porous Alloys through the Kirkendall Effect.* Advanced Materials, 2007. **19**(16): p. 2102-2106.

141. Kang, S.-J.L., *Sintering: densification, grain growth and microstructure*. 2004: Butterworth-Heinemann.

142. Esen, Z., E.T. Bor, and S. Bor, *Characterisation of loose powder sintered porous titanium and Ti6Al4V alloy.* Turkish Journal of Engineering Environmental Science, 2009. **33**: p. 207-219.

143. Sidambe, A., et al., *Metal Injection Moulding of CP-Ti Components for Biomedical Applications.* Journal of Materials Processing Technology, 2012.

144. Kellett, B.J. and F.F. Lange, *Thermodynamics of densification: I, Sintering of simple particle arrays, equilibrium configurations, pore stability, and shrinkage.* Journal of the American Ceramic Society, 1989. **72**(5): p. 725-734.

145. Lange, F.F., *Thermodynamics of densification: II, grain growth in porous compacts and relation to densification.* Journal of the American Ceramic Society, 1989. **72**(5): p. 735-741.

146. Johnson, D., *A general model for the intermediate stage of sintering.* Journal of the American Ceramic Society, 1970. **53**(10): p. 574-577.

147. Johnson, D.L., *New Method of Obtaining Volume, Grain-Boundary, and Surface Diffusion Coefficients from Sintering Data.* Journal of Applied Physics, 1969. **40**(1): p. 192-200.

148. Ashby, M., *A first report on sintering diagrams.* Acta Metallurgica, 1974. **22**(3): p. 275-289.

149. Swinkels, F. and M. Ashby, *A second report on sintering diagrams.* Acta Metallurgica, 1981. **29**(2): p. 259-281.

150. Zhao, J. and M.P. Harmer, *Effect of Pore Distribution on Microstructure Development: II, First‐and Second‐Generation Pores.* Journal of the American Ceramic Society, 1988. **71**(7): p. 530-539.

151. Zhao, J. and M.P. Harmer, *Effect of pore distribution on microstructure development: III, Model experiments.* Journal of the American Ceramic Society, 1992. **75**(4): p. 830-843.

152. Zhao, J. and M.P. Harmer, *Effect of pore distribution on microstructure development: I, Matrix pores.* Journal of the American Ceramic Society, 1988. **71**(2): p. 113-120.

153. Chawla, N., et al., *Axial fatigue behavior of binder-treated versus diffusion alloyed powder metallurgy steels.* Materials Science and Engineering: A, 2001. **308**(1): p. 180-188.

154. Ross, P.J., *Taguchi techniques for quality engineering: loss function, orthogonal experiments, parameter and tolerance design.* 1988.

155. Coleman, S. and W. Beere, *The sintering of open and closed porosity in UO2.* Philosophical Magazine, 1975. **31**(6): p. 1403-1413.

156. Hirschhorn, J.S., A.A. McBeath, and M.R. Dustoor, *Porous titanium surgical implant materials.* Journal of Biomedical Materials Research, 1971. **5**(6): p. 49-67.

157. Dullien, F.A., *Porous media: fluid transport and pore structure*. 1991: Academic press.

158. Bourcier, R., et al., *The influence of porosity on the deformation and fracture of alloys.* Acta Metallurgica, 1986. **34**(12): p. 2443-2453.

159. Lütjering, G. and J.C. Williams, *Titanium*. 2007: Springer-Verlag.

160. German, R.M., *Particle packing characteristics*. 1989, Princeton, NJ: MPIF.

161. Robertson, I. and G. Schaffer, *Review of densification of titanium based powder systems in press and sinter processing.* Powder Metallurgy, 2010. **53**(2): p. 146-162.

162. Smith, L. and P. Midha, *Computer simulation of morphology and packing behaviour of irregular particles, for predicting apparent powder densities.* Computational materials science, 1997. **7**(4): p. 377-383.

163. Karlsson, K. and L. Spring, *Packing of irregular particles.* Journal of Materials Science, 1970. **5**(4): p. 340-344.

164. Xu, Q., B. Gabbitas, and S. Matthews, *Influence of porosity on mechanical behaviour and gas permeability of Ti compacts prepared by slip casting.* Materials Science and Engineering: A, 2013. **587**: p. 123-131.

165. Lowell, S., et al., *Characterization of porous solids and powders: surface area, pore size and density*. Vol. 16. 2006: Springer.

166. Carniglia, S., *Construction of the tortuosity factor from porosimetry.* Journal of Catalysis, 1986. **102**(2): p. 401-418.

167. Froes, F. and D. Eylon, *Powder metallurgy of titanium alloys.* International Materials Reviews, 1990. **35**(1): p. 162-184.

168. Magnusen, P., P. Follansbee, and D. Koss, *The influence of strain rate and porosity on the deformation and fracture of titanium and nickel.* Metallurgical and Materials Transactions A, 1985. **16**(12): p. 2273-2281.

169. Seah, K., R. Thampuran, and S. Teoh, *Parametric studies of the mechanical behaviour of porous titanium.* Metals and Materials, 1998. **4**(4): p. 672-675.

170. Zhang, Y., D. Li, and X. Zhang, *Gradient porosity and large pore size NiTi shape memory alloys.* Scripta Materialia, 2007. **57**(11): p. 1020-1023.

171. Kieback, B., A. Neubrand, and H. Riedel, *Processing techniques for functionally graded materials.* Materials Science and Engineering: A, 2003. **362**(1): p. 81-106.

172. Werner, J., et al., *Mechanical properties and in vitro cell compatibility of hydroxyapatite ceramics with graded pore structure.* Biomaterials, 2002. **23**(21): p. 4285-4294.

173. Fan, X.P., et al., *Graded porous titanium scaffolds fabricated using powder metallurgy technique.* Powder Metallurgy and Metal Ceramics, 2012. **51**(5-6): p. 372-377.

174. Jung, H.-D., et al., *Fabrication of titanium scaffolds with porosity and pore size gradients by sequential freeze casting.* Materials Letters, 2009. **63**(17): p. 1545-1547.

175. Traini, T., et al., *Direct laser metal sintering as a new approach to fabrication of an isoelastic functionally graded material for manufacture of porous titanium dental implants.* Dental Materials, 2008. **24**(11): p. 1525-1533.